



Ulrich Angeringer, Dipl.-Ing.

# **Control Concepts for the Power-Train of Electric Vehicles**

## **DOCTORAL THESIS**

to achieve the university degree of

Doktor der technischen Wissenschaften

submitted to

**Graz University of Technology**

Supervisor

Univ.-Prof. Dipl.-Ing. Dr.techn. Martin Horn

Institute of Automation and Control

Graz, May 2016

# Abstract

The purpose of this thesis is the development and the practical evaluation of a new power-train control concept for the prevention of power-train oscillations. The advantages of this concept are that it does not require any torque sensor information and it copes with backlash of unknown width and the wheel speed information from the vehicle's bus system.

The concept uses a state observer which estimates the shaft and load torque at the power-train. The observer is designed by means of first-order sliding mode technique. It requires the motor and the wheel angular velocity signals for measurement, but in vehicles the information of the wheel speed sensors is available only with a limited update rate. Therefore the sliding mode observer is extended for the case of delayed and sampled signal measurements.

Based on the observer a first-order sliding mode controller is designed for tracking of a given reference torque. Due to the choice of the sliding surface, sliding mode is possible in the contact and backlash phase. The proposed concept is verified by means of a multi-body system simulation of the electrical rear axle of a prototype vehicle. For comparison reasons a second-order sliding mode step-by-step observer and a controller based on the so-called generic second order algorithm are designed.

For the investigation of the presented concepts a test-bench was designed. The rolling resistance, the tire parameters and an approximation of the motor dynamics with a second-order transfer function were experimentally determined. The power-train control concepts are implemented at the servo drive of the test bench. The tests proved a good tracking of the reference torque and sufficiently smooth backlash-contact transition. The developed control concept with delayed and sampled measurement of the wheel speed information performs with respect to tracking and backlash-contact transition nearly as good as the concept with undelayed and high-frequency sampled measurements.

# Zusammenfassung

Das Ziel dieser Arbeit ist die Entwicklung und praktische Evaluierung eines neuen Regelkonzeptes zur Unterdrückung von Antriebsstrangschwingungen. Ein Vorteil dieses Konzeptes ist, dass kein Momentensensor benötigt wird. Zusätzlich ist das Regelkonzept in der Lage mit Getriebespiel nicht bekannter Weite und den Raddrehzahlwerten vom Fahrzeugbussystem zurechtzukommen.

Das Konzept nutzt einen Zustandsbeobachter für die Schätzung des Antriebsstrang- und Lastmoments, wofür ein Sliding Mode Ansatz erster Ordnung verwendet wird. Es werden die Motor- und Raddrehzahlinformation benötigt. In einem Fahrzeug sind die Raddrehzalgrößen jedoch nur mit einer beschränkten Wiederholrate verfügbar. Daher wird der Sliding Mode Beobachter für die Verwendung von zusätzlichen Messsignalen erweitert, die totzeitbehaftet und abgetastet sind.

Aufbauend auf dem Beobachter wird ein Sliding Mode Regler erster Ordnung für die Nachführung eines Referenzmomentes entworfen. Durch die Wahl der Sliding Mode Schaltfläche wird ein Sliding Mode sowohl in der Kontakt- als auch in der Spielphase ermöglicht. Das entworfenen Regelkonzept wird mit einer Mehrkörpersimulation einer elektrisch angetriebenen Hinterachse eines Prototypenfahrzeuges evaluiert. Für Vergleichszwecke wird ein step-by-step Beobachter mit Sliding Mode Methoden zweiter Ordnung und ein Regler mit Hilfe eines sogenannten generischen Algorithmus zweiter Ordnung entworfen.

Für die Evaluierung der entwickelten Konzepte wurde ein Prüfstand entworfen. Die Rollreibung, die Reifenparameter und eine Approximation der Motordynamik mit einer Übertragungsfunktion zweiter Ordnung wurden experimentell bestimmt. Die Regelkonzepte wurden im Umrichter des Prüfstandes implementiert. Die Experimente zeigen eine gute Nachführung des Referenzmomentes und einen hinreichend sanften Spiel-Kontaktübergang. Das entwickelte Konzept, welches verzögerte und abgetastete Raddrehzahlmesswerte verwendet, verhält sich bezüglich Nachführung und Spiel-Kontaktübergang annähernd so gut wie mit unverzögerten und hochfrequent abgetasteten Messwerten.

# Acknowledgements

This work was made possible by a cooperation between MAGNA STEYR Engineering, MAGNA Powertrain, MAGNA Project House, the Institute for Smart System Technologies, Control and Mechatronic systems group at the Alpen-Adria Universität Klagenfurt, and the Institute of Automation and Control at the Graz University of Technology.

First of all, I would like to thank my advisor Univ.-Prof. Dr. Martin Horn who gave me the possibility to work in his group and for his scientific guidance on the project. I also would like to thank Prof. Dr. Bojan Grčar for his comments on the thesis. I thank my colleagues at the Institute of Automation and Control and the Control and Mechatronic Systems group, and especially Dr. Markus Reichhartinger, for the interesting discussions and the very good working atmosphere.

I am grateful to Dipl.-Ing. Manfred Speiser from MAGNA Powertrain and Dipl.-Ing. Gabriel Stabentheiner from MAGNA STEYR for enabling me to work on this project. I thank Rupert Altenstrasser and Fred Arneitz for assembling the test bench.

Finally, I thank my wife Larissa for her love and patience.

# Affidavit

I declare that I have authored this thesis independently, that I have not used other than the declared sources/resources, and that I have explicitly indicated all material which has been quoted either literally or by content from the sources used. The text document uploaded to TUGRAZonline is identical to the present doctoral thesis.

---

Date

---

Signature

# Contents

<b>1</b>	<b>Introduction</b>	<b>1</b>
1.1	Torsional oscillations . . . . .	1
1.2	Previous works . . . . .	2
1.3	Objectives . . . . .	3
1.4	Outline of the thesis . . . . .	4
<b>2</b>	<b>System Modeling</b>	<b>6</b>
2.1	Frequency-domain analysis of a linear two-mass system . . . . .	6
2.1.1	System representation . . . . .	6
2.1.2	Neglected viscous damping . . . . .	8
2.1.3	Transfer function approximation . . . . .	9
2.2	Forces acting on the wheels and the vehicle . . . . .	10
2.2.1	Rolling resistance . . . . .	12
2.2.2	Longitudinal tire forces . . . . .	12
2.3	Backlash models . . . . .	13
2.3.1	Dead-zone model . . . . .	13
2.3.2	Physical model . . . . .	14
2.4	Power-train modeling . . . . .	15
2.4.1	Two-mass system model . . . . .	15
2.4.2	Synthesis model . . . . .	18
2.5	Wheel speed sensor and bus model . . . . .	19
2.5.1	Automotive wheel speed sensor . . . . .	19
2.5.2	Wheel speed sensor model . . . . .	19
2.5.3	Bus model . . . . .	21
2.6	Test bench model . . . . .	22
2.6.1	Test bench description . . . . .	22
2.6.2	Tire model . . . . .	23
2.6.3	Backlash model . . . . .	23
2.6.4	Model of the EM . . . . .	24
2.6.5	Differential equations . . . . .	24
<b>3</b>	<b>Power-Train State Estimation</b>	<b>25</b>
3.1	Observability . . . . .	26
3.1.1	Definition and criteria . . . . .	26
3.1.2	Observability measures . . . . .	27

3.2	First-order sliding mode observers . . . . .	30
3.2.1	Sliding mode observer for LTI systems . . . . .	30
3.2.2	Extension for delayed and sampled measurements . . . . .	32
3.2.3	Observer design for a power-train with backlash . . . . .	36
3.3	Second-order sliding mode observer . . . . .	40
3.3.1	Step-by-step observer . . . . .	40
3.3.2	Observer design for a power-train with backlash . . . . .	42
<b>4</b>	<b>Power-Train Control Concepts</b>	<b>46</b>
4.1	First-order sliding mode based control . . . . .	47
4.1.1	Sliding surface design . . . . .	47
4.1.2	Power-train control design . . . . .	47
4.1.3	Chattering reduction . . . . .	49
4.1.4	Controller analysis in backlash phase . . . . .	51
4.1.5	Remarks on the definition of the sliding surface . . . . .	52
4.2	Power-train control software . . . . .	53
4.2.1	Conditional usage of the delayed correction term . . . . .	53
4.2.2	Reference torque limitation . . . . .	55
4.3	Multi-body system simulation . . . . .	55
4.3.1	Model of an electrically driven rear axle . . . . .	55
4.3.2	Implemented control concept . . . . .	57
4.3.3	Controller and observer parameters . . . . .	57
4.3.4	Simulated maneuvers . . . . .	59
4.4	Generic second order algorithm (GSOA) . . . . .	62
4.4.1	GSOA with lower-order terms . . . . .	62
4.4.2	Power-train control design . . . . .	63
<b>5</b>	<b>Test Bench Design and Concept Verification</b>	<b>64</b>
5.1	Mechanical test bench design . . . . .	65
5.1.1	Design goals . . . . .	65
5.1.2	Test bench realization . . . . .	66
5.1.3	Torsion bar design . . . . .	67
5.2	Electrical topology . . . . .	67
5.3	Parameter identification . . . . .	68
5.3.1	Motor torque calculation . . . . .	68
5.3.2	Linear model of the induction machine . . . . .	69
5.3.3	Rolling resistance . . . . .	70
5.3.4	Tire model . . . . .	70
5.4	Test bench model . . . . .	71
5.4.1	Model evaluation . . . . .	71
5.4.2	Synthesis model . . . . .	74
5.5	Concept implementation . . . . .	74
5.6	Experiments . . . . .	75
5.6.1	First order SMC concepts . . . . .	75
5.6.2	Higher-order based concepts . . . . .	84

<b>6</b>	<b>Summary and Outlook</b>	<b>87</b>
<b>A</b>	<b>Stability of Linear Sampled Data Systems</b>	<b>89</b>
<b>B</b>	<b>Observer and Controller Analysis</b>	<b>91</b>
B.1	Observer analysis with respect to unknown backlash width . . . . .	91
B.1.1	Measurements without delay . . . . .	91
B.1.2	Delayed and sampled load speed measurement . . . . .	93
B.2	Observer analysis with respect to a unknown load inertia . . . . .	94
B.2.1	Measurements without delay . . . . .	94
B.2.2	Delayed and sampled measurements . . . . .	95
B.3	Observer analysis with known backlash width . . . . .	96
B.3.1	Sliding mode observer for nonlinear systems . . . . .	96
B.3.2	Power-train observer design . . . . .	96
B.3.3	Observer stability analysis . . . . .	97
B.4	Sliding surface with unknown load inertia . . . . .	98
<b>C</b>	<b>Parameters</b>	<b>99</b>
C.1	Test bench parameters . . . . .	99
C.2	Parameters of the MBS simulation model . . . . .	103
	<b>Nomenclature</b>	<b>104</b>
	Symbols . . . . .	104
	Acronyms . . . . .	108
	<b>List of Figures</b>	<b>109</b>
	<b>List of Tables</b>	<b>111</b>
	<b>Bibliography</b>	<b>112</b>

# Chapter 1

## Introduction

Passenger vehicles and vans emit about 15 % of the overall carbon dioxide (CO<sub>2</sub>) in the European Union (EU). The framework for climate and energy of the EU for 2030 requires a reduction of at least 40 % of greenhouse gases compared to 1990<sup>1</sup>. This legal requirement and rising fuel prices will have a significant impact on the automotive industry in the long term such that the market share of electric vehicles (EV) and hybrid electric vehicles (HEV) will increase. Thus further development and improvement of EVs and HEVs is important. One of the problems of electrically driven vehicles is that torsional oscillations can arise in the power-train such that the driving comfort is significantly reduced.

### 1.1 Torsional oscillations

An automotive power-train corresponds to a low-damped system where unwanted torsional oscillations can be stimulated which result in vehicle jerk and discomfort. Torsional oscillations can also cause significant wear of mechanical parts in the power-train and as a consequence their life time is reduced. The torque of electric machines (EM) can be well controlled by means of field-oriented control (FOC). Therefore it is expected that torsional oscillation can be reduced for electrically driven vehicles by appropriate power-train control methods such that driving safety and comfort remain preserved.

In [Men01] the factors influencing the torsional oscillations of the power-train at the rear axle of an electrically driven passenger vehicle are analyzed. The power-train consists of an EM, a transmission and a final drive, drive shafts and wheels<sup>2</sup>. The oscillations occur mainly due to the elasticity of the low-damped drive shafts. These oscillations are of low frequency which is in general less than 10 Hz. Backlash is present within the gear and the joints of the drive shafts. Fast torque changes from zero to a constant value or converse, also called "tip-in" and "back-out", can increase the torsional oscillations due to the abrupt backlash-contact transitions. In general this can be acoustically noticed and significantly

---

<sup>1</sup><http://ec.europa.eu/clima/>

<sup>2</sup>For HEVs this configuration is sometimes called Electric Rear Axle Drive (ERAD).

deteriorates the driving comfort. The tire slip increases the damping of the torsional oscillations which grows with vehicle speed. The rise time of the torque of the EM has a significant influence. Assuming linearity and presuming that the torque of the EM corresponds to an ideal ramp the zeros in the spectrum of the ramp function can be exploited by choosing the rise time as a multiple of the reciprocal eigen-frequency [Men01]. In practice there is some mitigation of the oscillations because of the nonlinear tire slip, a non-ideal torque ramp of the EM and model uncertainties.

## 1.2 Previous works

In [NG02] a survey for controlling mechanical systems with backlash is presented. The article mainly examines speed and position control applications. In general and for the case of power-train control the control design is based on a two-mass system representation, see for example [Men01, ABP04, KN05].

In [Men01] control concepts for damping of torsional oscillations are evaluated for the power-train of electrically driven passenger vehicles. The first control concept reduces the power-train oscillations by an additional damping factor. This can be achieved by a feedback of the difference of the angular speeds, i.e. the difference of the motor and load angular speed of the two-mass system. It is assumed that only the motor angular speed is measurable such that the load angular speed is estimated by means of an observer. The second concept feeds back the torsion angle which is estimated by the observer. This concept reduces the motor inertia. Combining both concepts results in a state feedback.

In [ABP04] a control scheme for damping power-train oscillations for electrically driven vehicles is described. The shaft torque is estimated by means of a Kalman filter including a dead zone model for the backlash. The wheel speed sensor information is used dependent on the velocity. It is provided by the controller area network (CAN) bus which has been considered by a constant delay. The control law is represented by a third-order discrete-time transfer function from the estimated shaft torque to the motor torque. It has been designed such that the steady state control output is zero, i.e. it has a zero at  $z = 1$  which means differentiating behavior. Measurements from a prototype vehicle are given.

In [KN05] the power-train of passenger cars with conventional integrated combustion engines (ICE) has been modeled as a linear two-mass system for anti-jerking control. The vehicle mass is considered in the load inertia. In [TE09] a linear-quadratic regulator (LQR) with integral part for anti-jerking control for a truck with a diesel engine is proposed. In the synthesis model the wheel slip is considered which is defined as the difference between load and wheel speed. In [XHH<sup>+</sup>11] a model-predictive control scheme for anti-jerk during the tip-in/tip-out process is presented.

In [GK13] a drivetrain observer for active damping control is presented. In [HK07] a state observer for mechanical systems with backlash is presented and its asymptotic stability is shown by means of Popov's criterion. In [LE07] a state

observer for automotive power-trains with backlash is presented. The twist angle and the backlash width are estimated.

In [CSV<sup>+</sup>06] an observer and a control law for linear systems based on sampled data measurements are presented. In [Web08] a proportional-differential (PD), an LQR and a model predictive control (MPC) for the power-train of heavy commercial vehicles are presented. The controller parameters are adapted with the help of parameter estimation algorithms. The effect of the control with respect to the driving comfort is investigated by analyzing gear switching maneuvers and oscillations of the pitch rate of the driving cab. The state estimation is performed with a Kalman filter where the delayed wheel speed signals are extrapolated.

Unknown input observers using first-order sliding modes are presented in [ES98] and in [Spu08] a survey of sliding mode observers (SMO) is given. The effect of chattering can be reduced by using higher order sliding modes. In [FB06] a canonical form for the design of unknown input sliding mode observers is presented. This observer incorporates the so called super-twisting algorithm of [Lev93] step-by-step. In [FLD06a, FLD06b] a higher order sliding mode differentiator based observer for linear systems with unknown inputs is presented.

### 1.3 Objectives

The goal of this thesis is to develop a power-train control concept for electrically driven vehicles such that unwanted oscillations will be significantly reduced, also for the case if backlash is present in the power-train. Reduced oscillations also mean that the driving comfort can be improved and more energy can be regenerated. The power-train control concept should be able to cope with the following restrictions given in series passenger vehicles:

- The knowledge of the system states, such as the shaft torque, can improve the control performance. Due to cost reasons torque sensors will rather not be present in the near future in an automotive power-train. Therefore techniques for estimating the drive shaft torque with sufficient accuracy and reliability are preferred. The power-train is additionally affected by an *unknown input*, the load torque which results mainly from the acceleration force and the road gradient.
- The play within the power-train is distributed and no angular encoders are available to measure the backlash angle. Additionally the backlash widths may vary due to series production, ageing and changing ambient conditions.
- The automotive wheel speed sensors of the anti-lock braking system (ABS) used in series passenger vehicles have a low resolution such that the measured signal cannot be used in the control concept at small angular velocities.
- The wheel speed information is available on the vehicle's bus system. In general the cycle time of the control software is less than the message update

time on the bus<sup>3</sup>. Additionally there is some delay due to measurement or signal processing.

- In general the computational power of processors in automotive electronic control units (ECU) is comparably low.

## 1.4 Outline of the thesis

In order to reach the goals with the restrictions listed in section 1.3 sliding mode techniques will be used in this thesis. Due to the absence of torque sensors the presented control concepts are based on state observers.

**Chapter 2** first introduces two-mass systems, tire forces and backlash models. Then a power-train model for an electrically driven vehicle will be represented as a two-mass system with backlash. From that a linear synthesis model is derived, where the backlash is neglected since its width and its actual angle are unknown. An automotive wheel speed sensor model is presented. The delay of the wheel speed signal due to the measurement and the automotive bus system is analyzed. A test bench for analyzing and verifying the power-train control concepts is presented. A detailed three-mass model including tire slip is derived.

**Chapter 3** presents sliding mode based observers for estimating the not measurable state variables and the *unknown input*. It is estimated by means of a disturbance model. A first-order sliding mode observer for linear-time invariant (LTI) systems is extended for delayed and sampled measurements as it is the case for the wheel speed information provided by the automotive bus system. The determination of the observer gains for the sliding mode observer with delayed and sampled measurements involves a linear matrix inequality (LMI) design procedure. Additionally a second-order sliding mode *unknown input observer* concept for power-train state estimation is presented.

**Chapter 4** presents sliding mode based control concepts for controlling the shaft torque in an automotive power-train with backlash. The control concepts are based on the state estimates. The first concept incorporates a first-order sliding mode design. Appropriate methods for chattering reduction are applied. The control concept is evaluated with a multi-body system (MBS) simulation model of an electrically driven axle of a hybrid vehicle. The second concept is based on a reduced version of the so-called generic second order algorithm (GSOA).

**Chapter 5** describes the test bench in detail, especially the design of the torsion bar and the electrical topology. The tire-cylinder friction forces and the step response of the torque generating current are analyzed. The corresponding observer and control gains are determined for the test bench. Test bench experiments are

---

<sup>3</sup>The message update time at the bus system of the wheel speed signals is typically 10 ms.

presented and discussed.

**Chapter 6** summarizes the presented work and gives an outlook for future work.

**Appendix A** describes two criteria for the the stability of linear sampled data systems expressed with time-varying delay.

**Appendix B** analyzes the error dynamics of the first order sliding mode based observer concepts for the contact and backlash phase. Additionally a sliding mode control concept for the case that the backlash width is known is presented and discussed.

**Appendix C** contains additional information and parameters of the test bench and the MBS simulation model.

# Chapter 2

## System Modeling

At the beginning of this chapter a linear two-mass system is analyzed in the frequency domain. The longitudinal forces acting on the wheel and the vehicle are described and a physical backlash model is compared with the well-known dead zone model.

Then a power-train model for passenger vehicles including backlash is derived. It represents the power-train of a driven axle, for example an electrically driven rear axle. The model lumps the main elasticities of the drive-shafts such that the power-train can be represented as a two-mass system. In an automotive power-train the backlash widths and the backlash angles are unknown. Therefore the synthesis model for observer and control design does not contain a backlash model. A model of a wheel speed sensor currently used in series passenger vehicles is presented. The wheel speed information is transmitted over the vehicle's bus system for which also a simple model is described.

A test-bench which has been designed for verifying the developed control concepts is introduced in this section. It is modeled as a three-mass system including nonlinear friction and tire-slip.

### 2.1 Frequency-domain analysis of a linear two-mass system

In this section a linear two-mass system is analyzed in the frequency domain and an approximate transfer function is derived for the case that viscous friction is considered.

#### 2.1.1 System representation

The two-mass system as shown in Fig. 2.1 consists of two mass moments of inertia and a flexible shaft. It is assumed that the left inertia, denoted by  $J_m$ , represents a motor with the driving torque  $T_m$ . The right inertia represents the load and is denoted by  $J_l$ . The angular frequencies of the motor and load are denoted by  $\omega_m$  and  $\omega_l$ . The viscous damping coefficient with respect to the motor and the

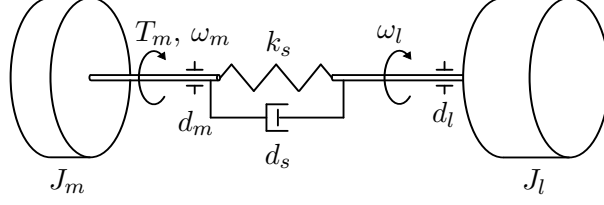


Figure 2.1: Two-mass system with additional viscous friction at the motor and the load.

load are denoted by  $d_m$  and  $d_l$  respectively<sup>1</sup>. It is assumed that the flexible shaft consists of an ideal spring with stiffness  $k_s$  and internal speed-dependent damping. The damping coefficient is denoted by  $d_s$ . According to [Föl08] the torque at the shaft is calculated as

$$T_s = k_s \varphi + d_s \dot{\varphi}, \quad (2.1)$$

where  $\varphi$  denotes the torsion angle of the shaft. It is defined by the difference between the motor angle and the angle of the load such that its derivative corresponds to  $\dot{\varphi} = \omega_m - \omega_l$ . The differential equations of the two-mass system are given by

$$\begin{aligned} \dot{\varphi} &= \omega_m - \omega_l, \\ J_l \dot{\omega}_l &= T_s - d_l \omega_l, \\ J_m \dot{\omega}_m &= -T_s - d_m \omega_m + T_m. \end{aligned} \quad (2.2)$$

Equations (2.2) represent a linear, time-invariant (LTI) system which can be written in matrix notation as

$$\begin{aligned} \dot{\mathbf{x}} &= \mathbf{A}\mathbf{x} + \mathbf{b}u, \\ \mathbf{y} &= \mathbf{c}^T \mathbf{x}, \end{aligned} \quad (2.3)$$

where  $u = T_m$ ,  $\mathbf{x}$  denotes the state and  $\mathbf{b}$  is the input vector, i.e.

$$\mathbf{x} = \begin{bmatrix} \varphi \\ \omega_l \\ \omega_m \end{bmatrix}, \quad \mathbf{b} = \begin{bmatrix} 0 \\ 0 \\ \frac{1}{J_m} \end{bmatrix}. \quad (2.4)$$

The system matrix is given by

$$\mathbf{A} = \begin{bmatrix} 0 & -1 & 1 \\ \frac{k_s}{J_l} & -\frac{d_s+d_l}{J_l} & \frac{d_s}{J_l} \\ -\frac{k_s}{J_m} & \frac{d_s}{J_m} & -\frac{d_s+d_m}{J_m} \end{bmatrix}. \quad (2.5)$$

For the frequency domain analysis the shaft torque is of interest. Therefore the output vector was chosen as

$$\mathbf{c}^T = [k_s \quad -d_s \quad d_s]. \quad (2.6)$$

<sup>1</sup>The viscous damping of the motor can also be considered in the motor torque  $T_m$  such that it can be set to zero.

The transfer function from the input torque  $T_m$  to the shaft torque  $T_s$  is calculated by

$$G_{\text{sm}}(s) = \frac{T_s(s)}{T_m(s)} = \mathbf{c}^T (s\mathbf{I} - \mathbf{A})^{-1} \mathbf{b}, \quad (2.7)$$

where  $s$  denotes the complex Laplace variable and  $\mathbf{I}$  denotes the unit matrix of dimension three. The transfer function is given by

$$G_{\text{sm}}(s) = \frac{d_s J_l s^2 + (J_l k_s + d_l d_s) s + d_l k_s}{n(s)}, \quad (2.8)$$

where

$$\begin{aligned} n(s) = & J_l J_m s^3 + ((d_s + d_l) J_m + (d_s + d_m) J_l) s^2 + \\ & + ((J_m + J_l) k_s + (d_m + d_l) d_s + d_l d_m) s + (d_m + d_l) k_s. \end{aligned}$$

### 2.1.2 Neglected viscous damping

At first, for the analysis of the transfer function (2.8) the viscous damping coefficients are neglected, i.e.  $d_m = 0$  and  $d_l = 0$ . Then the zeros at  $s = 0$  in the numerator and denominator of (2.8) cancel out such that the order of the transfer function is reduced by one, i.e.

$$\begin{aligned} G_{\text{sm}}(s) &= \frac{d_s J_l s + J_l k_s}{J_l J_m s^2 + d_s (J_m + J_l) s + (J_m + J_l) k_s} \\ &= \frac{J_l}{J_m + J_l} \frac{\left(\frac{d_s}{k_s} s + 1\right)}{\frac{J_m J_l}{(J_m + J_l) k_s} s^2 + \frac{d_s}{k_s} s + 1} \\ &= V_0 \frac{z_0(s)}{n_0(s)}. \end{aligned} \quad (2.9)$$

The denominator  $n_0(s)$  has the form of a normed polynomial, see e.g. [Föl08],

$$n_0(s) = \frac{s^2}{\omega_0^2} + \frac{2\zeta}{\omega_0} s + 1, \quad (2.10)$$

where  $\omega_0$  and  $\zeta$  correspond to the undamped natural frequency and the damping ratio. Comparing the coefficients their values are

$$\begin{aligned} \omega_0 &= \sqrt{\frac{(J_m + J_l) k_s}{J_m J_l}}, \\ \zeta &= \frac{d_s}{2} \sqrt{\frac{J_m + J_l}{J_m J_l k_s}}. \end{aligned} \quad (2.11)$$

For different damping ratios  $0 \leq \zeta \leq 1$  the roots of the normed polynomial (2.10) are

$$s_{1,2} = -\zeta \omega_0 \pm j \sqrt{1 - \zeta^2} \omega_0. \quad (2.12)$$

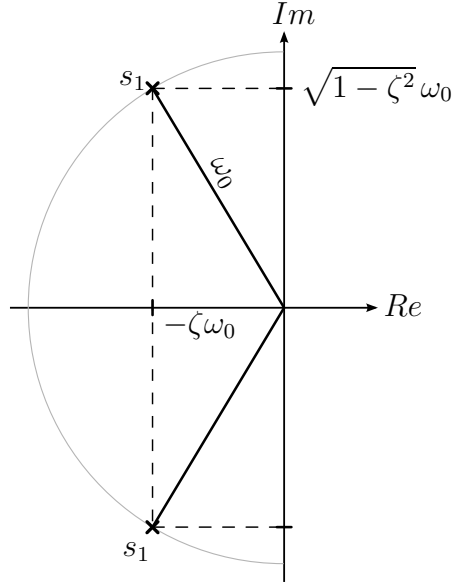


Figure 2.2: Roots of the normed second order polynomial.

The roots are located at a semi circle in the closed left complex half plane with radius  $\omega_0$ , see [HD04]. This is shown in Fig. 2.2. For small damping ratios  $\zeta$  the amplitude plot of the transfer function (2.9) has a significant resonant peak. The resonance frequency of (2.9) is very close to the resonance frequency  $\omega_{\text{res}}$  of the transfer function

$$G_{\text{sm},0}(s) = \frac{1}{\frac{s^2}{\omega_0^2} + \frac{2\zeta}{\omega_0}s + 1}, \quad (2.13)$$

which is

$$\omega_{\text{res}} = \omega_0 \sqrt{1 - 2\zeta^2}. \quad (2.14)$$

### 2.1.3 Transfer function approximation

In the above analysis the damping coefficients  $d_m$  and  $d_l$  were neglected. If the damping coefficients are different from zero the exact symbolic calculation of the poles of the transfer function (2.8) becomes tedious. But the poles can be well approximated. In [Sch09] the transfer function from the motor torque to the motor angular velocity of a two-mass system is represented as a combination of the stiff and the elastic system.

For  $k_s \rightarrow \infty$  the transfer function (2.8) corresponds to

$$\lim_{k_s \rightarrow \infty} G_{\text{sm}}(s) = \frac{d_l}{d_m + d_l} \frac{\frac{J_l}{d_l}s + 1}{\frac{J_m + J_l}{d_m + d_l}s + 1}. \quad (2.15)$$

Factoring out the numerator and denominator of (2.15) from the numerator and denominator of (2.8) and neglecting the terms multiplied with  $J_m^2$  and  $d_m$  in the

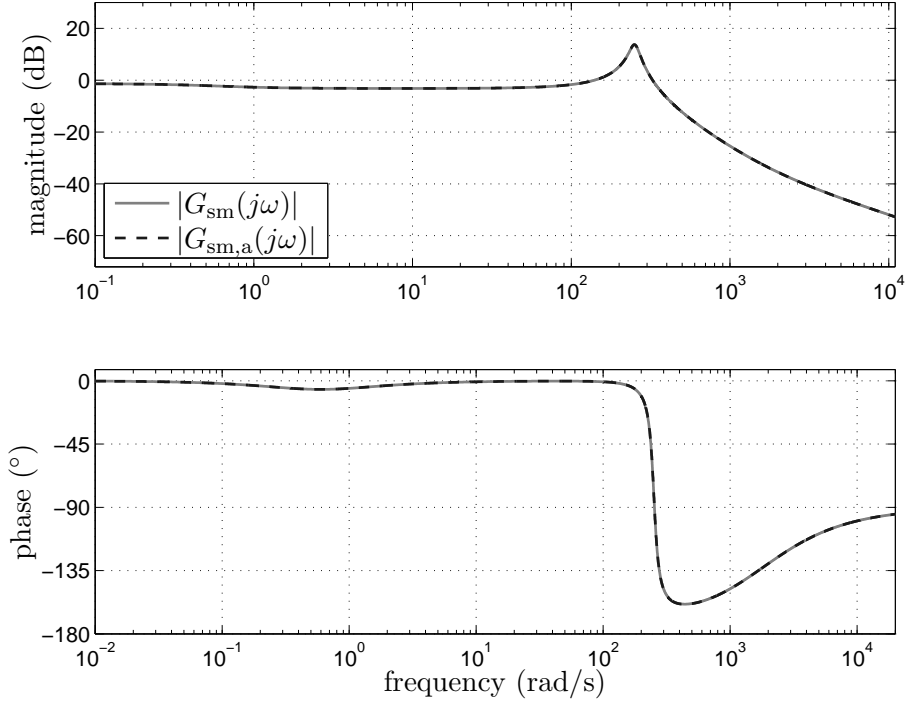


Figure 2.3: Bode diagrams of the transfer function (2.8) of a two-mass system and its approximation (2.16).

denominator, the transfer function (2.8) can be approximated by

$$G_{sm,a}(s) = \frac{d_l}{d_m + d_l} \frac{\left(\frac{J_l}{d_l}s + 1\right) \left(\frac{d_s}{k_s}s + 1\right)}{\left(\frac{J_m + J_l}{d_m + d_l}s + 1\right) \left(\frac{J_m J_l}{(J_m + J_l)k_s}s^2 + \frac{d_s}{k_s}s + 1\right)}. \quad (2.16)$$

The Bode diagrams of the transfer functions (2.8) and (2.16) are shown in Fig. 2.3. The transfer function was parameterized with the parameters of the test bench, see Tab. C.3.

## 2.2 Forces acting on the wheels and the vehicle

In [MW04] the forces acting on the wheels, the vehicle body and the road are described as shown in Fig. 2.4. The aerodynamic resistance  $F_{ad}$  acts on the vehicle's front area. The sum of the tread forces are denoted by  $F_x$ , the vertical force by  $F_z$ . The torques and forces apply to the driven axle.  $F_a$  denotes the longitudinal axle force,  $m_v$  and  $m_w$  denote the vehicle mass in the center of gravity (COG) and the mass of the wheels at the axle respectively. The *static tire radius* is denoted by  $r_{st}$  and corresponds to the distance from the wheel center to the road. The drive shaft torque is denoted by  $T_s$ . The longitudinal tire force  $F_x$  at the tread is composed of the resistance force due to the road gradient  $\chi$ , the rolling resistance  $F_r$  and the acceleration resistance  $F_{acc}$ . The acceleration resistance consists of the

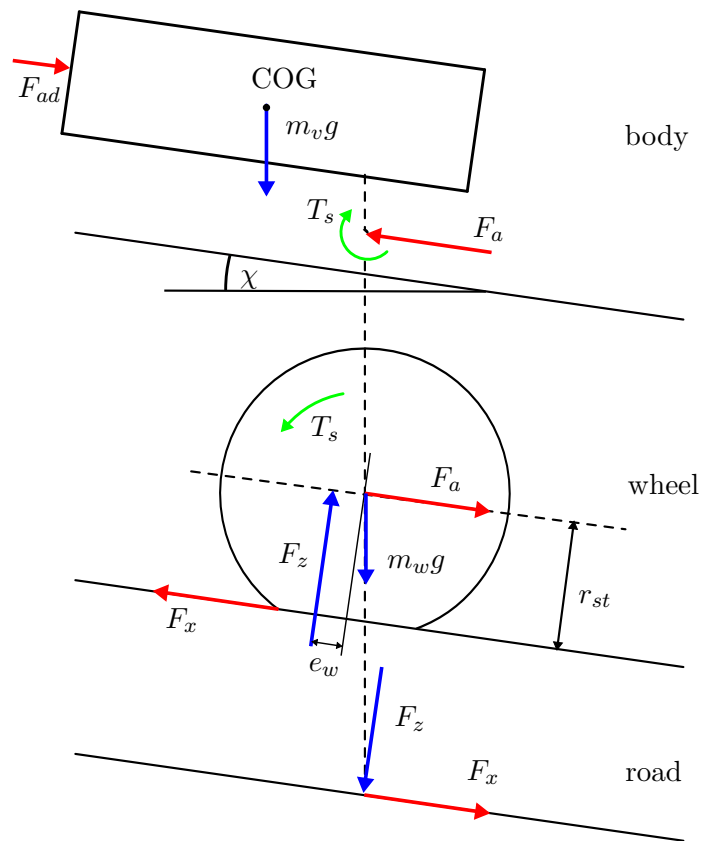


Figure 2.4: Forces acting on the wheel and vehicle according to [MW04].

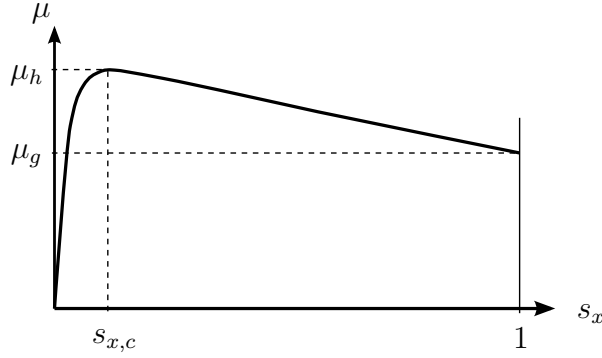


Figure 2.5: Friction coefficient  $\mu$  versus tire slip.

acceleration force of the vehicle including the axles, the wheels and the acceleration force due to the rotating parts.

### 2.2.1 Rolling resistance

The rolling resistance results mainly from the deformation work of the tire due to the rolling motion. Additionally the pressure distribution in the tire contact patch is not constant. This results in a reaction torque  $F_z e_w$  proportional to the vertical load, where  $e_w$  corresponds to the distance of the pressure maximum to the center of the contact patch, see Fig. 2.4. The rolling resistance depends approximately linearly on the vertical force  $F_z$ , see [MW04], i.e

$$F_r = f_r F_z, \quad (2.17)$$

where  $f_r$  denotes the rolling resistance coefficient. It consists of a constant and a speed-dependent part, i.e.

$$f_r = f_{r0} + f_{r1} \left( \frac{v_x}{100} \right) + f_{r4} \left( \frac{v_x}{100} \right)^4, \quad (2.18)$$

where the longitudinal vehicle velocity  $v_x$  has to be inserted in  $\text{km h}^{-1}$ . The coefficient  $f_{r4}$  can be neglected up to a vehicle velocity of  $150 \text{ km h}^{-1}$ .

### 2.2.2 Longitudinal tire forces

According to [MW04] the friction coefficient  $\mu$  is defined as

$$\mu = \frac{F_x}{F_z}. \quad (2.19)$$

The friction coefficient depends on the tire slip  $s_x$  and on the road condition. The tire slip is constituted of a deformation of the rubber and a gliding part. It is

defined as

$$s_x = \begin{cases} \frac{v_x - \omega_w r_{\text{dyn}}}{v_x} & \text{for braking,} \\ \frac{\omega_w r_{\text{dyn}} - v_x}{\omega_w r_{\text{dyn}}} & \text{for traction,} \end{cases} \quad (2.20)$$

where  $r_{\text{dyn}}$  denotes the *dynamical tire radius*. It is defined by the rolling circumference  $U$  of a non-driven wheel, i.e.

$$r_{\text{dyn}} = \frac{U}{2\pi}. \quad (2.21)$$

In this definition the tire slip is always positive,  $s_x \in [0, 1]$ . Fig. 2.5 shows the friction coefficient  $\mu$  in dependence of the longitudinal tire slip  $s_x$ . The maximum friction coefficient  $\mu_h$  is reached at the *critical slip*  $s_{x,c}$  whose value is about 10%. At a tire slip larger than  $s_{x,c}$  the friction coefficient decreases, at pure gliding, i.e.  $s_x = 1$  the friction coefficient is  $\mu_g < \mu_h$ . Depending on the tire  $\mu_h \approx 1$  for dry roads and  $\mu_h \approx 0.8$  for wet roads.

The tire force in dependence of the tire slip can be expressed by e.g. the *Pacejka magic formula* which corresponds to a semi-empirical model, see [Pac02],

$$F_x = D \sin(C \arctan(Bs_x - E(Bs_x - \arctan Bs_x))). \quad (2.22)$$

From the stiffness factor  $B$  and the peak value  $D$  the shape and curvature factors  $C$  and  $E$  can be determined. The product  $BCD$  corresponds to the slope at the origin and denotes the tire stiffness.

## 2.3 Backlash models

Two different backlash models from the literature are presented in this section. The first one is the well-known dead-zone model and the second one represents a physical model.

### 2.3.1 Dead-zone model

The dead zone model represents the torque in dependence of the total angle of deflection  $\theta$  with a zero output zone around the origin, as shown in Fig. 2.6. Within the dead band no torque is transferred. For  $|\theta| \geq \alpha$  there is contact of the gear teeth. The dead-zone model does not include any damping. The angle  $\theta$  is composed of the deflection angle of the backlash  $\beta$  and the torsion angle  $\varphi$ , i.e.

$$\theta = \beta + \varphi. \quad (2.23)$$

The angle  $\beta$  is bounded by half of the backlash width, i.e.  $|\beta| \leq \alpha$ . The torque is calculated by

$$T_s = k_s(\theta - \beta). \quad (2.24)$$

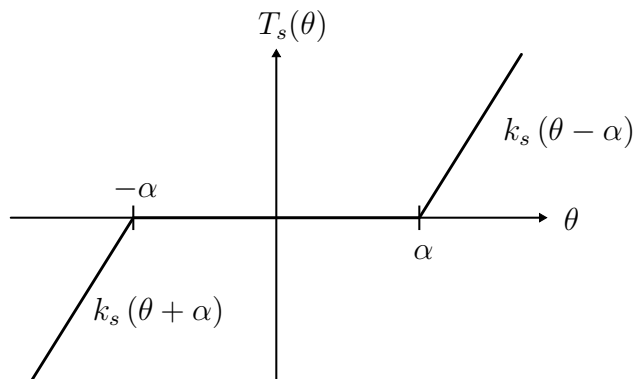


Figure 2.6: Dead zone model for the shaft torque  $T_s(\theta)$  in the presence of backlash of width  $2\alpha$ .

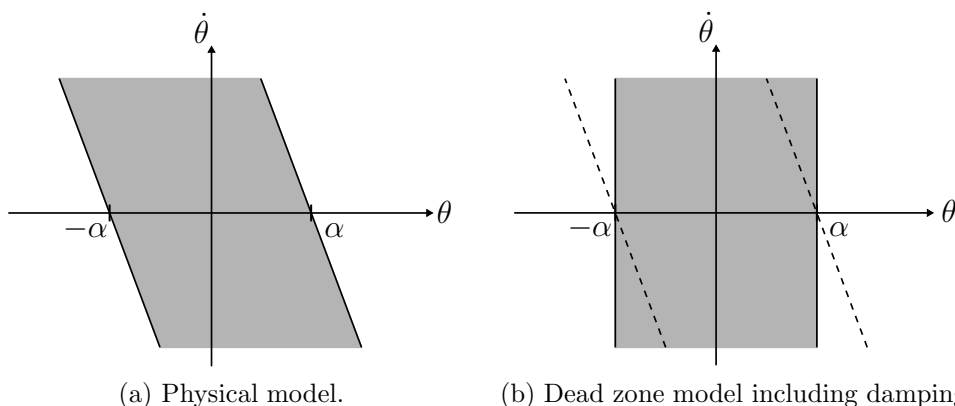


Figure 2.7: Phase plane plots of backlash models. Within the open set of the shaded area there is no contact of the gear teeth.

During the backlash phase  $\theta = \beta$  such that the shaft torque can be represented as

$$T_s(\theta) = \begin{cases} k_s(\theta - \alpha \operatorname{sgn}(\theta)) & \text{for } |\theta| > \alpha, \\ 0 & \text{for } |\theta| \leq \alpha. \end{cases} \quad (2.25)$$

### 2.3.2 Physical model

The physical backlash model combines an ideal backlash with an inertia-free elastic shaft with damping, see [NGG97]. The shaft torque  $T_s$  is calculated by

$$T_s = k_s(\theta - \beta) + d_s(\dot{\theta} - \dot{\beta}). \quad (2.26)$$

The coefficient  $d_s$  represents the viscous damping. For  $\beta = \alpha$  or  $\beta = -\alpha$  and  $\dot{\beta} = 0$  there is contact. Solving the right hand side of (2.26) for  $\dot{\theta}$  yields  $\dot{\theta} > -k_s/d_s \cdot (\theta - \alpha)$  for  $T_s > 0$  and  $\dot{\theta} < -k_s/d_s \cdot (\theta + \alpha)$  for  $T_s < 0$ . This separates the  $(\theta, \dot{\theta})$ -plane in three areas with straight lines of slope  $-k_s/d_s$  as

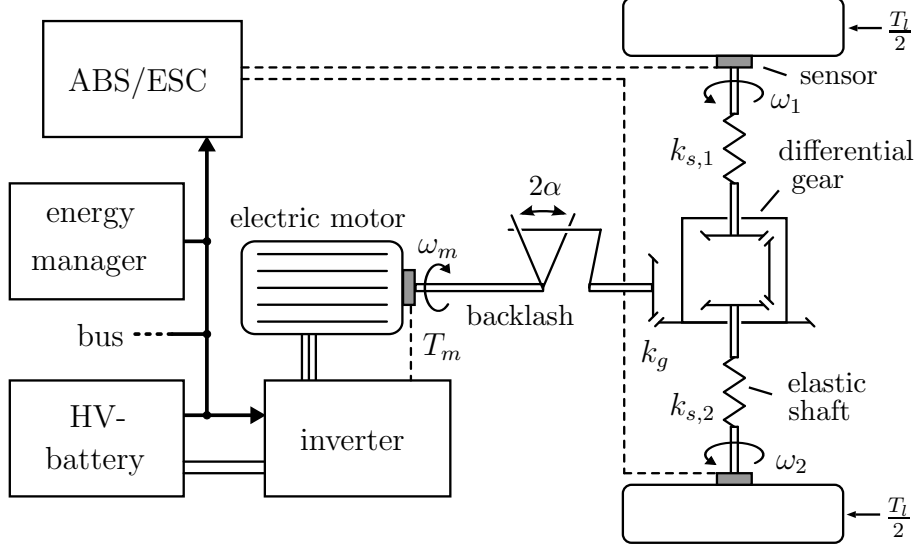


Figure 2.8: Power train of an electrically driven vehicle.

shown in Fig. 2.7(a). Within the open set defined by the shaded area there is no contact. Fig. 2.7(b) shows the  $(\theta, \dot{\theta})$ -plane for the dead zone model with a viscous damping term added which is significantly different from the physical model.

The dynamics of the backlash angle  $\beta$  is given by

$$\dot{\beta} = \begin{cases} \max(0, \dot{\theta} + \frac{k_s}{d_s}(\theta - \beta)) & \text{for } \beta = \alpha, \\ \dot{\theta} + \frac{k_s}{d_s}(\theta - \beta) & \text{for } |\beta| < \alpha, \\ \min(0, \dot{\theta} + \frac{k_s}{d_s}(\theta - \beta)) & \text{for } \beta = -\alpha. \end{cases} \quad (2.27)$$

## 2.4 Power-train modeling

Fig. 2.8 shows the power-train of an electrically driven vehicle. It consists of the EM, the backlash of width  $2\alpha$ , the differential gear with the gear ratio  $k_g$ , the elastic drive shafts and the wheels. Fig. 2.8 shows also ECUs interconnected via the vehicle's bus system, the angular sensor of the EM and the wheel speed sensors, which are processed by the ABS or ESC (Electronic Stability Control) ECU. The wheel angular velocities are denoted by  $\omega_1$  and  $\omega_2$ .

### 2.4.1 Two-mass system model

In this section the power-train is represented as a two-mass system. Therefore the wheels and the elasticities of the drive shafts are lumped. The backlash of the entire power train is lumped as well. An ideal differential gear is assumed such that the torques of the drive shafts are identical. The elasticity, which consists mainly of the elasticities of the drive shafts, is represented by a linear spring with

stiffness

$$k_s = k_{s,1} + k_{s,2}. \quad (2.28)$$

Viscous damping is assumed for the motor and the load. Then the differential equations of the power train can be summarized as<sup>2</sup>

$$\begin{aligned} \dot{\theta} &= \frac{\omega_m}{k_g} - \omega_l, \\ J_l \dot{\omega}_l &= T_s - d_l \omega_l - T_l, \\ J_m \dot{\omega}_m &= -\frac{T_s}{k_g} - d_m \omega_m + T_m, \end{aligned} \quad (2.29)$$

where  $J_m$  and  $J_l$  respectively denote the motor and load inertia. The angular velocities of motor and load are denoted by  $\omega_m$  and  $\omega_l$ , where the load angular velocity is the mean value of the corresponding left and right wheel angular velocities, i.e.

$$\omega_l = \frac{1}{2}(\omega_1 + \omega_2). \quad (2.30)$$

The damping coefficients  $d_m$  and  $d_l$  consider the viscous friction of the motor and the load. The motor inertia consists of the moments of inertia of the rotor and the differential gear.

### Load inertia

The load torque  $T_l$  represents the torque due to the tire-road contact forces as described in section 2.2. Neglecting the rolling resistance and the resistance due to the road gradient the load torque can be expressed with respect to the acceleration force, i.e.

$$T_l = F_{\text{acc}} r_{\text{st}}. \quad (2.31)$$

Assuming small tire slip the longitudinal vehicle speed  $v_x$  can be approximated by  $v_x \approx \omega_l r_{\text{dyn}}$ . Then the acceleration force can be expressed as

$$F_{\text{acc}} = m_v \dot{v}_x \approx m_v r_{\text{dyn}} \dot{\omega}_l, \quad (2.32)$$

where  $m_v$  denotes the vehicle mass. Inserting (2.31) and (2.32) into the second equation of (2.29) the load torque can be considered in the load inertia, i.e.

$$J_l = 2J_w + m_v r_{\text{dyn}} r_{\text{st}}, \quad (2.33)$$

where  $J_w$  corresponds to the wheel inertia.

---

<sup>2</sup>The load angular position can not be measured with an automotive wheel speed sensor. Therefore the difference angle between motor and load angular position  $\theta_m$  and  $\theta_l$  is used for system representation, i.e.  $\theta = \frac{\theta_m}{k_g} - \theta_l$ .

## Nonlinear state-space representation

Combining the state variables in the vector

$$\mathbf{x} = \begin{bmatrix} \theta \\ \omega_l \\ \omega_m \end{bmatrix}, \quad (2.34)$$

the differential equations in (2.29) can be expressed in state-space form as

$$\begin{aligned} \dot{\mathbf{x}} &= \mathbf{f}(\mathbf{x}) + \mathbf{b}u + \mathbf{m}w \\ \mathbf{y} &= \mathbf{C}\mathbf{x}, \end{aligned} \quad (2.35)$$

where  $u = T_m$  and  $w = T_l$  denote the *known* and *unknown* input respectively. The backlash is modeled as a dead-zone model as described in section 2.3 and the shaft torque is calculated according to (2.25). Then the nonlinear function  $\mathbf{f}(\mathbf{x})$ , the vectors corresponding to the known and unknown input  $\mathbf{b}$  and  $\mathbf{m}$  are

$$\begin{aligned} \mathbf{f}(\mathbf{x}) &= \begin{bmatrix} \frac{\omega_m}{k_g} - \omega_l \\ -\frac{d_l}{J_l}\omega_l + \frac{1}{J_l}T_s(\theta) \\ -\frac{d_m}{J_m}\omega_m - \frac{1}{k_g J_m}T_s(\theta) \end{bmatrix}, \\ \mathbf{b} &= \begin{bmatrix} 0 \\ 0 \\ \frac{1}{J_m} \end{bmatrix}, \quad \mathbf{m} = \begin{bmatrix} 0 \\ -\frac{1}{J_l} \\ 0 \end{bmatrix}. \end{aligned}$$

It is assumed that the measured signals are the motor angular speed and the wheel angular velocities. With (2.30) the output matrix is

$$\mathbf{C} = \begin{bmatrix} 0 & 1 & 0 \\ 0 & 0 & 1 \end{bmatrix}. \quad (2.36)$$

## Backlash representation as a combination of a linear and nonlinear function

In [HK07] the dead zone model representation  $T_s(\theta)$  according to (2.25) is expressed as the combination of a linear and nonlinear function in  $\theta$ , i.e.

$$T_s(\theta) = k_s \theta - k_s \xi(\theta), \quad (2.37)$$

where

$$\xi(\theta) = \begin{cases} \theta & \text{for } \theta \leq \alpha, \\ \alpha \operatorname{sgn}(\theta) & \text{for } \theta > \alpha. \end{cases} \quad (2.38)$$

The function  $\xi(\theta)$  is shown in Fig. 2.9. With (2.37) the nonlinear state-space model (2.35) can be expressed as the sum of a linear system and a nonlinear vector  $\mathbf{g}\xi(\theta)$ , i.e.

$$\begin{aligned} \dot{\mathbf{x}} &= \mathbf{A}\mathbf{x} + \mathbf{b}u + \mathbf{m}w + \mathbf{g}\xi(\theta), \\ \mathbf{y} &= \mathbf{C}\mathbf{x}. \end{aligned} \quad (2.39)$$

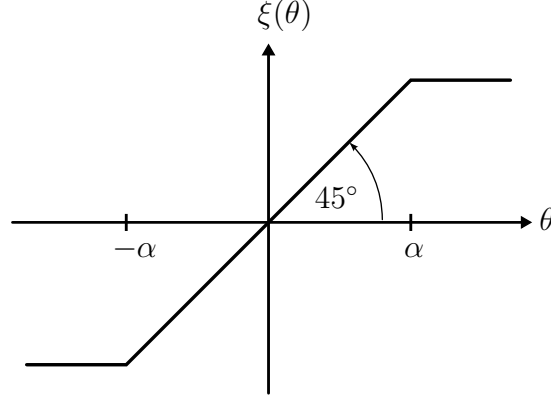


Figure 2.9: Nonlinear function  $\xi(\theta)$  for correcting a linear function in  $\theta$  in order to model the effect of backlash.

The vector  $\mathbf{g}$  corresponds to the negative first column of the matrix  $\mathbf{A}$ . They are

$$\mathbf{A} = \begin{bmatrix} 0 & -1 & \frac{1}{k_g} \\ \frac{k_s}{J_l} & -\frac{d_l}{J_l} & 0 \\ -\frac{k_s}{k_g J_m} & 0 & -\frac{d_m}{J_m} \end{bmatrix}, \quad \mathbf{g} = \begin{bmatrix} 0 \\ -\frac{k_s}{J_l} \\ \frac{k_s}{k_g J_m} \end{bmatrix}.$$

In the backlash and contact phase the system (2.39) describes different systems. In the backlash phase no torque can be transmitted, i.e.  $\theta = \xi(\theta)$ . The nonlinear part of (2.39) and the first column of the matrix  $\mathbf{A}$  cancel out each other. Then (2.39) corresponds to

$$\begin{aligned} \dot{\mathbf{x}} &= \mathbf{A}_{\text{bl}}\mathbf{x} + \mathbf{b}u + \mathbf{m}w, \\ \mathbf{y} &= \mathbf{C}\mathbf{x}, \end{aligned} \tag{2.40}$$

where

$$\mathbf{A}_{\text{bl}} = \begin{bmatrix} 0 & -1 & \frac{1}{k_g} \\ 0 & -\frac{d_l}{J_l} & 0 \\ 0 & 0 & -\frac{d_m}{J_m} \end{bmatrix}.$$

## 2.4.2 Synthesis model

Due to cost reasons no angle encoders are present which would measure the overall backlash angle  $\beta$ . It cannot be reconstructed for example by an observer, i.e. the pair  $(\mathbf{C}, \mathbf{A}_{\text{bl}})$  according to (2.36) and (2.40) is neither observable nor detectable<sup>3</sup>.

Due to the spread of series production and different ambient conditions the backlash width is not exactly known. This requires an algorithm for the estimation of the backlash width, such as presented in [LE07]. Due to the high torsional stiffness  $k_s$  the estimation of the backlash width  $2\hat{\alpha}$  has to be exact for the application in a state observer.

---

<sup>3</sup>Detectability means that the non-observable modes are stable.

In automotive applications the control concepts should be simple and robust. Therefore in this thesis a linear synthesis model neglecting the backlash is proposed. This allows the design of the state observer and the controller to be independently of backlash width. The state variable  $\varphi$  instead of  $\theta$  is used to indicate that the backlash is not considered in the model. The shaft torque can be retrieved according to (2.1). The state vector corresponds to

$$\mathbf{x} = \begin{bmatrix} \varphi \\ \omega_l \\ \omega_m \end{bmatrix}^T. \quad (2.41)$$

### Synthesis Model

The *synthesis model* is represented by

$$\begin{aligned} \dot{\mathbf{x}} &= \mathbf{A}\mathbf{x} + \mathbf{b}u + \mathbf{m}w, \\ \mathbf{y} &= \mathbf{C}\mathbf{x}, \end{aligned} \quad (2.42)$$

where the system matrix  $\mathbf{A}$  is

$$\mathbf{A} = \begin{bmatrix} 0 & -1 & \frac{1}{k_g} \\ \frac{k_s}{J_l} & -\frac{d_s+d_l}{J_l} & \frac{d_s}{J_l k_g} \\ -\frac{k_s}{J_m k_g} & \frac{d_s}{J_m k_g} & -\frac{1}{J_m} \left( \frac{d_s}{k_g^2} + d_m \right) \end{bmatrix}.$$

## 2.5 Wheel speed sensor and bus model

### 2.5.1 Automotive wheel speed sensor

The wheel speed sensors of passenger vehicles are integrated in the wheel bearing at the hub, see [Rei12b]. They consist of a sensor element and a magnetic multi-pole ring with  $N_0 = 48$  alternating magnetic units which are made of synthetic material with ferromagnetic powder on a non-magnetic metallic wheel. Fig. 2.10 shows schematically a wheel speed sensor with multi-pole ring.

The sensor consists of a Hall sensor element and an integrated circuit (IC) which are encapsulated in plastic material. The integrated circuit generates pulses from the Hall voltage. The sensor IC is connected to the ABS or ESP ECU by a current interface. Additional information such as direction of rotation, sensor error or standstill is modulated onto the pulse width.

### 2.5.2 Wheel speed sensor model

The sensor is modeled as an incremental encoder. The angular velocity signal of the wheel rim, denoted by  $\omega_r$ , is calculated by numerical approximation of the

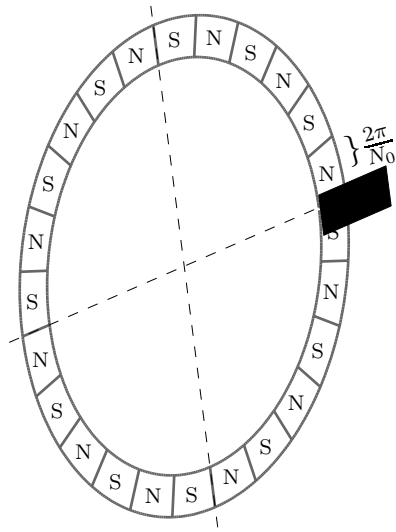


Figure 2.10: Automotive wheel speed sensor with magnetic multi pole ring.

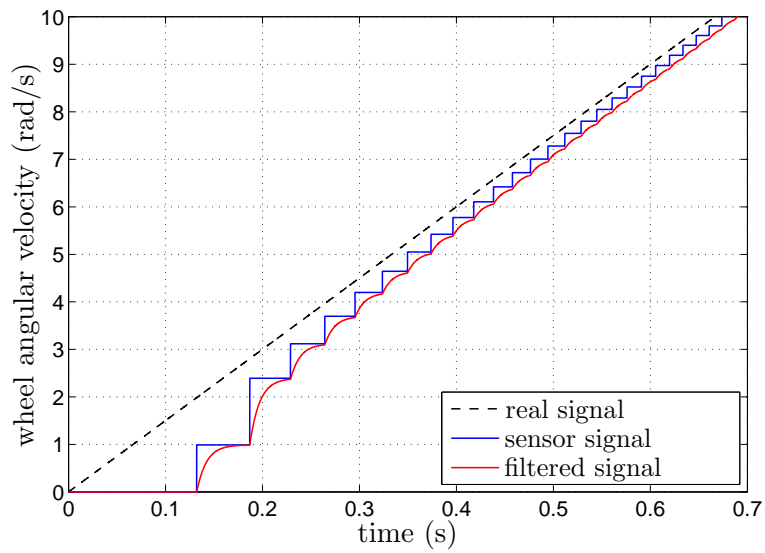


Figure 2.11: Real wheel angular velocity, output of the sensor model and subsequently filtered signal.

time-derivative of the rotation angle, i.e

$$\omega_r \approx \frac{\Delta\phi}{\Delta t}, \quad (2.43)$$

where  $\Delta\phi$  and  $\Delta t$  denote the angle and the time interval respectively. Depending on the method, as shown in [FPL12], the numerator or the denominator in (2.43) can be fixed for calculating the angular velocity value. If the measurement time  $\Delta t$  is fixed the corresponding angle has to be determined<sup>4</sup>. If the angle  $\Delta\phi$  is fixed the time for traversing a predefined number of increments or magnetic units has to be measured<sup>5</sup>. The time measurement can be accomplished with the help of a counter running at a high sampling frequency  $f_0$ . This method is preferred since it results in a smaller relative quantization error  $e_{\text{rel}}$  at low velocities, i.e.

$$e_{\text{rel}} \leq \frac{\omega_{r,s}}{\Delta\phi f_0}, \quad (2.44)$$

where  $\omega_{r,s}$  corresponds to the sensor angular velocity signal and  $\Delta\phi$  corresponds to the angle of  $N \in \mathbb{N}$  consecutive segments of the multi-pole ring, i.e.

$$\Delta\phi = N \frac{2\pi}{N_0}. \quad (2.45)$$

In the sensor model the sampling frequency was chosen as  $f_0 = 10$  kHz. In general the measured signal  $\omega_{r,s}$  is subsequently filtered. Fig. 2.11 shows the real angular velocity signal of the wheel rim  $\omega_r$ , the output of the wheel speed sensor model  $\omega_{r,s}$  and the filtered signal of the model for which a first-order low-pass filter with time constant  $\tau_f = 10$  ms has been used.

The measurement principle introduces a delay of  $\omega_{r,s}$ . Assuming that the angular velocity changes slowly the delay of the measured signal can be approximated by  $\Delta t/2$ . Due to the filter only the lower frequencies are transferred. There is an additional delay due to the *zero order hold*. For a sinusoidal signal the delay of a *zero order hold* can be approximated by  $\Delta t/2$ , see [Lun13]. The delay introduced by the filter can be approximated by the group delay at zero frequency  $t_{gr}|_{\omega=0}$ .

### 2.5.3 Bus model

In general the power-train control algorithm is implemented in a separate ECU, such as an inverter. It is connected to the vehicle's bus system where the wheel speed information is provided. Due to the bus transmission the wheel speed information is affected by an additional delay.

With a Controller Area Network (CAN) bus system the delay cannot be determined exactly since the bus system is event-driven. Although the wheel speed information is provided with a high priority, the tasks of the sender and receiver

---

<sup>4</sup>This method is also called chronologically synchronous acquisition.

<sup>5</sup>This method is also called angular synchronous acquisition.

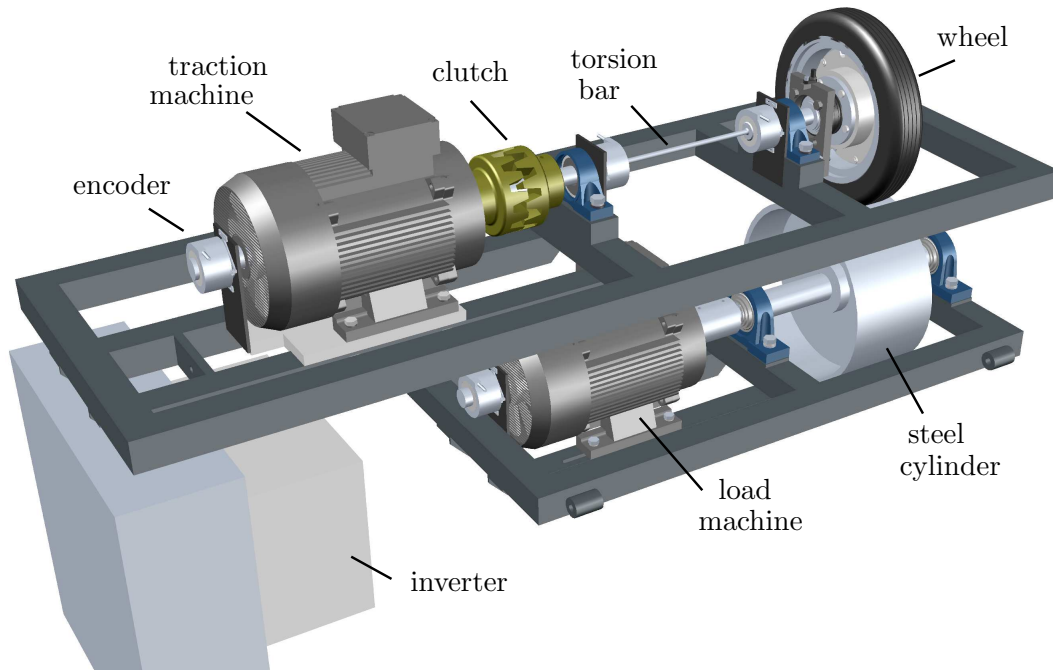


Figure 2.12: Test bench for investigating power train control concepts.

ECU are not synchronized. With a time-triggered bus system implementing the Time Division Multiple Access (TDMA) strategy, such as *FlexRay<sup>TM</sup>*, the software tasks can be synchronized and the transmission delay is constant, see [Rei12a].

The bus model implements a constant transmission delay  $\tau_b$ . In general the bus update time is higher than the cycle time of the software task implementing the control algorithm. This is modeled by a *sampler* and a *zero order hold*.

## 2.6 Test bench model

### 2.6.1 Test bench description

Fig. 2.12 shows the test bench built for investigating the power train control concepts. The upper part represents the power train of a single axle of an electrically driven vehicle. It consists of the traction motor, a claw coupling, the torsion bar and the wheel. The claw coupling represents the gear play within the power-train. The motor can be moved horizontally such that the backlash angle of the coupling has a predefined value between zero and ten degrees. The torsion bar represents the drive shaft and is attached between two ball bearings. Its stiffness is well known from geometrical dimensions and from the steel properties. The lower part can be adjusted in height statically such that the vertical force between tire and metal cylinder, which represents the road, can be adjusted. By changing the cylinder's horizontal position two different friction values are available. The lower motor can be used to apply additional load torques or disturbances.

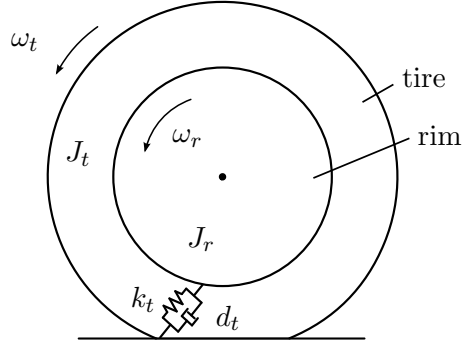


Figure 2.13: Tire modeled as an elastic element with stiffness and damping coefficient  $k_t$  and  $d_t$ .

High resolution sensors for angular position and speed measurement are located at the motors and at both ends of the torsion bar. The two motors are identical induction machines (IM) with squirrel cage rotor with a nominal torque of 55 N m. They are driven by 9 kW ACOPOS inverters from B&R<sup>6</sup> using three phase voltage of 400 V<sub>eff</sub>.

The parameters of the mechanical parts, such as the moment of inertia of the rotor of the EM, the clutch and the metal cylinder are known from CAD modeling. The test bench is described in more detail in chapter 5. For details on the motor, the inverter and the parameters of the test bench see appendix C.

## 2.6.2 Tire model

As in [MW04] the tire is modeled as a torsional elastic element as shown in Fig. 2.13. The torque  $T_t$  at the tire is represented by

$$T_t = k_t \varphi_t + d_t \dot{\varphi}_t, \quad (2.46)$$

where  $\varphi_t$  corresponds to the tire torsion angle and  $k_t$  and  $d_t$  denote the stiffness and damping coefficient of the tire respectively. The inertias of the wheel rim and the tire are denoted by  $J_r$  and  $J_t$  respectively. The traction force between tire and cylinder corresponds to a nonlinear function of the longitudinal tire slip  $s_x$ . According to Fig. 2.4 the longitudinal tire force  $F_x$  is

$$F_x = \frac{T_t}{r_{st}} - F_r, \quad (2.47)$$

where  $F_r$  and  $r_{st}$  denote the rolling resistance and the statical tire radius.

## 2.6.3 Backlash model

The physical backlash model from section 2.3.2 is applied. The backlash angle  $\beta$  is calculated with an integrator with saturation. The conditions  $\beta = \pm\alpha$  and

---

<sup>6</sup>www.brautomation.com

$|\beta| < \alpha$  are used to distinguish the cases in (2.27). Then the shaft torque is calculated with (2.26).

## 2.6.4 Model of the EM

The torque dynamics of the induction machine is approximated by a second-order transfer function. It corresponds to (2.13) and its parameterization can be found in Tab. C.13.

## 2.6.5 Differential equations

The shaft and the tire represent the main elasticities such that the test bench corresponds to a three-mass system. It is described by the differential equations

$$\begin{aligned}
\dot{\theta} &= \omega_m - \omega_r, \\
J_m \dot{\omega}_m &= T_m - T_s - d_m \omega_m, \\
J_r \dot{\omega}_r &= T_s - T_t, \\
\dot{\varphi}_t &= \omega_r - \omega_t, \\
J_t \dot{\omega}_t &= T_t - F_x r_{st} - F_r(|\omega_t|) \operatorname{sgn}(\omega_t) r_{st}, \\
J_c \dot{\omega}_c &= F_x r_c - d_c \omega_c - T_l,
\end{aligned} \tag{2.48}$$

where  $\omega_r$ ,  $\omega_t$  and  $\omega_c$  correspond to the angular velocities of the wheel rim, the tire and the cylinder respectively. The torques at the shaft and at the tire are calculated according to (2.26) and (2.46). The inertias of the wheel rim, the tire and the steel cylinder are denoted as  $J_r$ ,  $J_t$  and  $J_c$ . The radius of the steel cylinder is denoted by  $r_c$ . The viscous damping at the motor and at the cylinder is considered by the damping coefficients  $d_m$  and  $d_c$ . The rolling resistance  $F_r(\omega_t)$  is represented in dependence of the positive tire angular velocity as shown in Fig. 5.5.

The longitudinal tire force in dependence of the tire slip is represented as shown in Fig. 5.6. The tire slip is calculated according to (2.20). The rolling resistance and the longitudinal tire force were evaluated experimentally.

# Chapter 3

## Power-Train State Estimation

The shaft torque in the power-train of series passenger vehicles is not measured due to costly sensor equipment. The torque therefore has to be estimated via appropriate methods. The backlash within the power-train is in general distributed and of unknown width. In the contact phase, i.e. when the backlash gap is closed, the power-train model is *observable* and the shaft torque can be estimated with the help of a state observer.

Since the synthesis model of section 2.4.2 has been chosen to be linear the observer design will focus on linear time-invariant (LTI) systems. The computational effort of the observer should be small. For this reason the designed observers are based on first-order sliding mode techniques. For the observer implementation a basic method for chattering reduction is applied. In order to estimate the shaft torque exactly, the unknown load torque has additionally to be estimated. The observer design involves a simple *disturbance model*.

In the observer design the measurement of the ideal motor and load angular velocities is presumed. The wheel speed information is of poor quality at low angular velocities and therefore cannot be used reliably in a state observer. The impact on the observability is analyzed by means of observability measures.

The sliding mode observer concept is extended for the case that a part of the sensor signals is only available with delay and a limited update rate. The extension incorporates a linear correction term of the delayed measurements such as the wheel speed information which is available on the vehicle's bus system. The stability determination of the observer error dynamics a *Linear Matrix Inequality* has to be solved.

For the measurement of the ideal motor and load angular velocities the synthesis model (2.40) fulfills the so-called *strong observability condition* with respect to the *unknown input*. A second-order sliding mode *unknown input observer* is applied for state estimation. It allows the estimation of the shaft torque despite an unknown load torque.

## 3.1 Observability

### 3.1.1 Definition and criteria

Consider a continuous-time LTI system with disturbance  $w$  and initial state  $\mathbf{x}(t=0) = \mathbf{x}_0$ ,

$$\begin{aligned}\dot{\mathbf{x}} &= \mathbf{A}\mathbf{x} + \mathbf{b}u + \mathbf{m}w, \\ \mathbf{y} &= \mathbf{C}\mathbf{x},\end{aligned}\tag{3.1}$$

with  $\mathbf{x} \in \mathbb{R}^n$ ,  $\mathbf{y} \in \mathbb{R}^r$ , and  $u, w \in \mathbb{R}$ . The definition of observability of an LTI system is given e.g. in [ZDG96].

**Definition:** System (3.1) is *observable* if, for any  $t_1 > 0$  the initial state  $\mathbf{x}_0$  can be calculated from the output  $\mathbf{y}(t)$  and the input  $u(t)$  within the finite time interval  $[0, t_1]$ .

In [ZDG96] criteria for the observability of LTI systems are given:

1. System (3.1) is observable if and only if the observability matrix  $\mathbf{B}_y$  has full column rank  $n$ , i.e.

$$\text{rank } \mathbf{B}_y = \text{rank} \begin{bmatrix} \mathbf{C} \\ \mathbf{C}\mathbf{A} \\ \vdots \\ \mathbf{C}\mathbf{A}^{n-1} \end{bmatrix} = n.\tag{3.2}$$

2. System (3.1) is observable if and only if the *observability Gramian*  $\mathbf{W}_o(t)$  is positive definite for any  $t > 0$ , i.e.

$$\mathbf{W}_o(t) := \int_0^t e^{\mathbf{A}^T\tau} \mathbf{C}^T \mathbf{C} e^{\mathbf{A}\tau} d\tau \succ 0,\tag{3.3}$$

where the matrix  $e^{\mathbf{A}\tau}$  denotes the *state transition matrix*.

3. System (3.1) is observable if and only if

$$\mathbf{C}\mathbf{p}_{ij} \neq \mathbf{0},\tag{3.4}$$

where  $\mathbf{p}_{ij}$  corresponds to a (linearly independent) eigenvector of the eigenvalue  $s_i$  of  $\mathbf{A}$  with multiplicity  $k$ ,  $j \leq k$ , i.e.

$$\mathbf{A}\mathbf{p}_{ij} = s_i\mathbf{p}_{ij}, \quad i = 1, \dots, m \leq n.\tag{3.5}$$

4. System (3.1) is observable if and only if the eigenvalues of  $(\mathbf{A} + \mathbf{L}\mathbf{C})$  can be assigned arbitrary.

**Definition:** [Hau83] System (3.1) is *strongly observable* if for any initial state  $\mathbf{x}_0$  and  $w \equiv 0$ ,  $\mathbf{y}(t) \equiv 0$  implies  $\mathbf{x}(t) \equiv 0$ .

### 3.1.2 Observability measures

Due to the low resolution of the automotive wheel speed sensors their signal cannot be used for state estimation at small vehicle speeds. Therefore the question arises if the observability significantly deteriorates if only the motor angular velocity signal is considered for measurement in an observer. In order to evaluate the degree of observability so-called observability measures were introduced. In [Mos11] controllability measures for LTI systems are analyzed. Because of duality these measures can be applied to observability. In the following section a short overview of well-known measures is given.

#### Observability measure according to Litz

The observability measure according to *Litz* is based on the diagonal form. Assuming that the system matrix  $\mathbf{A}$  is diagonalizable, the system (3.1) can be transformed into the *canonical form* via the state transformation

$$\mathbf{z} = \mathbf{V}\mathbf{x}, \quad (3.6)$$

where  $\mathbf{V} = [\mathbf{p}_1, \dots, \mathbf{p}_n]$  denotes the matrix of eigenvectors. The transformed system reads as

$$\begin{aligned} \dot{\mathbf{z}} &= \mathbf{diag}(s_i)\mathbf{z} + \tilde{\mathbf{b}}u, \\ \mathbf{y} &= \tilde{\mathbf{C}}\mathbf{z}, \end{aligned} \quad (3.7)$$

where  $\mathbf{diag}(s_i) = \mathbf{V}^{-1}\mathbf{A}\mathbf{V}$ ,  $\tilde{\mathbf{b}} = \mathbf{V}^{-1}\mathbf{b}$  and  $\tilde{\mathbf{C}} = \mathbf{C}\mathbf{V}$ .

The system (3.1) is observable if and only if the output matrix  $\tilde{\mathbf{C}}$  has no zero column which means that  $\mathbf{C}\mathbf{p}_i \neq \mathbf{0}$ ,  $i = 1, \dots, n$ . Small values in the  $i$ -th column of the transformed output matrix  $\tilde{\mathbf{C}}$  indicate 'poor' observability of the corresponding eigenvalue. The measure according to Litz is defined as

$$\kappa_i = \frac{\mathbf{p}_i^* \mathbf{C}^T \mathbf{C} \mathbf{p}_i}{\mathbf{p}_i^* \mathbf{p}_i}, \quad i = 1, \dots, n, \quad (3.8)$$

where  $\mathbf{p}_i^*$  denotes the conjugate transpose of  $\mathbf{p}_i$ .

#### Observability measure according to Benninger and Rivoir

The controllability measure according to *Benninger and Rivoir*, see [BR86], is based on the minimal energy required to steer an initial state  $\mathbf{x}_0$  to the origin  $\mathbf{x} = \mathbf{0}$ . Applied to observability the measure is defined as

$$m_i = \frac{1}{\sqrt{\left(\tilde{\mathbf{W}}_o^{-1}(t)\right)_{ii}}}, \quad i = 1, \dots, n, \quad (3.9)$$

Table 3.1: Observability measure according to Litz.

$y_1 = \omega_m$	$\kappa_1 = 0.5$
	$\kappa_2 = 0.637$
	$\kappa_3 = 0.637$
$\mathbf{y}_2 = [\omega_m, \omega_l]$	$\kappa_1 = 1.0$
	$\kappa_2 = 1.0$
	$\kappa_3 = 1.0$

where  $(\tilde{\mathbf{W}}_o^{-1}(t))_{ii}$  denotes the  $i$ -th main diagonal element of the inverse observability Gramian, where

$$\tilde{\mathbf{W}}_o(t) = \int_0^t e^{-\mathbf{A}^T \tau} \mathbf{C}^T \mathbf{C} e^{-\mathbf{A} \tau} d\tau. \quad (3.10)$$

The minimal control energy of the dual system of (3.1) corresponds to

$$W_{\min}(t) = \mathbf{x}_0^T \tilde{\mathbf{W}}_o^{-1} \mathbf{x}_0. \quad (3.11)$$

The definition of the Observability Gramian according to (3.10) is based on the inverse *state transition matrix* such that for a stable system matrix  $\mathbf{A}$  the measure (3.9) will tend to infinity as the integration time goes to infinity. This means that no control energy is needed for stabilizing the dual system of (3.1).

### Analysis of the synthesis model

In this section the observability of the synthesis model (2.42) is analyzed for two sensor configurations. In the first configuration the only measured output is the motor angular velocity, i.e

$$y_1 = \omega_m = \mathbf{C}_1 \mathbf{x}, \quad \mathbf{C}_1 = [0 \ 0 \ 1]. \quad (3.12)$$

In the second configuration the motor and the load angular velocities are measured, i.e.

$$\mathbf{y}_2 = \begin{bmatrix} \omega_l \\ \omega_m \end{bmatrix} = \mathbf{C}_2 \mathbf{x}, \quad \mathbf{C}_2 = \begin{bmatrix} 0 & 1 & 0 \\ 0 & 0 & 1 \end{bmatrix}. \quad (3.13)$$

For the analysis it is assumed that the disturbance input  $w \equiv 0$  since external disturbances are not considered with the investigated measures. The parameters correspond to them of the test bench, see Tab. C.3. For both sensor configurations the corresponding observability matrix (3.2) has full rank.

The results of the observability measure according to Litz for the two sensor configurations are shown in Tab. 3.1. The values  $\kappa_2$  and  $\kappa_3$  belong to the complex conjugate eigenvalues. The measure has no significant dependence on the damping coefficient  $d_s$ .

Table 3.2: Observability measure according to Benninger and Rivoir with damping coefficient  $d_s = 1$ .

$y_1 = \omega_m$	$m_1 = 98.64$
	$m_2 = 0.31$
	$m_3 = 0.28$
$\mathbf{y}_2 = [\omega_m, \omega_l]$	$m_1 = 123.86$
	$m_2 = 0.42$
	$m_3 = 0.4$

Table 3.3: Observability measure according to Benninger and Rivoir with damping coefficient  $d_s = 0$ .

$y_1 = \omega_m$	$m_1 = 32.01$
	$m_2 = 0.22$
	$m_3 = 0.18$
$\mathbf{y}_2 = [\omega_m, \omega_l]$	$m_1 = 40.09$
	$m_2 = 0.29$
	$m_3 = 0.24$

For the measure (3.9) according to Benninger and Rivoir it is not necessary to compute the integral (3.10). Eq. (3.10) fulfills the *Lyapunov differential equation*

$$\dot{\tilde{\mathbf{W}}}_o(t) = -\mathbf{A}^T \tilde{\mathbf{W}}_o(t) - \tilde{\mathbf{W}}_o(t) \mathbf{A} + \mathbf{C}^T \mathbf{C}, \quad (3.14)$$

with the initial condition  $\tilde{\mathbf{W}}_o(0) = \mathbf{0}$ . Eq. (3.14) was evaluated numerically using Matlab/Simulink<sup>1</sup>. The simulation was performed with a step size of 1 ms by the *Runge-Kutta* integration method, see e.g. [Kre93]. In [BR86] it is proposed to choose the integration time of (3.10) in the magnitude of the dominant time constant of the system which corresponds to 2.3 s. For (2.42) this yields large values of the measure for the case that the damping coefficient  $d_s = 1$ . Therefore the integration time was chosen as 0.1 s.

Tab. 3.2 and Tab. 3.3 show the results of the measure (3.9) according to Benninger and Rivoir. The two tables compare the influence of the damping coefficient  $d_s$ .

<sup>1</sup>www.mathworks.com

## 3.2 First-order sliding mode observers

### 3.2.1 Sliding mode observer for LTI systems

Consider an observable continuous-time linear, time-invariant (LTI) system with *unknown* disturbance  $w$

$$\begin{aligned}\dot{\mathbf{x}} &= \mathbf{A}\mathbf{x} + \mathbf{b}u + \mathbf{d}w, \\ \mathbf{y} &= \mathbf{C}\mathbf{x},\end{aligned}\tag{3.15}$$

with  $\mathbf{x} \in \mathbb{R}^n$ ,  $\mathbf{y} \in \mathbb{R}^r$ ,  $u, w \in \mathbb{R}$ . In order to estimate the state  $\mathbf{x}$  and the *unknown* input  $w$ , system (3.15) is augmented by a disturbance model. The disturbance is assumed to be constant, i.e.  $\dot{w} = 0$ . With the augmented state vector  $\bar{\mathbf{x}}^T = [w \ \mathbf{x}^T]$  with  $\mathbf{x} \in \mathbb{R}^{\bar{n} \times 1}$ , where  $\bar{n} = n + 1$ , the model has the form

$$\begin{aligned}\dot{\bar{\mathbf{x}}} &= \bar{\mathbf{A}}\bar{\mathbf{x}} + \bar{\mathbf{b}}u, \\ \mathbf{y} &= \bar{\mathbf{C}}\bar{\mathbf{x}}.\end{aligned}\tag{3.16}$$

#### Observer design

It is assumed that  $\text{rank}(\bar{\mathbf{C}}) = r$  and  $\bar{\mathbf{C}} = [\mathbf{0} \ \mathbf{C}]$ . The augmented system (3.16) is observable if and only if the eigenvalues of the matrix

$$(\bar{\mathbf{A}} + \bar{\mathbf{L}}\bar{\mathbf{C}}) = \begin{bmatrix} 0 & \mathbf{I}^T \mathbf{C} \\ \mathbf{d} & \mathbf{A} + \mathbf{L}\mathbf{C} \end{bmatrix}\tag{3.17}$$

can be assigned arbitrary, where  $\bar{\mathbf{L}}^T = [\mathbf{I} \ \mathbf{L}^T]$  denotes the observer gain matrix with  $\mathbf{I}^T \in \mathbb{R}^{1 \times r}$  and  $\mathbf{L} \in \mathbb{R}^{n \times r}$ . Such an observer is also called a *proportional integral* (PI) observer, see [BS88].

For the design of the sliding mode observer the state variables have to be reordered such that the last  $r$  states are the measured states, i.e.

$$\bar{\mathbf{x}} = \begin{bmatrix} \mathbf{x}_1 \\ \mathbf{y} \end{bmatrix}\tag{3.18}$$

with  $\mathbf{x}_1 \in \mathbb{R}^{\bar{n}-r}$ . This can be accomplished by a linear state transformation

$$\mathbf{T}\bar{\mathbf{A}}\mathbf{T}^{-1} = \begin{bmatrix} \mathbf{A}_{11} & \mathbf{A}_{12} \\ \mathbf{A}_{21} & \mathbf{A}_{22} \end{bmatrix}, \quad \mathbf{T}\bar{\mathbf{b}} = \begin{bmatrix} \mathbf{b}_1 \\ \mathbf{b}_2 \end{bmatrix},\tag{3.19}$$

with the regular matrix

$$\mathbf{T} = \begin{bmatrix} \mathbf{N} \\ \bar{\mathbf{C}} \end{bmatrix},$$

where the rows of  $\mathbf{N}$  span the null space of  $\bar{\mathbf{C}}$ . Then the state-space model (3.15) has the following form:

$$\begin{aligned}\dot{\mathbf{x}}_1 &= \mathbf{A}_{11}\mathbf{x}_1 + \mathbf{A}_{12}\mathbf{y} + \mathbf{b}_1u, \\ \dot{\mathbf{y}} &= \mathbf{A}_{21}\mathbf{x}_1 + \mathbf{A}_{22}\mathbf{y} + \mathbf{b}_2u.\end{aligned}\tag{3.20}$$

For the system (3.20), the sliding mode observer has the form [UGS09]:

$$\begin{aligned}
\dot{\hat{\mathbf{x}}}_1 &= \mathbf{A}_{11}\hat{\mathbf{x}}_1 + \mathbf{A}_{12}\hat{\mathbf{y}} + \mathbf{b}_1u + \mathbf{L}\mathbf{v}, \\
\dot{\hat{\mathbf{y}}} &= \mathbf{A}_{21}\hat{\mathbf{x}}_1 + \mathbf{A}_{22}\hat{\mathbf{y}} + \mathbf{b}_2u - \mathbf{v}, \\
\mathbf{v} &= \mathbf{M}\mathbf{sgn}(\hat{\mathbf{y}} - \mathbf{y}), \\
\mathbf{M} &= \mathbf{diag}(M_i), \quad i = 1, \dots, r,
\end{aligned} \tag{3.21}$$

where  $\mathbf{sgn}(\cdot)$  denotes the vector-valued sign function which defines  $r$  *sliding surfaces*

$$\sigma_i = \hat{y}_i - y_i, \quad i = 1, \dots, r. \tag{3.22}$$

The constant elements  $M_i$  of the  $r$ -dimensional diagonal matrix  $\mathbf{M}$  have to be strictly positive and sufficiently large such that sliding mode is enforced on each surface of (3.22). Finite time convergence within

$$t_{e,i} = |\sigma_i(0)|/\eta_i \tag{3.23}$$

is ensured to  $\sigma_i = 0$  for the initial conditions  $\sigma_i(0)$  if

$$\dot{\sigma}_i \mathbf{sgn}(\sigma_i) < -\eta_i, \quad \eta_i > 0. \tag{3.24}$$

In sliding mode the error of the measured states  $\mathbf{e}_y = \mathbf{y} - \hat{\mathbf{y}}$  and its derivative  $\dot{\mathbf{e}}_y = \dot{\hat{\mathbf{y}}} - \dot{\mathbf{y}}$  vanish. The equivalent control method yields  $\mathbf{v}_{eq} = \mathbf{A}_{21}\mathbf{e}_{x_1}$ , where  $\mathbf{e}_{x_1} = \hat{\mathbf{x}}_1 - \mathbf{x}_1$  denotes the error of the not measurable states. The observer gain matrix  $\mathbf{L} \in \mathbb{R}^{(n-r) \times r}$  has to be chosen such that the error dynamics

$$\dot{\mathbf{e}}_{x_1} = (\mathbf{A}_{11} + \mathbf{L}\mathbf{A}_{21})\mathbf{e}_{x_1} \tag{3.25}$$

is stable. The remaining linear error dynamics (3.25) in sliding mode corresponds to the error dynamics of a *reduced Luenberger observer*, see [Utk92].

### Implementation issues

The sliding mode design method involves continuous-time models and presumes infinite switching frequency. The implementation of the observer (3.21) in a computer will generate chattering because of the finite switching frequency. An efficient strategy is to introduce a *boundary layer* of width  $\varepsilon_o$  by replacing the sign functions in (3.21) with saturation functions as shown in Fig. 3.1, see [SL91], i.e.

$$\text{sat}\left(\frac{\sigma_i}{\varepsilon_{o,i}}\right) = \begin{cases} \mathbf{sgn}(\sigma_i) & \text{for } |\sigma_i| > \varepsilon_{o,i} \\ \sigma_i/\varepsilon_{o,i} & \text{for } |\sigma_i| \leq \varepsilon_{o,i} \end{cases}, \quad i = 1 \dots, r, \tag{3.26}$$

where  $\varepsilon_{o,i}$  denotes the boundary layer width of the  $i$ -th sliding surface  $\sigma_i$ . Due to the implementation of the boundary layer sliding mode cannot exist, since the right hand side of (3.26) is continuous.

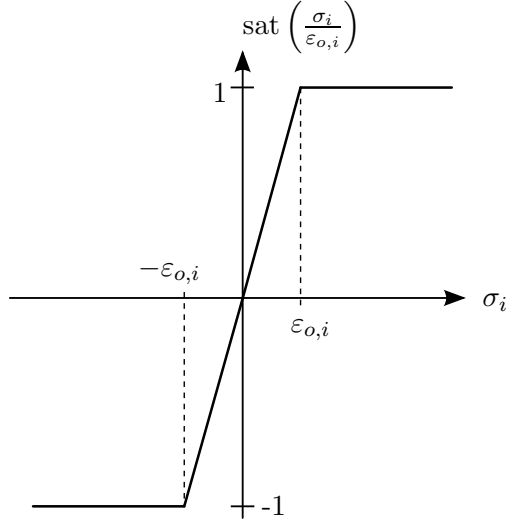


Figure 3.1: Representation of a boundary layer with a saturation function for chattering reduction.

### Design with nonlinear synthesis model

The sliding mode observer can also be designed based on the nonlinear power-train model according to (2.39). This is performed in section B.3. The observer (B.42) has a major disadvantage compared to the observer design based on a linear synthesis model. The backlash width  $2\alpha$  must be known. This means that an additional estimation algorithm is necessary for the backlash width, see for example [LE07, MDCF06]. Due to the large stiffness estimation errors of the backlash width will lead to large errors of the estimated torque.

### 3.2.2 Extension for delayed and sampled measurements

In this section the observer of section 3.2.1 will be extended for the case that a part of the sensor signals is available only via a network or bus system. Assume that  $(r - l) > 0$  output signals  $\mathbf{y}_1(t) = \bar{\mathbf{C}}_1 \bar{\mathbf{x}}(t)$  can be measured without any delay and  $l$  output signals of (3.16) can only be measured with delay  $\tau_0$  which is assumed to be constant. Due to the transmission over the network or bus system the outputs are available only at the time instants  $t_k$ ,  $k \in \mathbb{N}_0$ , such that they remain constant for the time  $t_k \leq t < t_{k+1}$  as shown in Fig. 3.2. The delayed and sampled outputs can be represented as signals with *time-varying* delay  $\tau(t)$ , i.e.

$$\mathbf{y}_2(t_k - \tau_0) = \bar{\mathbf{C}}_2 \bar{\mathbf{x}}(t - \tau(t)), \quad (3.27)$$

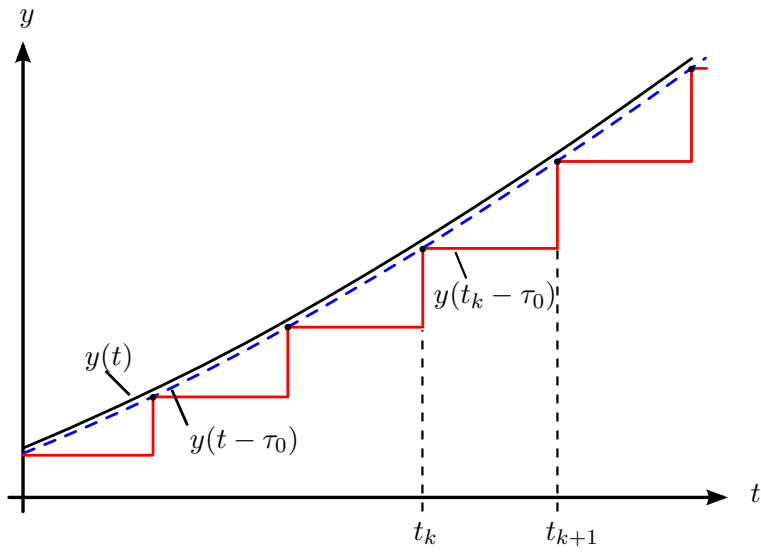


Figure 3.2: Delayed and sampled signal due to network or bus transmission.

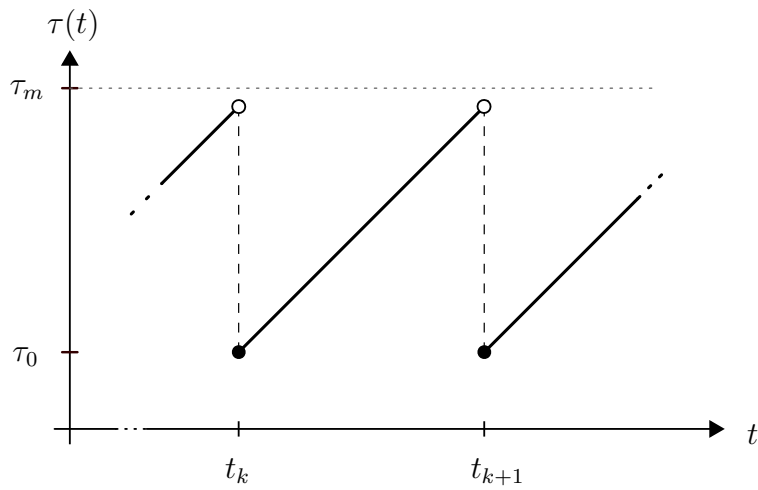


Figure 3.3: Variable time delay  $\tau(t)$  due to sampling. Additional constant delay  $\tau_0$  due to measurement processing and bus transmission. The overall delay is assumed to be bounded by  $\tau_m$ .

where  $t_{k+1} - t_k \leq \tau_s$  is upper bounded and  $\bar{\mathbf{C}}_2 \in \mathbb{R}^{l \times \bar{n}}$ . Due to sampling

$$\tau(t) = t - t_k + \tau_0 \quad (3.28)$$

has the form of a sawtooth function where  $\dot{\tau}(t) = 1$  for  $t \neq t_k$ , see Fig. 3.3.

**Remark:** For the wheel speed sensor and bus model in sections 2.5.2 and 2.5.3 the delay  $\tau_0$  can be represented as  $\tau_0 = \Delta t + \tau_{gr} + \tau_b$ .

### Observer design

It is assumed that the pair  $(\bar{\mathbf{C}}_1, \bar{\mathbf{A}})$  in (3.16) is observable and that the output matrix can be represented as

$$\bar{\mathbf{C}} = \begin{bmatrix} \bar{\mathbf{C}}_2 \\ \bar{\mathbf{C}}_1 \end{bmatrix}, \quad (3.29)$$

such that the rows of  $\bar{\mathbf{C}}_1$  and  $\bar{\mathbf{C}}_2$  span different sub-spaces. Applying the linear state transformation (3.19) the output matrix (3.29) is of the form

$$\bar{\mathbf{C}}\mathbf{T}^{-1} = \begin{bmatrix} \mathbf{0} & \mathbf{C}'_2 & \mathbf{0} \\ \mathbf{0} & \mathbf{0} & \mathbf{C}'_1 \end{bmatrix},$$

where  $\mathbf{C}'_1 \in \mathbb{R}^{(r-l) \times (r-l)}$  and  $\mathbf{C}'_2 \in \mathbb{R}^{l \times l}$ . The transformed system (3.16) can be represented as

$$\begin{aligned} \dot{\mathbf{z}} &= \mathbf{A}_{11}\mathbf{z} + \mathbf{A}_{12}\mathbf{y}_1 + \mathbf{b}_1\mathbf{u}, \\ \dot{\mathbf{y}}_1 &= \mathbf{A}_{21}\mathbf{z} + \mathbf{A}_{22}\mathbf{y}_1 + \mathbf{b}_2\mathbf{u}. \end{aligned} \quad (3.30)$$

The vector  $\mathbf{y}_1$  contains the state variables which can be measured without delay. The vector  $\mathbf{z} \in \mathbb{R}^{(\bar{n}-r+l) \times 1}$  contains the state variables to be estimated  $\mathbf{x}_1 \in \mathbb{R}^{(\bar{n}-r) \times 1}$  and the state variables which can be measured only with delay  $\mathbf{y}_2$ , i.e.

$$\mathbf{z} = \begin{bmatrix} \mathbf{x}_1 \\ \mathbf{y}_2 \end{bmatrix}. \quad (3.31)$$

Then, observer (3.21) for the system (3.30) is extended by an additional time-delay term as follows:

#### Sliding mode observer with additional delayed linear error feedback

$$\begin{aligned} \dot{\hat{\mathbf{z}}} &= \mathbf{A}_{11}\hat{\mathbf{z}} + \mathbf{A}_{12}\hat{\mathbf{y}}_1 + \mathbf{b}_1u + \mathbf{L}_1\mathbf{v} + \mathbf{L}_2\mathbf{e}_{y_2}(t_k - \tau_0), \\ \dot{\hat{\mathbf{y}}}_1 &= \mathbf{A}_{21}\hat{\mathbf{z}} + \mathbf{A}_{22}\hat{\mathbf{y}}_1 + \mathbf{b}_2u - \mathbf{v}, \\ \mathbf{v} &= \mathbf{M} \operatorname{sgn}(\hat{\mathbf{y}}_1 - \mathbf{y}_1), \\ \mathbf{M} &= \operatorname{diag}(M_i), \quad i = 1, \dots, r-l. \end{aligned} \quad (3.32)$$

The dimensions of the observer gain matrices are  $\mathbf{L}_1 \in \mathbb{R}^{(\bar{n}-r+l) \times (r-l)}$ ,  $\mathbf{L}_2 \in \mathbb{R}^{(\bar{n}-r+l) \times l}$ ,  $\mathbf{M} \in \mathbb{R}^{(r-l) \times (r-l)}$ .

The error of the delayed measurements is defined by

$$\mathbf{e}_{y_2}(t_k - \tau_0) = \hat{\mathbf{y}}_2(t_k - \tau_0) - \mathbf{y}_2(t_k - \tau_0) = \mathbf{C}_2 \mathbf{e}_z(t_k - \tau_0), \quad (3.33)$$

where  $t_k \leq t < t_{k+1}$ ,

$$\mathbf{C}_2 = [\mathbf{0} \ \mathbf{C}'_2] \in \mathbb{R}^{l \times (\bar{n}-r+l)}, \quad (3.34)$$

and

$$\mathbf{e}_z = \hat{\mathbf{z}} - \mathbf{z}. \quad (3.35)$$

### Stability determination

For  $M_i$ ,  $i = 1, \dots, r-l$  sufficiently large sliding mode exists and the dynamics of the estimation error  $\mathbf{e}_z$  is

$$\dot{\mathbf{e}}_z = \mathbf{A}_0 \mathbf{e}_z + \mathbf{A}_1 \mathbf{e}_z(t - \tau(t)), \quad (3.36)$$

where  $\mathbf{A}_0 = \mathbf{A}_{11} + \mathbf{L}_1 \mathbf{A}_{21}$  and  $\mathbf{A}_1 = \mathbf{L}_2 \mathbf{C}_2$ . The initial condition of (3.36) is

$$\begin{aligned} \mathbf{e}_z(\psi) &= \mathbf{0}, \quad \text{for } \psi \in [-\tau_m, 0), \\ \mathbf{e}_z(0) &= \mathbf{e}_0, \end{aligned} \quad (3.37)$$

where  $\tau_m = \tau_s + \tau_0$  denotes the maximum time delay and  $\mathbf{e}_0$  the initial estimation error.

The stability of the error dynamics (3.36) has to be determined in a two-step procedure. First the observer gain  $\mathbf{L}_1$  has to be chosen such that  $\mathbf{A}_0$  is stable. The error dynamics (3.36) has to be stable also in the delay free case, i.e.  $\mathbf{A}_0 + \mathbf{A}_1$  must be Hurwitz. The gain  $\mathbf{L}_2$  can be chosen e.g. by pole placement such that  $\mathbf{A}_0 + \mathbf{A}_1$  is stable. The stability of (3.36) can be determined with e.g. the Razumikhin theorem, see [GKC03], but leads to conservative results. Therefore the stability will be determined with the help of the following theorem, see [LF12, Fri14], which yields less conservative results:

**Theorem:** For  $\tau_0$ , and  $\tau_s$  given, if the positive definite  $(\bar{n} - r + l) \times (\bar{n} - r + l)$ -matrices  $\mathbf{P}$ ,  $\mathbf{W}$ ,  $\mathbf{R}_1$ ,  $\mathbf{R}_2 \succ 0$  exist, system (3.36) is asymptotically stable, if

$$\begin{bmatrix} \mathbf{U} & \mathbf{P}\mathbf{A}_1 + \mathbf{R}_2 & \mathbf{P}\mathbf{A}_1 & \mathbf{A}_0^T \mathbf{F} \\ \mathbf{A}_1^T \mathbf{P} + \mathbf{R}_2 & -\mathbf{R}_1 - \mathbf{R}_2 & \mathbf{0} & \mathbf{A}_1^T \mathbf{F} \\ \mathbf{A}_1^T \mathbf{P} & \mathbf{0} & -\frac{\pi^2}{4} \mathbf{W} & \mathbf{A}_1^T \mathbf{F} \\ \mathbf{F}\mathbf{A}_0 & \mathbf{F}\mathbf{A}_1 & \mathbf{F}\mathbf{A}_1 & -\mathbf{F} \end{bmatrix} \prec 0, \quad (3.38)$$

where

$$\begin{aligned} \mathbf{U} &= \mathbf{A}_0^T \mathbf{P} + \mathbf{P}\mathbf{A}_0 + \mathbf{R}_1 - \mathbf{R}_2, \\ \mathbf{F} &= \tau_s^2 \mathbf{W} + \tau_0^2 \mathbf{R}_2. \end{aligned}$$

Theorem (3.38) denotes a *Linear Matrix Inequality* (LMI) and results from the derivative of a *Lyapunov-Krasovskii functional*, see appendix A.

Also exponential stability with decay rate  $\gamma > 0$  can be guaranteed [LF12]. With the change of variables  $\bar{\mathbf{e}}_z(t) = e^{\gamma t} \mathbf{e}_z(t)$  the error dynamics of (3.36) can be represented as

$$\dot{\bar{\mathbf{e}}}_z = (\mathbf{A}_0 + \gamma \mathbf{I}) \bar{\mathbf{e}}_z + e^{\gamma \tau(t)} \mathbf{A}_1 \bar{\mathbf{e}}_z(t - \tau(t)). \quad (3.39)$$

The stability of (3.39) guarantees the exponential stability of (3.36) with decay rate  $\gamma > 0$ . Since (3.38) is affine in  $\mathbf{A}_0$  and  $\mathbf{A}_1$  and by convexity arguments, condition (3.38) has to be verified for

$$\bar{\mathbf{A}}_0 = \mathbf{A}_0 + \gamma \mathbf{I}, \quad \bar{\mathbf{A}}_1^{(1)} = e^{\gamma \tau_0} \mathbf{A}_1, \quad (3.40)$$

and

$$\bar{\mathbf{A}}_0 = \mathbf{A}_0 + \gamma \mathbf{I}, \quad \bar{\mathbf{A}}_1^{(2)} = e^{\gamma \tau_m} \mathbf{A}_1, \quad (3.41)$$

by solving the two corresponding LMIs simultaneously.

### Implementation issues

Again a boundary layer can be used in (3.32) to reduce chattering. Within the boundary layer the observer gains are

$$\bar{\mathbf{L}}_1 = \frac{1}{\varepsilon_o} \begin{bmatrix} \mathbf{L}_1 \mathbf{M} \\ -\mathbf{M} \end{bmatrix}, \quad \bar{\mathbf{L}}_2 = \begin{bmatrix} \mathbf{L}_2 \\ \mathbf{0} \end{bmatrix}. \quad (3.42)$$

### 3.2.3 Observer design for a power-train with backlash

In this section the observer concepts of sections 3.2.1 and 3.2.3 are used for estimating the shaft and load torque in the power-train. The model for the observer design is the synthesis model (2.42). The *unknown* disturbance  $w = T_l$  is modeled as

$$w = k_s q, \quad \dot{q} = 0, \quad (3.43)$$

where the scaling factor  $k_s$  corresponds to the shaft stiffness. The scaling factor has been introduced for convenience such that the observer stability analysis is simplified in section B.1. As proposed in section 3.2.1 the state variable corresponding to the disturbance is placed at first in the augmented state vector. Since the state of the synthesis model is already in the appropriate form the state  $\hat{\mathbf{x}}$  does not have to be reordered by the linear state transformation (3.19).

### Measurements without delay

In this section it is assumed that the motor and load angular speeds can be measured without delay. The proposed observer concept is based on the works presented in [AH11] and [AH10]. The states according to (3.20) are

$$\mathbf{x}_1 = [q \quad \varphi]^T \quad \text{and} \quad \mathbf{y} = [\omega_l \quad \omega_m].$$

The submatrices according (3.20) are  $\mathbf{A}_{11} = \mathbf{0}$ ,  $\mathbf{b}_1 = \mathbf{0}$  and

$$\mathbf{A}_{12} = \begin{bmatrix} 0 & 0 \\ -1 & \frac{1}{k_g} \end{bmatrix}, \quad \mathbf{A}_{21} = \begin{bmatrix} -\frac{k_s}{J_l} & \frac{k_s}{J_l} \\ 0 & -\frac{k_s}{k_g J_m} \end{bmatrix},$$

$$\mathbf{A}_{22} = \begin{bmatrix} -\frac{d_l}{J_l} & 0 \\ 0 & -\frac{d_m}{J_m} \end{bmatrix}, \quad \mathbf{b}_2 = \begin{bmatrix} 0 \\ \frac{1}{J_m} \end{bmatrix}.$$

For sufficiently large elements  $M_i$ ,  $i = 1, 2$  of the matrix  $\mathbf{M}$  observer (3.21) with the following gain matrix  $\mathbf{L}$  renders the error dynamics (3.25) exponentially stable:

Observer gain matrix

$$\mathbf{L} = \begin{bmatrix} \frac{J_l}{k_s} \lambda_1 & \frac{k_g J_m}{k_s} \lambda_1 \\ 0 & \frac{k_g J_m}{k_s} \lambda_2 \end{bmatrix}, \quad \lambda_1 > 0, \lambda_2 > 0 \quad (3.44)$$

The observer gain matrix  $\mathbf{L}$  can be determined by hand. The error dynamics is given by

$$\dot{\mathbf{e}}_{x_1} = \text{diag}(-\lambda_1, -\lambda_2) \mathbf{e}_{x_1}. \quad (3.45)$$

In section B.1.1 the observer error dynamics is analyzed for the contact and backlash phase for the power-train model with backlash (2.39). In the contact phase the observer error dynamics does not change and the estimated sates are calculated correctly if *unknown* backlash is present in the power train. During the backlash phase the shaft torque estimate remains bounded and the error dynamics of the load torque estimate remains stable.

According to (2.33) the load inertia  $J_l$  might change e.g. due to longitudinal slip or a changing vehicle load. Since the load torque which is estimated influences the second differential equation in (2.29) a change of the load inertia will change the load torque estimate. The analysis of the parameter  $J_l$  is given in section B.2.1.

### Delayed and sampled load speed measurement

According to (3.30) the state vector consists of

$$\mathbf{z} = [q \quad \varphi \quad \omega_l]^T \quad \text{and} \quad y_1 = \omega_m \quad (3.46)$$

The sub-matrices according to (3.30) are  $\mathbf{b}_1 = \mathbf{0}$ ,  $b_2 = 1/J_m$  and

$$\mathbf{A}_{11} = \begin{bmatrix} 0 & 0 & 0 \\ 0 & 0 & -1 \\ -\frac{k_s}{J_l} & \frac{k_s}{J_l} & -\frac{d_l}{J_l} \end{bmatrix}, \quad \mathbf{a}_{12} = \begin{bmatrix} 0 \\ \frac{1}{k_g} \\ 0 \end{bmatrix},$$

$$\mathbf{a}_{21}^T = \begin{bmatrix} 0 & -\frac{k_s}{k_g J_m} & 0 \end{bmatrix}, \quad a_{22} = -d_m/J_m.$$

The determination of the gains  $\mathbf{I}_1$  and  $\mathbf{I}_2$  of the observer from section 3.2.2 are determined in a two step process.

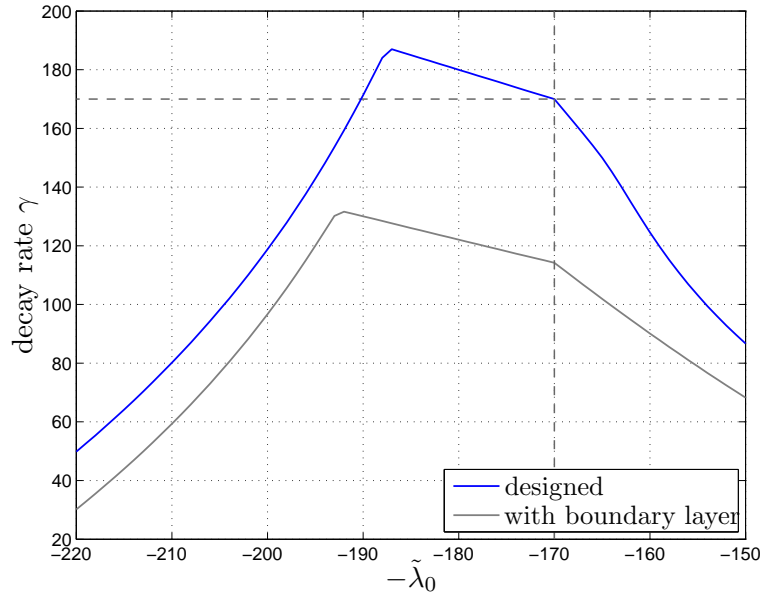


Figure 3.4: Exponential decay rate  $\gamma$  of the observer error dynamics in dependence of the real part  $-\tilde{\lambda}_0$  of the eigenvalues of  $\mathbf{A}_0 + \mathbf{A}_1$ .

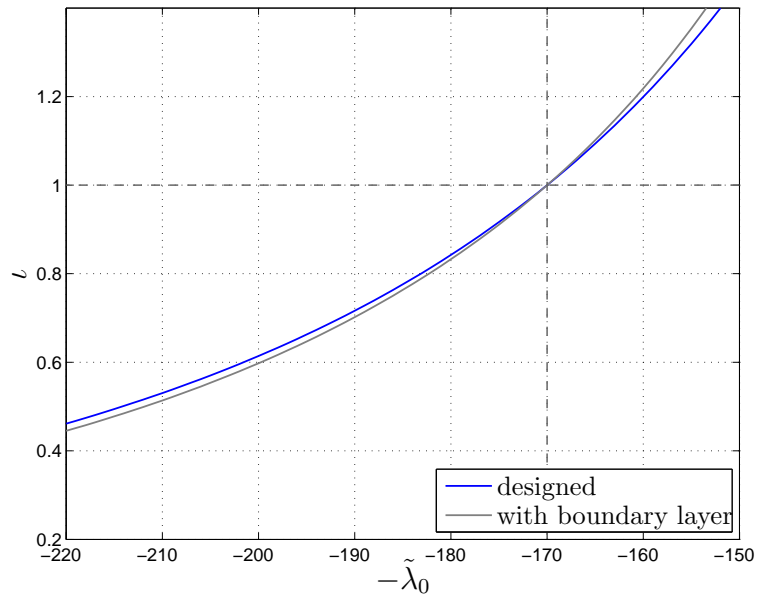


Figure 3.5: Value  $\iota$  which is a measure for the estimation error of the load angular velocity signal in the backlash phase in dependence of the real part  $-\tilde{\lambda}_0$  of the eigenvalues of  $\mathbf{A}_0 + \mathbf{A}_1$ .

In the first step the gain  $\mathbf{I}_1$  has to be chosen such that  $\mathbf{A}_0$  is stable. The eigenvalues  $s_i$  of  $\mathbf{A}_0$  are determined by pole placement such that their real parts are identical, i.e.

$$\operatorname{Re}(s_i) = -\lambda_0, \quad \lambda_0 > 0, i = 1, \dots, 3. \quad (3.47)$$

In the second step the gain  $\mathbf{I}_2$  has to be determined with an iterative process by pole placement such that  $(\mathbf{A}_0 + \mathbf{A}_1)$  has desired eigenvalues. It is desirable that the decay rate  $\gamma$  of the error dynamics (3.25) will not deteriorate due to the delayed and sampled measurement signal  $\omega_l$ . Therefore the real part  $\tilde{\lambda}_0$  of the eigenvalues of  $(\mathbf{A}_0 + \mathbf{A}_1)$  has to be chosen such that  $\tilde{\lambda}_0 > \lambda_0$ .

For each value of  $\tilde{\lambda}_0$  the decay rate  $\gamma$  has to be determined. This involves also an iterative search by a bisection method for  $\gamma$  by solving the LMIs (3.38) for the matrices (3.40) and (3.41) simultaneously. The initial interval of the bisection search for  $\gamma$  is chosen as  $[0, \tilde{\lambda}_0]$ . The bisection search is stopped after a predefined number of steps. Fig. 3.4 shows the exponential decay rate  $\gamma$  of the error dynamics (3.36) in dependence of the real part  $-\tilde{\lambda}_0$  of the eigenvalues of  $(\mathbf{A}_0 + \mathbf{A}_1)$ . This design was done with the parameters of the test bench. The real parts of the eigenvalues of  $\mathbf{A}_0$  were chosen as  $-\lambda_0 = -170$ . The choice of the eigenvalues of  $(\mathbf{A}_0 + \mathbf{A}_1)$  and the observer parameters is described in chapter 5.

In section B.1.2 the observer error dynamics is analyzed for the contact and backlash phase with the power-train model with backlash (2.39). In the contact phase the observer error dynamics does not change and the estimated states are calculated correctly if *unknown* backlash is present in the power train. Contrary to the observer without delayed measurement the state corresponding to the *disturbance* estimate is not observable due to the delayed load speed measurement. Therefore the load torque should be small during the backlash phases. This can be achieved by considering the acceleration force of the vehicle in load inertia as described in section 2.4.1.

In section B.1.2 also the steady state error in the backlash phase is analyzed. According to (B.24) the value  $\iota$  is a measure for the steady state error of the load speed estimate in the backlash phase, i.e.

Steady state error measure of the load speed estimate in the backlash phase

$$\iota = -\mathbf{h}_3^T (\mathbf{A}_0 + \mathbf{A}_1)^{-1} \mathbf{h}_2. \quad (3.48)$$

The vectors  $\mathbf{h}_3$  and  $\mathbf{h}_2$  denote the corresponding unit vectors. Fig. 3.5 depicts (3.48) in dependence of the the real part  $-\tilde{\lambda}$  of the eigenvalues of  $(\mathbf{A}_0 + \mathbf{A}_1)$ .

### 3.3 Second-order sliding mode observer

The disadvantage of first-order sliding modes is chattering. With the help of a saturation function the chattering was significantly reduced. As a result the robustness properties are lost. Therefore in this section a second-order sliding mode unknown input observer concept will be used for estimating the torsion angle of the shaft.

#### 3.3.1 Step-by-step observer

Consider the linear, time-invariant, observable system with *unknown* input (3.15). The vector of measured signals  $\mathbf{y} \in \mathbb{R}^r$  can be expressed as

$$\mathbf{y} = \mathbf{C}\mathbf{x} = \begin{bmatrix} \mathbf{c}_1^T \\ \vdots \\ \mathbf{c}_r^T \end{bmatrix} \mathbf{x}. \quad (3.49)$$

Define the relative degree  $\delta_{i,w}$ ,  $i = 1, \dots, r$  of the  $i$ -th output  $y_i$  with respect to the disturbance input  $w$  as the smallest integer such that

$$\mathbf{c}_i^T \mathbf{A}^j \mathbf{m} = 0, \quad j = 1, \dots, \delta_{i,w} - 2, \quad \text{and} \quad \mathbf{c}_i^T \mathbf{A}^{\delta_{i,w}-1} \mathbf{m} \neq 0. \quad (3.50)$$

It is assumed that the sum of the relative degrees corresponds to  $n$ . This means that the system (3.15) is *strongly observable* and the transformation matrix

$$\mathbf{T} = \begin{bmatrix} \mathbf{c}_1^T \\ \vdots \\ \mathbf{c}_1^T \mathbf{A}^{\rho_1} \\ \vdots \\ \mathbf{c}_r^T \\ \vdots \\ \mathbf{c}_r^T \mathbf{A}^{\rho_r} \end{bmatrix} \quad (3.51)$$

has full rank. With  $\mathbf{z} = \mathbf{T}\mathbf{x}$  the system (3.15) can be transformed into a *block triangular form*, see [FB06]. Separating the transformed state vector  $\mathbf{z}$  into  $r$  subvectors, i.e.

$$\mathbf{z} = \begin{bmatrix} \mathbf{z}_1 \\ \vdots \\ \mathbf{z}_r \end{bmatrix}, \quad \mathbf{z}_i \in \mathbb{R}^{\rho_i}, \quad (3.52)$$

the  $i$ -th block of the transformed system has the form

$$\begin{aligned} \dot{\mathbf{z}}_i &= \tilde{\mathbf{H}}_i \mathbf{z}_i + \tilde{\mathbf{A}}_i \mathbf{z} + \tilde{\mathbf{b}}_i u + \tilde{\mathbf{d}}_i w, \\ y_i &= [1 \ 0 \ \dots \ 0] \mathbf{z}_i, \end{aligned} \quad (3.53)$$

where  $\tilde{\mathbf{H}}_i \in \mathbb{R}^{\rho_i \times \rho_i}$ ,  $\tilde{\mathbf{A}}_i \in \mathbb{R}^{\rho_i \times n}$ ,  $\tilde{\mathbf{b}}_i$ ,  $\tilde{\mathbf{d}}_i$ ,  $\tilde{\mathbf{z}}_i \in \mathbb{R}^{\rho_i}$  and

$$\tilde{\mathbf{H}}_i = \begin{bmatrix} 0 & 1 & 0 & \dots & 0 \\ \vdots & \ddots & \ddots & \ddots & \vdots \\ \vdots & & \ddots & 1 & 0 \\ 0 & \dots & \dots & 0 & 0 \end{bmatrix}, \quad \tilde{\mathbf{A}}_i = \begin{bmatrix} \mathbf{0}^T \\ \vdots \\ \mathbf{0}^T \\ \mathbf{c}_i^T \mathbf{A}^{\rho_i} \mathbf{T}^{-1} \end{bmatrix}, \quad \tilde{\mathbf{d}}_i = \begin{bmatrix} 0 \\ \vdots \\ 0 \\ \mathbf{c}_i^T \mathbf{A}^{\rho_i-1} \mathbf{m} \end{bmatrix}.$$

According to [FB06] the step-by-step observer for the  $i$ -th block is given by

$$\begin{aligned} \dot{\hat{z}}_{i,1} &= \nu(\hat{z}_{i,1} - y_i) + \tilde{b}_{i,1}u, \\ \dot{\hat{z}}_{i,2} &= E_{i,1}\nu(\hat{z}_{i,2} - \tilde{z}_{i,2}) + \tilde{b}_{i,2}u, \\ &\vdots \\ \dot{\hat{z}}_{i,\rho_i} &= \mathbf{c}_i^T \mathbf{A}^{\rho_i} \mathbf{T}^{-1} \hat{\mathbf{z}} + E_{i,\rho_i-1}\nu(\hat{z}_{i,\rho_i} - \tilde{z}_{i,\rho_i}) + \tilde{b}_{i,\rho_i}u, \end{aligned} \tag{3.54}$$

where  $\tilde{b}_{i,j}$ ,  $j = 1, \dots, \rho_i$  denote the elements of  $\tilde{\mathbf{b}}_i$ . The elements of  $\tilde{z}_{i,j}$  are defined recursively, i.e.

$$\begin{aligned} \tilde{z}_{i,1} &= y_i, \\ \tilde{z}_{i,j} &= \nu(\hat{z}_{i,j-1} - \tilde{z}_{i,j-1}), \quad j = 2, \dots, \rho_i. \end{aligned} \tag{3.55}$$

The nonlinear injection terms are composed of the super-twisting algorithm [Lev93, Lev98]

$$\begin{aligned} \nu(\sigma_{i,j}) &= -\kappa_{1,i,j} \sqrt{|\sigma_{i,j}|} \operatorname{sgn}(\sigma_{i,j}) + v_{i,j}, \\ \dot{v}_{i,j} &= -\kappa_{2,i,j} \operatorname{sgn}(\sigma_{i,j}), \end{aligned} \tag{3.56}$$

where  $\kappa_{1,i,j} > 0$ ,  $\kappa_{2,i,j} > 0$ ,  $j = 1, \dots, \rho_i$ . The factors  $E_{i,j}$ ,  $j = 1, \dots, \rho_i - 1$  will be set to one if all the previous errors have vanished which represents an *anti-peaking structure*. The observer design involves in total  $2n$  states. The estimation errors are defined as

$$e_{i,j} = \hat{z}_{i,j} - z_{i,j}, \quad j = 1, \dots, \rho_i. \tag{3.57}$$

The dynamics of the first error differential equation of the  $i$ -th block is given by

$$\dot{e}_{i,1} = \nu(e_{i,1}) - z_{i,2}. \tag{3.58}$$

Assuming that  $z_{i,2}$  obeys a *Lipschitz condition* with *Lipschitz constant*<sup>2</sup>  $L_{i,2}$ , i.e.  $|\dot{z}_{i,2}| \leq L_{i,2}$  and for sufficiently large  $\kappa_{1,i,1}$ ,  $\kappa_{2,i,1}$  after finite time a second-order sliding mode occurs in (3.58), i.e.  $\{e_{i,1} = 0, \dot{e}_{i,1} = 0\}$ , such that

$$\nu(e_{i,1}) = z_{i,2}. \tag{3.59}$$

---

<sup>2</sup> $|z(t_1) - z(t_0)| \leq L|t_1 - t_0|$  for all  $t_0, t_1 \in \mathbb{R}$ .

With  $\hat{z}_{i,1} = z_{i,2}$  the error dynamics (3.58) implements a *robust exact* differentiator, see [Lev98]. Then the second observer equation in the  $i$ -th block will be enabled by setting  $E_{i,1}$  to one. With (3.55) and (3.59) it follows that

$$\begin{aligned}\dot{e}_{i,2} &= \nu(\hat{z}_{i,2} - \tilde{z}_{i,2}) - z_{i,3}, \\ &= \nu(\hat{z}_{i,2} - \nu(e_{i,1})) - z_{i,3}, \\ &= \nu(\hat{z}_{i,2} - z_{i,2}) - z_{i,3}, \\ &= \nu(e_{i,2}) - z_{i,3}.\end{aligned}\tag{3.60}$$

For  $|\dot{z}_{i,3}| \leq L_{i,3}$  and sufficiently large  $\kappa_{1,i,2}$ ,  $\kappa_{2,i,2}$  after finite time a second-order sliding mode occurs in (3.60), i.e.  $\{e_{i,2} = 0, \dot{e}_{i,2} = 0\}$ , such that

$$\nu(e_{i,2}) = z_{i,3}.\tag{3.61}$$

This process is continued such that the estimates of the corresponding states converge step-by-step. In the last step  $E_{i,\rho_i-1}$  will be set to one such that

$$\dot{e}_{i,\rho_i} = \nu(\hat{z}_{i,\rho_i} - \tilde{z}_{i,\rho_i}) + \mathbf{c}_i^T \mathbf{A}^{\rho_i} \mathbf{T}^{-1} \mathbf{e} - \mathbf{c}_i^T \mathbf{A}^{\rho_i-1} \mathbf{m} w,\tag{3.62}$$

where  $\mathbf{e} = \hat{\mathbf{z}} - \mathbf{z}$ . It is assumed that a Lipschitz constant exists such that  $|\mathbf{c}_i^T \mathbf{A}^{\rho_i-1} \mathbf{m}| \cdot |w| \leq L_{i,\rho_i+1}$ . Sufficient conditions for the stability of the super-twisting algorithm, see [SEFL13], are

$$\begin{aligned}\kappa_{2,i,j} &> 1.1 L_{i,j+1}, \\ \kappa_{1,i,j} &\geq 1.5 \sqrt{L_{i,j+1}}, \quad j = 1, \dots, \rho_i, \quad i = 1, \dots, r.\end{aligned}\tag{3.63}$$

### 3.3.2 Observer design for a power-train with backlash

For the application of the observer from section 3.3.1 the number of steps should be small as it will be the case for the power-train synthesis model (2.42). The damping constant  $d_s > 0$  is incorporated in the synthesis model since it reduces the relative degrees with respect to the *unknown* input by one. For the outputs  $y_1 = \mathbf{c}_1^T \mathbf{x} = \omega_l$  and  $y_2 = \mathbf{c}_2^T \mathbf{x} = \omega_m$  the relative degrees with respect to the *unknown* input  $w$  are

$$\delta_{1,w} = 1, \quad \delta_{2,w} = 2.\tag{3.64}$$

The sum of the relative degrees in (3.64) corresponds to the system order  $n = 3$  such that the *strong observability condition* is fulfilled with respect to the *unknown* input  $w$ . The transformation matrix  $\mathbf{T}$  is

$$\mathbf{T} = \begin{bmatrix} \mathbf{c}_1^T \\ \mathbf{c}_2^T \\ \mathbf{c}_2^T \mathbf{A} \end{bmatrix},\tag{3.65}$$

such that  $\rho_1 = 1$  and  $\rho_2 = 2$ . With the regular state transformation  $\mathbf{z} = \mathbf{T}\mathbf{x}$  the system in *block observable form* is given by

$$\tilde{\mathbf{A}} = \begin{bmatrix} -\frac{d_l}{J_l} & -\frac{d_m}{J_l} & -\frac{J_m k_g}{J_l} \\ 0 & 0 & 1 \\ \frac{J_l k_s - d_l d_s}{J_l J_m} & -\frac{J_l k_s + d_m d_s}{J_l J_m} & -\frac{d_s J_m + J_l (d_s + d_m)}{J_l J_m} \end{bmatrix},\tag{3.66}$$

where the gear transmission ratio  $k_g = 1$  was assumed for simplicity. The transformed vectors  $\tilde{\mathbf{d}}$  and  $\tilde{\mathbf{b}}$  are given by

$$\tilde{\mathbf{d}} = \begin{bmatrix} -\frac{1}{J_l} \\ 0 \\ -\frac{d_s}{J_l J_m} \end{bmatrix}, \quad \tilde{\mathbf{b}} = \begin{bmatrix} 0 \\ \frac{1}{J_m} \\ -\frac{d_s + d_m}{J_m^2} \end{bmatrix}. \quad (3.67)$$

The elements of the vectors  $\tilde{\mathbf{b}}$ ,  $\tilde{\mathbf{d}}$  and  $\mathbf{z}$  will be numbered in ascending order for convenience. Then

$$\begin{aligned} z_1 &= y_1, \\ z_2 &= y_2, \\ z_3 &= \dot{z}_2 - \tilde{b}_2 u. \end{aligned} \quad (3.68)$$

Denoting the elements of the transformed matrix  $\tilde{\mathbf{A}}$  with  $\tilde{a}_{ij}$ ,  $i, j = 1, \dots, 3$ , the transformed system (3.15) corresponds to

$$\begin{aligned} \dot{z}_1 &= \tilde{a}_{11} z_1 + \tilde{a}_{12} z_2 + \tilde{a}_{13} z_3 + \tilde{d}_1 w, \\ \dot{z}_2 &= z_3 + \tilde{b}_2 u, \\ \dot{z}_3 &= \tilde{a}_{31} z_1 + \tilde{a}_{32} z_2 + \tilde{a}_{33} z_3 + \tilde{b}_3 u + \tilde{d}_3 w. \end{aligned} \quad (3.69)$$

The observer for the transformed system (3.69) is given as follows:

#### Step-by-step observer

$$\begin{aligned} \dot{\hat{z}}_1 &= \tilde{a}_{11} z_1 + \tilde{a}_{12} z_2 + \tilde{a}_{13} \hat{z}_3 + \nu (\hat{z}_1 - y_1), \\ \dot{\hat{z}}_2 &= \nu (\hat{z}_2 - y_2) + \tilde{b}_2 u, \\ \dot{\hat{z}}_3 &= \tilde{a}_{31} z_1 + \tilde{a}_{32} z_2 + \tilde{a}_{33} \hat{z}_3 + E_3 \nu (\hat{z}_3 - \tilde{z}_3) + \tilde{b}_3 u. \end{aligned} \quad (3.70)$$

The term  $\tilde{z}_3$  denotes the result of the super-twisting algorithm of the previous step, i.e.  $\tilde{z}_3 = \nu(\hat{z}_2 - y_2)$ . The first and third observer equation reproduce the system equations in order to reduce the gains in the super-twisting algorithms. Fig. 3.6 shows the structure of the observer.

#### Determination of the observer gains

The estimation errors are defined as

$$e_i = \hat{z}_i - z_i, \quad i = 1, \dots, 3. \quad (3.71)$$

The observer error dynamics corresponds to

$$\begin{aligned} \dot{e}_1 &= \nu(e_1) + \tilde{a}_{13} e_3 - \tilde{d}_1 w, \\ \dot{e}_2 &= \nu(e_2) - z_3, \\ \dot{e}_3 &= E_3 \nu(\tilde{z}_3 - \hat{z}_3) + \tilde{a}_{33} e_3 - \tilde{d}_3 w. \end{aligned} \quad (3.72)$$

For sufficiently large observer gains a second-order sliding mode will occur after finite time such that  $\{e_i = 0, \dot{e}_i = 0\}$ ,  $i = 1, \dots, 2$ . Then

$$\nu(e_2) = z_3, \text{ and } e_3 = \tilde{z}_3 - \hat{z}_3 \quad (3.73)$$

Since  $\tilde{a}_{33} < 0$  the error  $e_3$  is bounded for  $E_3 = 0$ . Then, by setting  $E_3 = 1$ , after finite time a second-order sliding mode occurs also in the third error differential equation, i.e.  $\{e_3 = 0, \dot{e}_3 = 0\}$ .

For the determination of the observer gains the Lipschitz constants have to be estimated with the help of the observer error dynamics (3.72). According to the second error differential equation in (3.72) the Lipschitz constant has to be chosen such that

$$|\dot{z}_3|_{\max} \leq L_2. \quad (3.74)$$

According to (3.68)  $|\dot{z}_3| = |\ddot{w}_m - \tilde{b}_2 \dot{u}|$ . In the first and third differential equation of (3.72) the maximum derivative of the disturbance  $|w|$  has to be considered, i.e.

$$|\tilde{d}_1| |\dot{w}|_{\max} \leq L_1, \quad (3.75)$$

and

$$|\tilde{d}_3| |\dot{w}|_{\max} \leq L_3. \quad (3.76)$$

The maximum values of the derivatives can be evaluated with the simulation model (2.48) or from measurements. Then the observer gains can be calculated with the help of (3.63).

### Reconstruction of the unknown input

Presuming sliding mode the *unknown* input  $w$  can be reconstructed from the first and third equation of (3.72). It is preferred to reconstruct the unknown input from the first equation as it involves no differentiation process. Then

$$\hat{w} = \frac{\nu(e_1)}{\tilde{d}_1}. \quad (3.77)$$

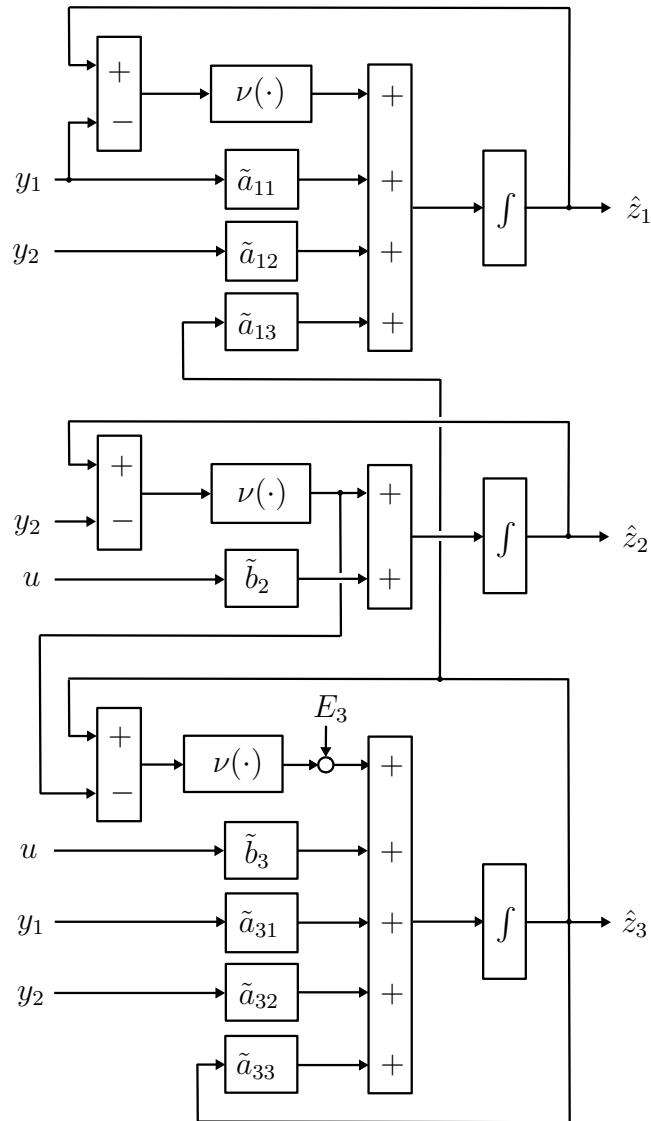


Figure 3.6: Step-by-step sliding mode observer for the power-train.

# Chapter 4

## Power-Train Control Concepts

In this chapter control concepts for a power-train of an electrically driven vehicle are presented. The control task is to track a given reference torque command  $T_{\text{ref}}$ . In general the command is transmitted via the vehicle's bus system from the ECU executing the operating strategy to the corresponding power-train ECU. The emphasis of the presented control concept is to cope with the backlash of *unknown* width within the power-train. On the one hand the controller has to track the reference torque and on the other hand the backlash-contact transitions have to be performed such that no noticeable torque overshoots occur.

The use of Sliding mode techniques allows to fulfill these requirements, since sliding mode is possible in the contact and backlash phase with an appropriate definition of the *sliding surface*. A first-order sliding mode control (SMC) concept is derived because it can be implemented in an embedded processor of a servo drive in addition to the field-oriented control. Additionally, the sliding mode design allows the analysis of the backlash phase. The control law needs the *state variables* which are estimated by the observers from section 3.2.3.

Methods for chattering reduction are analyzed, especially the so-called *boundary layer method*. The maximum control gain is determined with the help of a second-order actuator model. For the parameterization of the controller gain a differentiation has to be made in practice depending on whether the load speed is delayed or not.

In general chattering reduction methods are necessary for the implementation of first-order SMC. Therefore a reduced version of the so-called *Generic Second Order Algorithm* (GSOA) is applied for power-train control. The state variables are calculated by the second-order sliding mode observer from section 3.3.2.

For the integration of the proposed concepts into an automotive ECU additional algorithms are necessary. This involves a conditional usage of the delayed wheel speed signal and a concept for a very low vehicle velocity.

The first-order SMC concept is evaluated in a multi-body system (MBS) co-simulation for a hybrid electrical vehicle. The MBS system represents a detailed model of the electrically driven rear axle. The co-simulation includes the models of the wheel speed sensor and the bus system of section 2.5.

## 4.1 First-order sliding mode based control

In this section a power-train control law based on first-order sliding mode design techniques is derived. It is based on the work presented in [AH11]. Following the arguments in section 2.4.2 the control design incorporates the linear synthesis model (2.42).

### 4.1.1 Sliding surface design

The first task is to design the *sliding surface*. Define the error variable  $e$  as

$$e = \hat{\varphi} - \varphi_{\text{ref}}, \quad (4.1)$$

where  $\varphi_{\text{ref}}$  denotes the reference shaft torsion angle. It is determined by solving (2.1) for  $\varphi$  and by setting  $\dot{\varphi} = 0$ , i.e.

$$\varphi_{\text{ref}} = \frac{T_{\text{ref}}}{k_s}, \quad (4.2)$$

where  $T_{\text{ref}}$  denotes the reference shaft torque. Due to the structure of the synthesis model (2.42) the sliding surface has been chosen as follows:

#### Sliding surface design

$$\sigma = \dot{e} + \lambda e, \quad \lambda > 0. \quad (4.3)$$

Substituting the corresponding model equation of (2.42) and (4.1) into (4.3) the sliding surface  $\sigma$  corresponds to

$$\sigma = \frac{\omega_m}{k_g} - \omega_l - \dot{\varphi}_{\text{ref}} + \lambda(\hat{\varphi} - \varphi_{\text{ref}}), \quad (4.4)$$

where  $\hat{\varphi}$  and  $\dot{\varphi}_{\text{ref}}$  correspond to the estimated torsion angle the time-derivative of the reference torsion angle.

### 4.1.2 Power-train control design

The above definition of the sliding surface according to (4.3) allows that sliding mode is possible in the contact and backlash phase of the power-train controller. In order to enforce sliding mode, the so-called *reachability condition*, see e.g. [PB02], i.e.

$$\sigma \dot{\sigma} < 0 \quad (4.5)$$

has to be fulfilled. This can be achieved with the constraint

$$\dot{\sigma} = -K \operatorname{sgn}(\sigma), \quad (4.6)$$

where the parameter  $K > 0$  has to be sufficiently large such that sliding mode will be enforced within finite time, see [UGS09]. Differentiating (4.4) with respect

to the time, substituting the equations of the synthesis model (2.42) and solving the expression for the actuating signal yields the control law given by

$$u = u_{\text{eq}} - J_m k_g K \operatorname{sgn}(\sigma), \quad (4.7)$$

where  $u_{\text{eq}}$  corresponds to the *equivalent control* term which is given by

$$u_{\text{eq}} = d_m \omega_m + \left( \frac{1}{k_g} + \frac{J_m k_g}{\hat{J}_l} \right) k_s \hat{\varphi} - \frac{d_l J_m k_g}{\hat{J}_l} \omega_l - \frac{J_m k_g}{\hat{J}_l} \hat{T}_l + J_m k_g \ddot{\varphi}_{\text{ref}} - J_m k_g \lambda \left( \frac{\omega_m}{k_g} - \omega_l - \dot{\varphi}_{\text{ref}} \right). \quad (4.8)$$

The symbols  $\hat{J}_l$  and  $\hat{T}_l$  denote the estimated load inertia and the load torque estimate respectively. In (4.8) the damping coefficient  $d_s = 0$  was assumed for simplicity.

### Determination of the control gain

According to (2.33) the load inertia  $J_l$  depends on the vehicle mass which may vary. In (2.33) it is assumed that the tire slip is small. For spinning wheels the load inertia will significantly decrease. This fact should be considered in the determination of the controller gain  $K$ . With the Lyapunov function

$$V = \frac{1}{2} \sigma^2 \quad (4.9)$$

the attractiveness of the sliding surface  $\sigma = 0$  can be guaranteed if  $\dot{V} = \sigma \dot{\sigma} < 0$ . In section B.4 the time derivative of the sliding surface (4.4) is calculated for the case that the load inertia is not exactly known. The load inertia is assumed to be constant, i.e.

$$\hat{J}_l = J_l + \delta J_l. \quad (4.10)$$

Define the error of the load torque as

$$e_{T_l} = \hat{T}_l - T_l. \quad (4.11)$$

With (B.57) the time-derivative of (4.9) becomes

$$\begin{aligned} \dot{V} &= \sigma \dot{\sigma} \\ &= \sigma \left( -\frac{e_{T_l}}{\hat{J}_l} - \frac{\delta J_l}{\hat{J}_l} \dot{\omega}_l - K \operatorname{sgn}(\sigma) \right) \\ &\leq |\sigma| \left( \frac{|e_{T_l}|_{\max}}{\hat{J}_l} + \frac{|\delta J_l|_{\max}}{\hat{J}_l} |\dot{\omega}_l|_{\max} - K \right) \\ &\leq -\eta |\sigma|, \quad \eta > 0. \end{aligned} \quad (4.12)$$

The condition  $\sigma \dot{\sigma} \leq -\eta |\sigma|$  is also called the  $\eta$ -*reachability condition*, see [PB02]. For the finite time convergence to  $\sigma = 0$  within the *reaching time*  $t_r$ , i.e.

$$t_r \leq \frac{|\sigma(0)|}{\eta}, \quad (4.13)$$

the control gain  $K$  has to satisfy the following condition:

Control gain
$K \geq \frac{ e_{T_l} _{\max}}{\hat{J}_l} + \frac{ \delta J_l _{\max}}{\hat{J}_l}  \dot{\omega}_l _{\max} + \eta. \quad (4.14)$

For the implementation of the control law the corresponding state estimates are provided by the observers from section 3.2.3. For the delayed measurement of the load angular velocity the load torque can not be estimated correctly during the backlash phase. Then  $|e_{T_l}|_{\max}$  corresponds to the absolute maximum load torque.

### 4.1.3 Chattering reduction

The direct implementation of the control law would generate chattering which results from the unmodeled dynamics, such as neglected motor dynamics and the finite switching frequency.

In [UGS09] methods for chattering reduction are presented. The *'Equivalent control dependent gain method'* varies the control gain depending on the *equivalent control* term  $(\text{sgn}(\sigma))_{\text{eq}}$ . An estimate of the equivalent control term can be retrieved by a low-pass filter of the discontinuous control part. The *'Observer-Based Solution'* generates sliding mode in an auxiliary observer loop. These methods require the control law to be discontinuous.

In general the control concept has to cope with existing field-oriented control (FOC) implementations such that the actuating signal represents the reference signal for the underlying current control loop. This reference must be continuous such that high voltages are prevented due to the inductive nature of the electric motor. Therefore a *boundary layer solution* is chosen.

#### Boundary layer

The boundary layer solution implements a saturation function such that the control will be continuous [SL91]. In [ES98] also variants of the continuous approximation are given. In section 3.2.1 the saturation functions were used in the observer implementation. Fig. 4.1 shows the sliding surface (4.3) with the boundary layer

$$|\sigma| \leq \varepsilon_c \quad (4.15)$$

in the  $(e, \dot{e})$ -plane, where  $\varepsilon_c$  corresponds to the boundary layer width. If condition (4.14) is fulfilled the boundary layer is attractive. It follows from (4.3) and (4.15) that after finite time the absolute value of the torque error  $e_{T_s}$  for a constant reference torque is bounded by

$$|e_{T_s}| = |\hat{T}_s - T_{\text{ref}}| \leq \frac{\varepsilon_c}{\lambda} k_s. \quad (4.16)$$

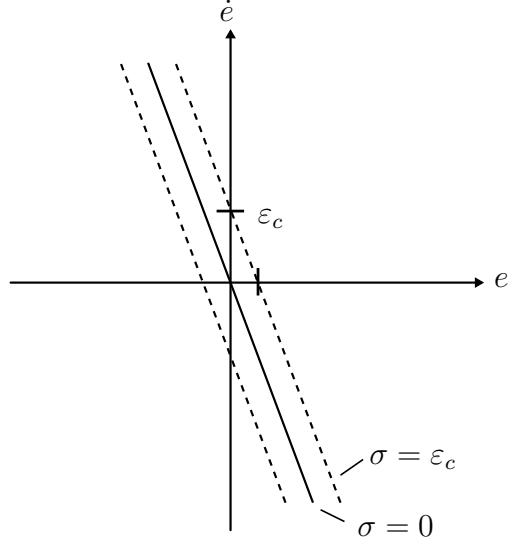


Figure 4.1: Boundary layer solution for chattering reduction.

For  $|\sigma| \leq \epsilon_c$  the slope of the linear part of the saturation function corresponds to  $1/\epsilon_c$ . Within the boundary layer the derivative of the sliding surface (4.3) is continuous such that (B.57) becomes

$$\dot{\sigma} = -\frac{K}{\epsilon_c}\sigma - \frac{e_{T_l}}{\hat{J}_l} - \frac{\delta J_l}{\hat{J}_l}\dot{\omega}_l. \quad (4.17)$$

Eq. (4.17) introduces a first-order low-pass filter with time constant  $\epsilon_c/K$ , i.e.

$$\dot{\sigma} = -\frac{K}{\epsilon_c}\sigma - \frac{K}{\epsilon_c} \left( \frac{\epsilon_c}{\hat{J}_l K} (e_{T_l} + \delta J_l \dot{\omega}_l) \right). \quad (4.18)$$

For the assumption that  $\sigma$  and the torque error  $e_{T_s}$  are constant within the boundary layer it follows from (4.3), (2.1) and (4.18) that the absolute value of the control error  $|e_{T_s}|$  corresponds to:

Control error of shaft torque

$$|e_{T_s}| = \frac{|\sigma| k_s}{\lambda} = \frac{\epsilon_c k_s}{\lambda \hat{J}_l K} |e_{T_l} + \delta J_l \dot{\omega}_l|. \quad (4.19)$$

### Stability within the boundary layer in presence of second-order actuator dynamics

In the synthesis of the control law (4.7) the actuator dynamics is neglected. High control gains in combination with small boundary layer widths will lead to instability within the boundary layer which generates chattering, see for example [UGS09]. For the stability analysis only the linear high-gain control term is

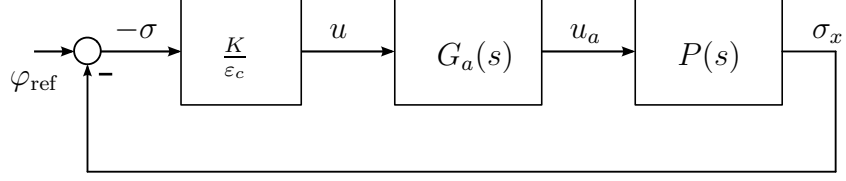


Figure 4.2: Closed loop transfer function for stability analysis of the control law within the boundary layer.

applied, i.e.

$$u = -\frac{K}{\varepsilon_c}\sigma = -V\sigma. \quad (4.20)$$

Linear second order actuator dynamics is assumed. Its transfer function  $G_a(s)$  has the shape of (2.13). The sliding surface (4.3) can be rewritten as

$$\sigma = \underbrace{\mathbf{c}_\sigma^T \mathbf{x}}_{=:\sigma_x} - \lambda\varphi_{\text{ref}} - \dot{\varphi}_{\text{ref}}, \quad (4.21)$$

where

$$\mathbf{c}_\sigma^T = \left[ \lambda \quad -1 \quad \frac{1}{k_g} \right]. \quad (4.22)$$

The transfer function  $P_\sigma(s)$  from the plant input  $u$  to the output  $\sigma_x$  is involved in the control loop as shown in Fig. 4.2. It corresponds to

$$P_\sigma(s) = \frac{\sigma_x(s)}{u(s)} = \mathbf{c}_\sigma^T (s\mathbf{I} - \mathbf{A})^{-1} \mathbf{b}. \quad (4.23)$$

The transfer function  $T_\sigma(s)$  of the closed-loop system is

$$T_\sigma(s) = \frac{VG_a(s)P_\sigma(s)}{1 + VG_a(s)P_\sigma(s)}. \quad (4.24)$$

The gain  $V = K/\varepsilon_c$  has to be designed such that the roots of the denominator of (4.24) are located in the open complex left half-plane.

#### 4.1.4 Controller analysis in backlash phase

In this section the difference angular velocity

$$\bar{\omega} = \frac{\omega_m}{k_g} - \omega_l \quad (4.25)$$

in the backlash phase is determined. On the one hand, a large difference angular velocity causes a torque jerk at the backlash contact transition. On the other hand, a too slow difference angular velocity results in poor control behavior. The behavior of the controlled power-train during the backlash phase is determined by the definition of the sliding surface (4.3).

First, it is assumed that the control gain is sufficiently large such that  $\sigma \equiv 0$  can be fulfilled also during the backlash phase. It is further assumed that the estimated torsion angle  $\hat{\varphi}$  is small and therefore can be neglected. Solving (4.4) for  $\bar{\omega}$  yields

$$\bar{\omega} = \dot{\varphi}_{\text{ref}} + \lambda\varphi_{\text{ref}}. \quad (4.26)$$

The realization of the controller of section 4.1.2 is based on a boundary layer of width  $\varepsilon_c$ . As in section 4.1.2 it is assumed that the load inertia is not exactly known. The differential equation for  $\bar{\omega}$  can be determined from the second and third equation of (B.51) such that

$$\dot{\bar{\omega}} = -\frac{d_m}{k_g J_m}\omega_m + \frac{d_l}{J_l}\omega_l + \frac{T_l}{J_l} + \frac{T_m}{k_g J_m}. \quad (4.27)$$

By substitution of the control law (4.7) into (4.27) and assuming that  $\hat{\varphi} = 0$ ,  $\dot{\varphi}_{\text{ref}} = 0$  and  $\ddot{\varphi}_{\text{ref}} = 0$  the sliding surface (4.3) can be expressed in terms of  $\bar{\omega}$ , i.e.

$$\sigma = \bar{\omega} - \lambda\varphi_{\text{ref}}. \quad (4.28)$$

It is further assumed that the absolute value of the load angular acceleration  $|\dot{\omega}_l|$  is small such that it can be neglected. With (B.55) and (B.56) the dynamics of the difference speed  $\bar{\omega}$  in the backlash phase corresponds to

$$\dot{\bar{\omega}} = -\frac{e_{T_l}}{\hat{J}_l} - \left( \frac{\lambda\varepsilon_c + K}{\varepsilon_c} \right) \bar{\omega} + \frac{K\lambda}{\varepsilon_c}\varphi_{\text{ref}}. \quad (4.29)$$

The steady state difference angular velocity is given as:

Difference angular velocity in backlash phase

$$\bar{\omega} = -\frac{\varepsilon_c}{\lambda\varepsilon_c + K} \frac{e_{T_l}}{\hat{J}_l} + \frac{K\lambda}{\lambda\varepsilon_c + K}\varphi_{\text{ref}}. \quad (4.30)$$

This means that the difference angular velocity depends on the reference torque in the backlash phase and the design parameters  $\lambda$ ,  $K$  and  $\varepsilon_c$  and the load torque estimation error. For a small value of the boundary layer width  $\varepsilon_c$  the difference angular velocity  $\bar{\omega}$  approximately corresponds to

$$\bar{\omega} \approx \lambda\varphi_{\text{ref}}. \quad (4.31)$$

Due to (4.2) the difference angular velocity also depends on the shaft stiffness. In general the reference torsion angle  $\varphi_{\text{ref}}$  is small which results in a small difference angle such that the transition from the backlash to the contact phase is smooth.

#### 4.1.5 Remarks on the definition of the sliding surface

The use of a boundary layer implies that the steady-state error will not decay to zero, see (4.19). The sliding surface (4.3) can be extended by an integral term,

see for example [SL91], such that the sliding surface corresponds to

$$\sigma = \dot{e} + 2\lambda e + \lambda^2 \int e dt, \quad \lambda > 0. \quad (4.32)$$

Due to the integral term the actuating signal reaches comparably large values in the backlash phase such that a too large difference angular velocity  $\bar{\omega}$  causes a torque overshoot after the backlash-contact transition. For small values of  $\lambda$  the control performance significantly deteriorates.

Chattering results from unmodeled dynamics and the finite switching frequency. The actuator dynamics can be approximated, for example by a first-order system with time constant  $\tau_a$ , i.e.

$$\tau_a \dot{T}_m = -T_m + T_{m,\text{ref}}. \quad (4.33)$$

Then the relative degree of the sliding surface  $\sigma$  with respect to the control input, the motor reference torque  $T_{m,\text{ref}}$ , has to be increased, i.e.

$$\sigma = \ddot{e} + 2\lambda\dot{e} + \lambda^2 e. \quad (4.34)$$

It follows from (2.42) and (4.33) that the unknown load torque  $T_l$  appears in the sliding surface (4.34) which has to be estimated. This can lead to unwanted control action, for example by using the estimate for  $\hat{T}_l$  from the observer in section 3.2.2.

The sliding surface can be designed as the error variable as introduced in (4.1). Then the relative degree of  $\sigma$  with respect to the control input is two. The power-train can be controlled for example by means of the twisting algorithm, see [Lev93]. In the backlash phase however, sliding mode cannot occur since the reference does not correspond to the real shaft torque, i.e.  $\sigma \neq 0$ . As a consequence there will be an overshoot at the backlash contact transition.

## 4.2 Power-train control software

The functionality of the control concept must be guaranteed even at low vehicle speeds, where the load angular velocity signal is not reliable. Therefore additional software modules are necessary. The first module determines whether the wheel speed signal is used in the observer. The second module limits the reference torque and its gradient at very low vehicle speeds. It is assumed that the control software is implemented in the power-train ECU together with the field-oriented control (FOC) of the EM. Fig. 4.3 shows the concept of the power-train control software.

### 4.2.1 Conditional usage of the delayed correction term

During the backlash phase the knowledge of the load angular velocity signal is of essential importance for a good control performance. But the delayed correction term

$$\mathbf{l}_2 e_{\omega_l}(t - \tau(t)) \quad (4.35)$$

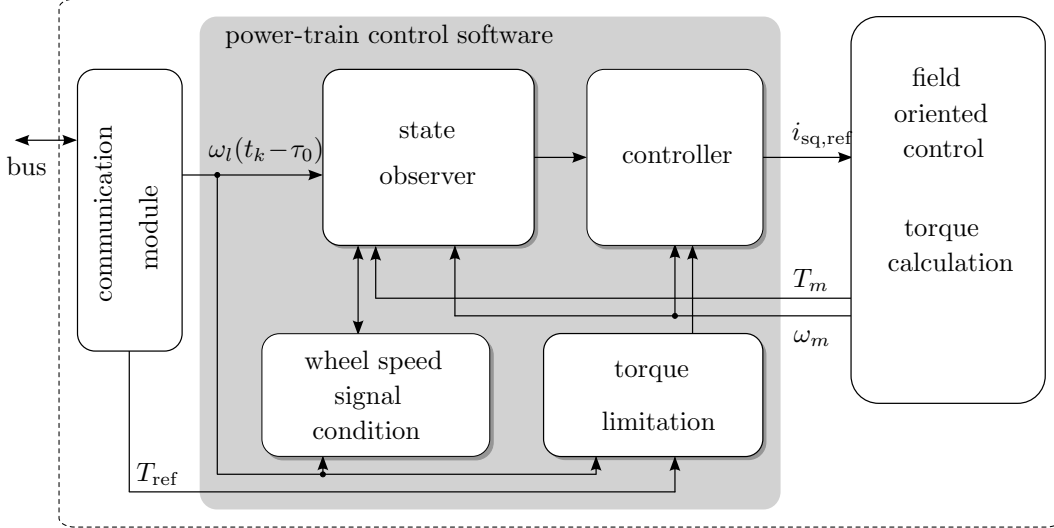


Figure 4.3: Overview of the controller software.

of observer (3.32) cannot be used at low vehicle speeds. This is accomplished by an additional multiplicative term which enables or disables (4.35) in the observer (3.32). The enabling or disabling of (4.35) in the state estimator should only be accomplished in the contact phase. The contact phase can be detected if, for example, the absolute value of the estimated shaft torque exceeds a predefined threshold.

In general the load angular velocity signal is affected by noise. In the case of the delayed and sampled load angular velocity signal a disturbance remains constant between two consecutive samples, i.e. bus signals. These disturbances prevent that the observation error completely vanishes. Therefore it is proposed to use the delayed correction term (4.35) in the state observer only when traversing the backlash phases. For example, it can be enabled when the absolute value of estimated shaft torque is lower than a certain threshold value. This can be performed without a very small impact to the state estimates because the observer (3.32) represents one dynamical system.

The conditional usage of the delayed correction term (4.35) in observer (3.32) can be managed by the following boolean condition

$$d(\hat{T}_s, \omega_l(t - \tau(t))) = \begin{cases} 1 & \text{for } |\hat{T}_s| < T_{th} \wedge |\omega_l(t - \tau(t))| > \omega_{th} \\ 0 & \text{for } |\hat{T}_s| \geq T_{th} \vee |\omega_l(t - \tau(t))| \leq \omega_{th} \end{cases}, \quad (4.36)$$

where  $T_{th}$  and  $\omega_{th}$  denote the corresponding threshold values. The threshold value with respect to the shaft torque  $T_{th}$  has to be sufficiently large such that the switching of the correction term is accomplished when there is contact in the power-train. The threshold value  $\omega_{th}$  corresponds to a sufficiently large wheel speed.

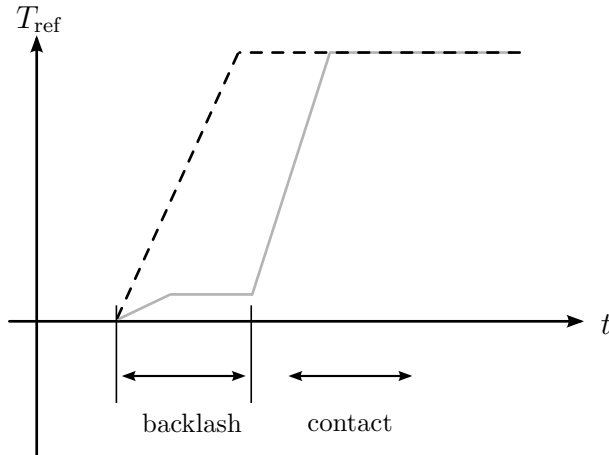


Figure 4.4: Limitation of the reference torque and its gradient within the backlash phase for the case that no load angular signal is available.

### 4.2.2 Reference torque limitation

At low vehicle speeds the control concept has no information about the load angular velocity. Consequently torque overshoots cannot be suppressed by the control at the backlash-contact transitions. Therefore it is necessary to limit the reference torque and its gradient. Fig. 4.4 shows the concept of torque limitation.

## 4.3 Multi-body system simulation

For the evaluation of the control concept a multi body system (MBS) model of the power-train of an electrically driven rear axle from a prototype hybrid vehicle of Magna Steyr Fahrzeugtechnik<sup>1</sup> has been generated. The prototype vehicle is a Fiat Panda with 1200 cm<sup>3</sup> integrated combustion engine which consists additionally of an electrically driven rear axle. The traction motor is a synchronous machine with a peak torque of 72 N m. The peak power is 23 kW. Details about the vehicle and the hybrid power-train can be found in [SSK10].

### 4.3.1 Model of an electrically driven rear axle

In Figure 4.5 the Adams/Car<sup>2</sup> MBS model of the electrically driven rear axle power-train is depicted. The differential gear is placed off the center of the axle such that the drive shafts have different length and stiffness. They are connected with the differential gear by tripod joints. The three small flat cylinders show the mountings at the vehicle body. They are modeled as stiff springs.

Since the MBS model consists only of the axle the wheels interact with a roll.

<sup>1</sup>www.magnasteyr.com

<sup>2</sup>www.mscsoftware.com

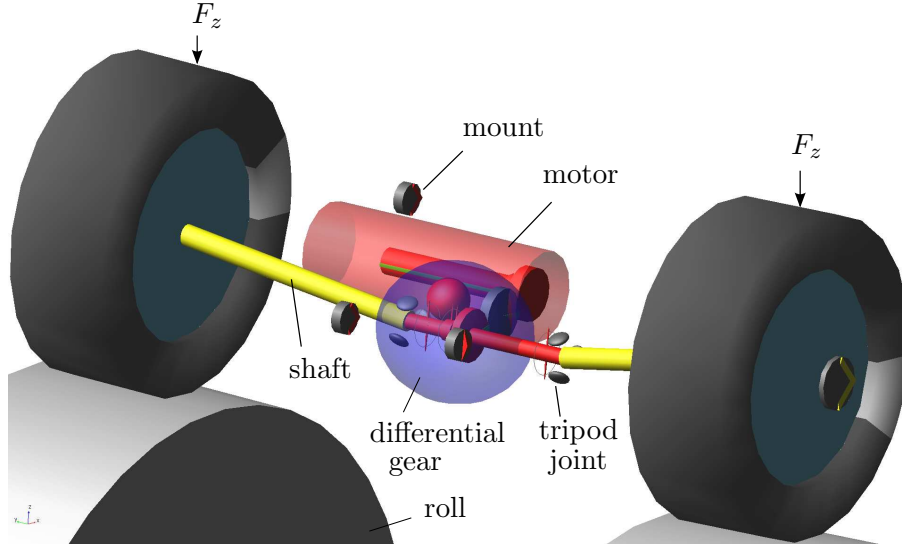


Figure 4.5: Multi Body System model of an electrically driven rear axle of a hybrid prototype vehicle.

A constant vertical force of

$$F_z = \frac{m_v g}{4} \quad (4.37)$$

acts on the wheels, where  $m_v$  denotes the vehicle mass. The roll has been designed such that its inertia corresponds to 50% of the total vehicle mass, i.e.

$$J_{\text{roll}} = \frac{m_v r_{\text{st}}^2}{2}, \quad (4.38)$$

since the traction motor at the rear axle supports the combustion engine, e.g. with all wheel drive functionality.

For the used tires with dimension of 165 × 65 R14 a model for dry road is available. It consists of a set of adhesion coefficients  $\mu(s_x)$  in dependence of the longitudinal tire slip. The longitudinal tire force, as shown in Fig. 4.6, is obtained by multiplication of the tire slip with the vertical force, i.e.  $F_x = \mu(s_x)F_z$ . In addition to the tire model, the tire itself is modeled as a torsional elastic element.

Each drive shaft is modeled by two identical inertias and a spring-damper element in-between. The magnitudes of the damping coefficients have been set to 0.5% of the corresponding stiffness magnitudes. The remaining elements of the power-train, such as the differential gear, are modeled as stiff components. The backlash has been modeled between rotor and differential gear and at the tripod joints. Tab. C.14 shows the parameters of the MBS model which result from CAD design of the prototype parts of the power-train. Tab. C.15 shows the moments of inertias of the power-train parts.

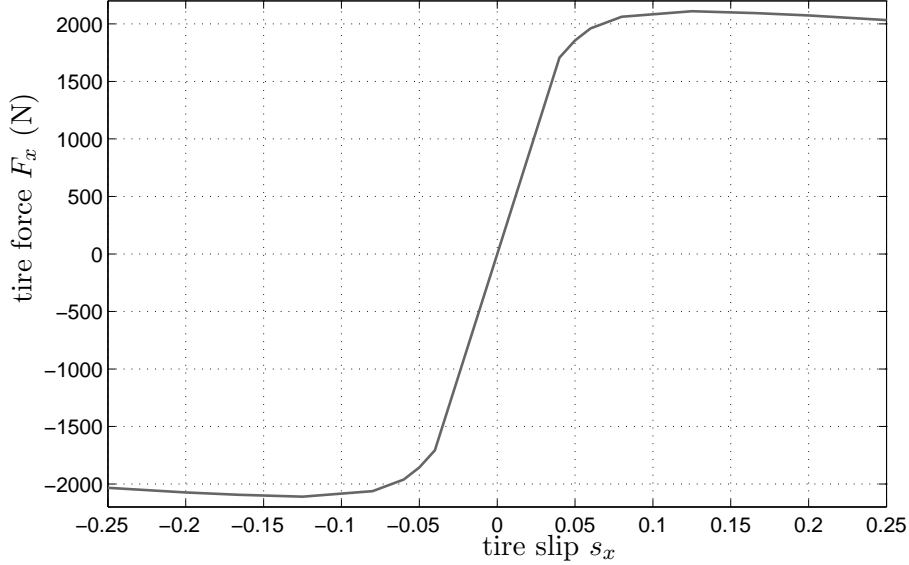


Figure 4.6: Longitudinal tire force  $F_x$  versus tire slip  $s_x$ .

### 4.3.2 Implemented control concept

Fig. 4.7 shows the implemented control concept. The state observer corresponds to that of section 3.2.3 incorporating the delayed load angular velocity and the controller corresponds to that of section 4.1.2. A model of an automotive wheel speed sensor according to section 2.5 is used in the simulation. The sensor model is applied to the load angular velocity signal according to (2.30). The wheel speed sensor signal is filtered by a first-order low-pass filter with time constant  $\tau_f = 5$  ms. Subsequently it is delayed by 2 ms and sampled every 5 ms. The signal delay of the sensor is also considered in the observer. The delay is calculated from the time difference  $\Delta t$  of traversing a magnetic sensor unit.

Due to the low resolution of the wheel speed sensor a strategy for very low vehicle speeds according to section 4.2 has been applied. The error of the delayed load speed signal  $\omega_l(t - \tau(t))$  is used in the observer if

$$|\hat{T}_s| < 50 \text{ N m} \quad \text{and} \quad |\hat{\omega}_l| > 8 \text{ rad s}^{-1}.$$

### 4.3.3 Controller and observer parameters

The overall stiffness  $k_s$  of the power-train has been set to the sum of the shaft stiffnesses such that  $k_s = 140 \text{ Nm}/^\circ$ . The damping coefficients  $d_m$  and  $d_l$  have been both set to  $0 \text{ N m s rad}^{-1}$ . Tab. 4.1 shows the controller and observer parameters. The observer gains  $\mathbf{l}_1$  and  $\mathbf{l}_2$  of the observer according to (3.32) have been set by pole placement. The spectra  $\sigma(\mathbf{A}_0)$  and  $\sigma(\mathbf{A}_0 + \mathbf{A}_1)$  were chosen according to Tab. 4.1.

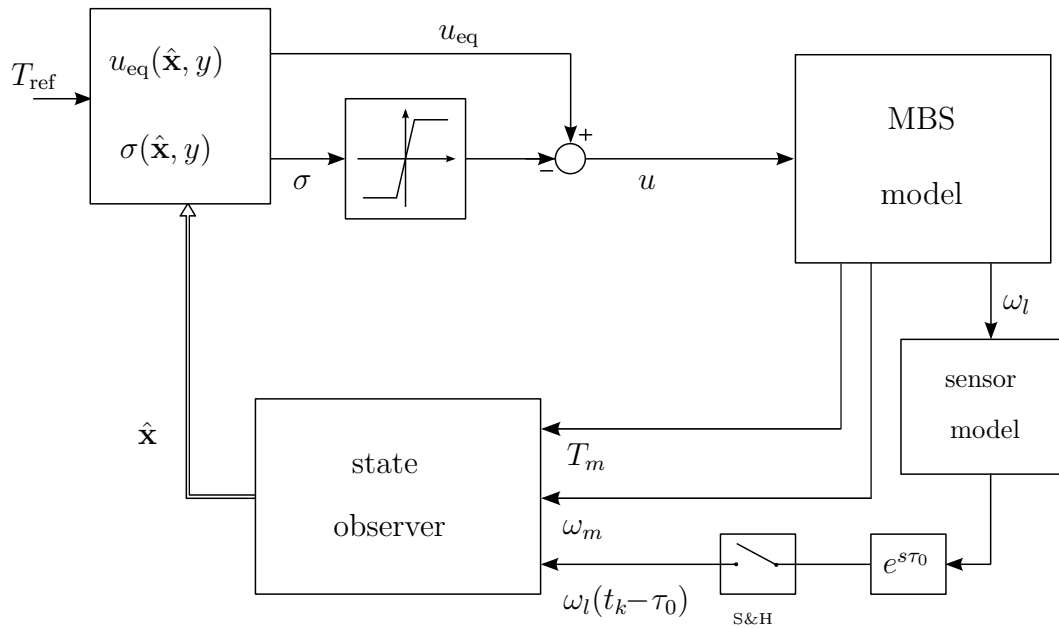


Figure 4.7: Observer-based Sliding Mode Control evaluated with a MBS model of an electrically driven rear axle power-train.

Table 4.1: Controller and observer parameters of the control concept for the MBS simulation.

<b>Controller</b>		<b>Observer</b>	
$K$	60	$M$	5000
$\lambda$	110	$\varepsilon_o$	1
$\epsilon_c$	1	$\sigma(\mathbf{A}_0)$	$\{-180, -180 \pm 40j\}$
		$\sigma(\mathbf{A}_0 + \mathbf{A}_1)$	$\{-210, -210 \pm 40j\}$

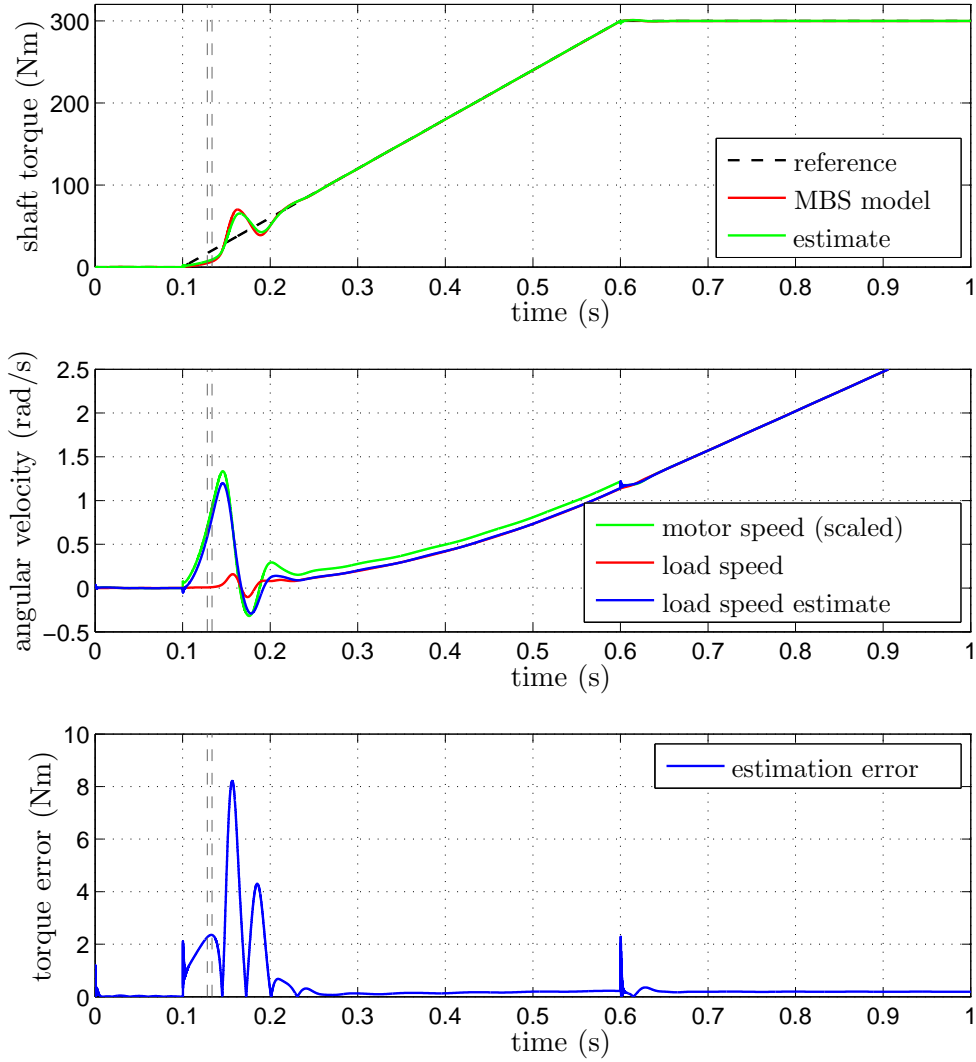


Figure 4.8: Multi Body System simulation of the control concept at an acceleration maneuver.

#### 4.3.4 Simulated maneuvers

The Adams/Car MBS model was simulated in a co-simulation with Matlab/Simulink. The sampling time in Simulink was set to 0.1 ms. In the simulation the reference shaft torque is increased to 300 N m. After some seconds the reference torque changes to  $-150$  N m. The magnitude of the torque gradient is limited to  $600$  N m s $^{-1}$ .

Fig. 4.8 shows the acceleration maneuver from standstill. The top graph shows the reference and the actual shaft torque. The middle graph shows the motor speed speed divided by  $k_g$ , the load speed and its estimate. The lower graph plots the estimation error of the shaft torque  $|\hat{T}_s - T_s|$ . Fig. 4.9 shows the deceleration maneuver, where the shaft torque changes its sign such that energy can be regenerated.

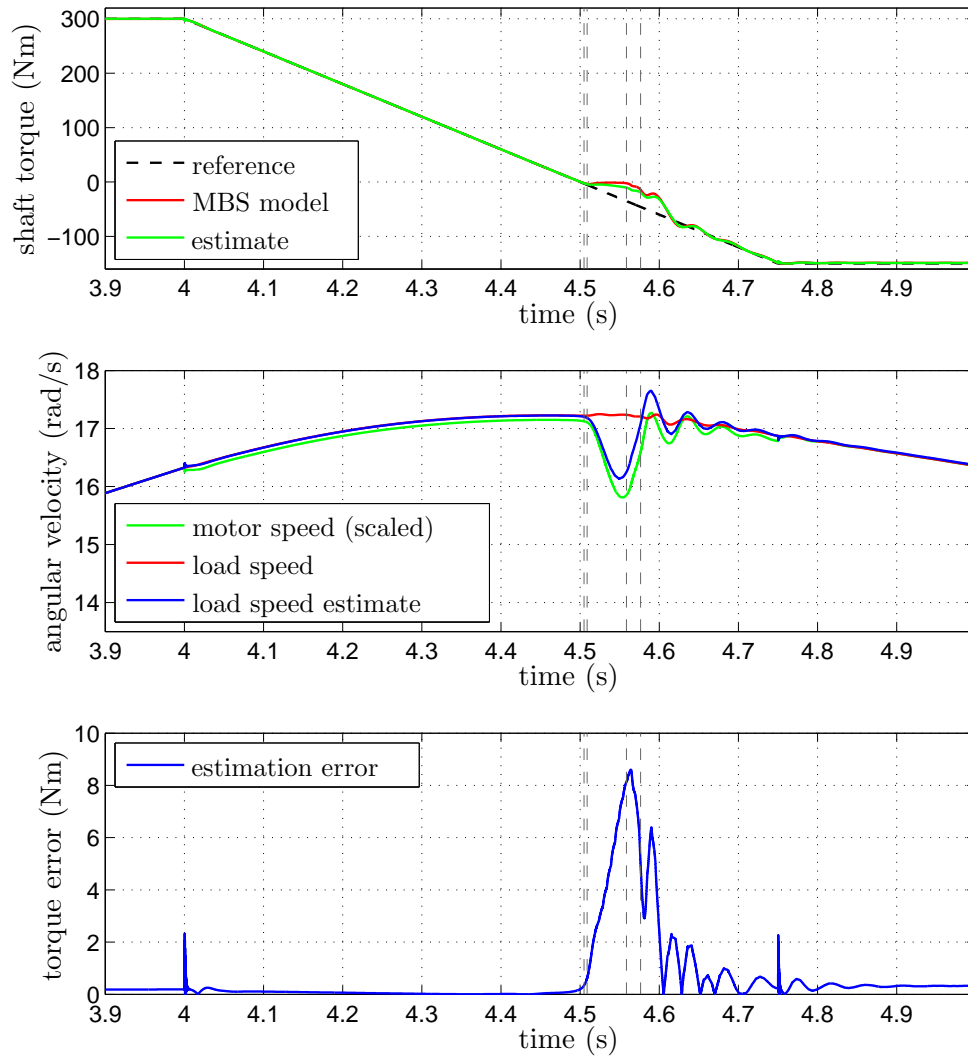
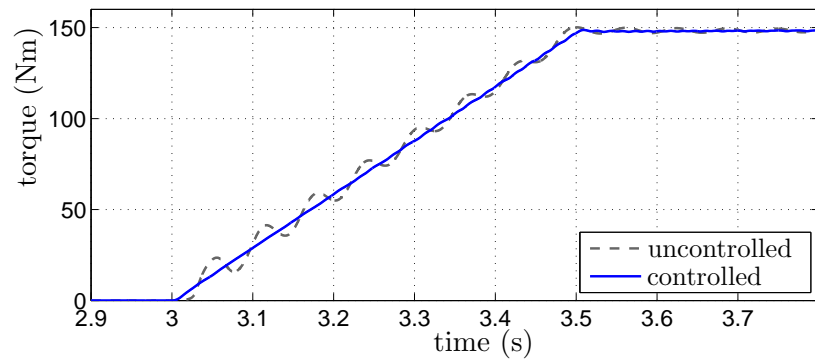
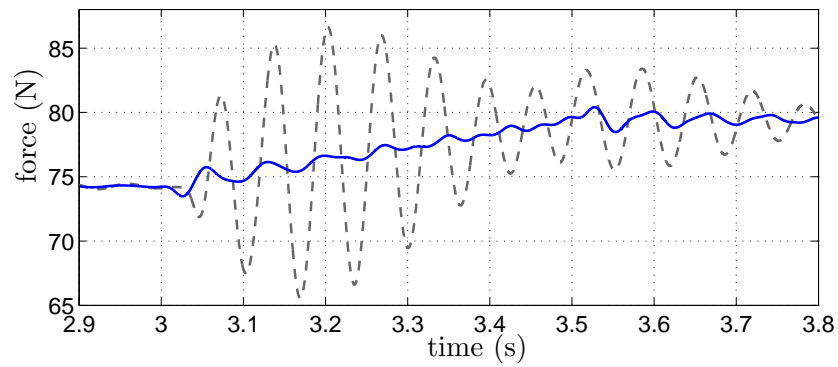


Figure 4.9: Multi Body System simulation of the control concept at an deceleration maneuver.



(a) Shaft torque at left half shaft.



(b) Force at motor mounting in z-direction.

Figure 4.10: Comparing the control concept with the uncontrolled simulation.

The dashed vertical lines show the transition of the backlash phase to the contact phase and vice versa. Due to the fact that the backlash is modeled between motor and differential gear and within the tripod joints two lines are plotted at each transition.

In the simulated concept the load inertia  $J_l$  consists only of the wheel inertias. Due to the delayed load angular velocity signal the load torque estimation is not reliable in the backlash phase. Therefore the load torque estimate was not used in the controller such that a steady-state control error remains. The error feedback of the delayed load angular velocity was activated in the observer at about  $t = 4.41s$ . This can be seen in the lower plot of Fig. 4.9, where the estimation error slightly increases. This is due to the approximation of the delay of the sensor by  $\Delta t$  and the group delay of the low-pass filter.

Finally Fig. 4.10a compares the control concept with the uncontrolled power-train. Fig. 4.10b shows the vertical force in z-direction of the rear mounting beside the motor. It can be seen that the oscillations at the mounting can be significantly reduced.

## 4.4 Generic second order algorithm (GSOA)

For the first-order sliding mode based control concept from section 4.1 appropriate chattering reduction methods have to be applied. By the use of a saturation function finite time convergence to  $\sigma = 0$  is only possible outside of the boundary layer of the sliding surface. By the use of second-order sliding mode algorithms, such as the super-twisting algorithm, chattering can be mitigated. In this section the so-called *Generic Second Order Algorithm* (GSOA), as proposed by [Mor11], is applied for power-train control. The concept is based on the work presented in [ARH12]. Due to limited computational power only a sub-set of the algorithm incorporating the lower-order terms is considered.

### 4.4.1 GSOA with lower-order terms

The GSOA with lower-order terms corresponds to

$$\begin{aligned}\dot{\sigma}_1 &= -k_1 |\sigma_1|^p \operatorname{sgn}(\sigma_1) + \sigma_2 + \rho_1 \\ \dot{\sigma}_2 &= -k_2 p |\sigma_1|^{2p-1} \operatorname{sgn}(\sigma_1) + \rho_2,\end{aligned}\tag{4.39}$$

where  $1/2 \leq p \leq 1$ ,  $k_1 > 0$ ,  $k_2 > 0$ ,  $\rho_1$  and  $\rho_2$  correspond to bounded disturbances. Depending on the parameter  $p$  the algorithm (4.39) has different properties:

- For  $p = 1/2$  the algorithm (4.39) corresponds to a second order sliding mode algorithm, namely the super twisting algorithm.
- For  $1/2 < p < 1$  the algorithm (4.39) is continuous, but not Lipschitz continuous.
- For  $p = 1$  it is linear.

In [Mor11] the stability determination of the GSOA including disturbances is based on Lyapunov methods. It is assumed that the disturbances satisfy the sector conditions

$$\begin{aligned} |\rho_1| &\leq g_1 \left| |\sigma_1|^p \operatorname{sgn}(\sigma_1) + \sigma_2 \right|, \\ |\rho_2| &\leq g_2 \left| \frac{1}{2} |\sigma_1|^{2p-1} \operatorname{sgn}(\sigma_1) \right|. \end{aligned} \quad (4.40)$$

This means that the disturbances have to vanish at the origin  $\boldsymbol{\sigma} = [\sigma_1, \sigma_2]^T$ . For  $p = 1/2$  the disturbance  $\rho_2$  does not have to vanish, i.e.  $|\rho_2| \leq g_2/2$ . For the case that  $\rho_1 = 0$  finite time convergence to the origin  $\boldsymbol{\sigma} = \mathbf{0}$  can be achieved with the parameters

$$k_1 > g_2, \quad k_2 > \frac{k_1^2}{2}. \quad (4.41)$$

For the case that the disturbances do not correspond to the sector conditions (4.40) the trajectories of (4.39) converge to a neighborhood of  $\boldsymbol{\sigma} = \mathbf{0}$  in finite time for bounded disturbances

$$|\rho_1| < \delta_1, \quad |\rho_2| < \delta_2,$$

for  $k_1 > 0, k_2 > 0$ . According to [Mor11] this is also called "practical stability" and means that the trajectories are uniformly ultimately bounded, see [Kha02]. For that case the parameters have to be determined experimentally.

#### 4.4.2 Power-train control design

As in section 4.1 the control design involves the linear synthesis model (2.42). The sliding surface is defined according to (4.3). It is assumed that the corresponding states can be estimated in finite-time, for example by the observer from section 3.3. Choosing the control input  $u$  such that the closed loop dynamics corresponds to (4.39), the control law reads as

$$\begin{aligned} u &= J_m k_g (-k_1 |\sigma_1|^p \operatorname{sgn}(\sigma_1) + \sigma_2) + u_{\text{eq}}, \\ \dot{\sigma}_2 &= -k_2 p |\sigma_1|^{2p-1} \operatorname{sgn}(\sigma_1), \end{aligned} \quad (4.42)$$

where  $u_{\text{eq}}$  corresponds to (4.8). Only the derivative of the disturbance is considered with the term  $\rho_2$ . This means that  $\rho_1 = 0$ . As in section 4.1.2 it is assumed that the constant load inertia  $\hat{J}_l$  is not exactly known. Additionally an error in the load torque estimate  $e_{T_l}$  is considered. In (B.57) the dynamics of  $\sigma$  with respect to the first-order sliding mode control is given. The derivative of the disturbance corresponds to  $\rho_2$  which is

$$\rho_2 = -\frac{\dot{e}_{T_l}}{\hat{J}_l} - \frac{\delta J_l}{\hat{J}_l} \ddot{\omega}_l. \quad (4.43)$$

# Chapter 5

## Test Bench Design and Concept Verification

For the practical verification of the presented control concepts a test bench has been realized. It reproduces a basic automotive power-train with a traction machine, gear backlash, a low-damped elastic axle, a wheel and a load. The control performance concerning tracking behavior, oscillation damping and the backlash transitions are investigated within the real-world environment. Since the control variable has to be calculated by an observer the quality of the estimated states is verified. The control concept is affected by the unknown load torque, nonlinear friction due to the rolling resistance and tire slip. Additionally a time-varying delay is introduced to simulate the effect of an automotive bus system.

From the goals and requirements with respect to the test bench mechanics detailed design drawings were generated. Special emphasis was made on the torsion bar which is a compromise of a large torsion angle and a high fatigue strength. Additionally a CAD model was drawn. The test bench design involved the choice of appropriate electrical parts, such as EM, servo drive, interfaces and rotary encoders. Induction machines were chosen to be used at the test bench. The motor torque is an estimate from the machine parameters and the measured stator current of the q-component. For its calculation the direction-dependent motor losses are considered phenomenologically. The torque at the torsion bar can be determined with the help of the rotary encoders.

The tire parameters are determined experimentally. These are the speed-dependent rolling resistance, the tire force depending on the longitudinal tire slip and the tire torsional stiffness and the corresponding damping coefficient.

The implemented state estimation concepts are the observers of section 3.2.3 and section 3.3.2. The implemented control concepts are those presented in section 4.1 and section 4.4.2. The concepts are implemented in addition to the FOC software in C at the servo drive. This requires that the implemented algorithms are not computationally expensive. Experiments were made in order to demonstrate the performance of the implemented control and observer concepts.

## 5.1 Mechanical test bench design



Figure 5.1: Test bench for investigating the power-train control concepts.

### 5.1.1 Design goals

For the mechanical design of the test bench the following goals and requirements were considered:

- Construction of a low-damped system such that torsional oscillations with a low frequency can arise.
- Smaller nominal torques compared to series electric vehicles.
- Adjustable gear backlash within the power-train.
- Availability to apply different tire-road friction forces.
- Possibility to apply additional load torques or disturbances.
- Measurement of the torque at the torsion bar.

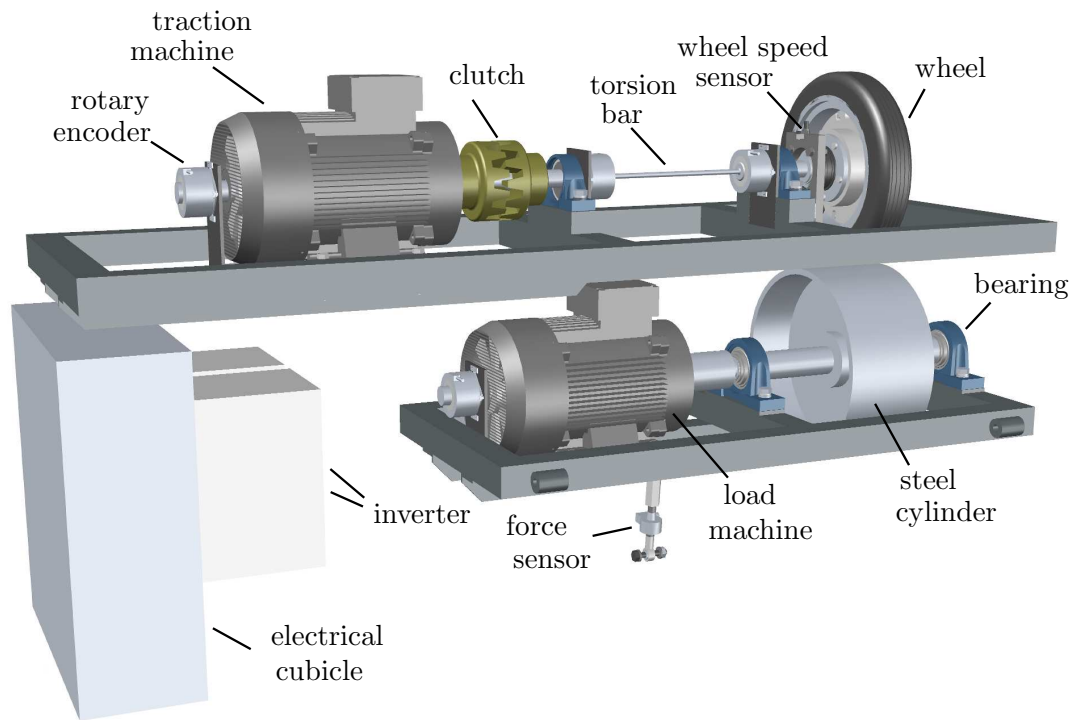


Figure 5.2: Test bench without metal frame.

### 5.1.2 Test bench realization

Fig. 5.1 shows the test bench construction which consists mainly of two parts. The upper part represents the power-train of a single axle of an electrically driven vehicle. It consists of the traction machine, the coupling with backlash, the torsion bar and the wheel. The lower part consists of the metal cylinder, which represents the road, and the load machine. The traction machine can be moved horizontally to adjust the backlash width at the coupling. The maximum backlash width is ten degrees. The torsion bar is made of spring steel and reproduces a drive shaft of a vehicle. Rotary encoders are mounted at both ends of the torsion bar such that the torque can be determined by the stiffness and damping coefficient and the measurement of the torsion and its derivative. Fig. 5.2 shows the CAD model of the test bench without the metal frame. Tab. C.1 shows some basic parameters of the test bench such as the geometrical dimensions.

The lower part can be moved manually such that the vertical force between the tire and the metal cylinder can be adjusted. Additionally a force sensor is mounted. The cylinder has a smooth and a rough surface such that two different friction values are available. With the help of the load machine additional load torques or disturbances can be applied.

By assigning the mass density to the corresponding parts the mass moments of inertia were calculated by the CAD software AutoCAD<sup>1</sup>. The mass density of the tire was estimated by its weight and volume. Tab. C.2 shows the mass moments

---

<sup>1</sup>www.autodesk.de

of inertia of the corresponding parts of the test bench.

For future applications an automotive series wheel speed sensor, as described in section 2.5, is mounted next to the wheel.

### 5.1.3 Torsion bar design

According to Hooke's law the torque at the torsion bar corresponds to the torsion angle multiplied with the shaft stiffness  $k_s$ . For a cylindrical steel shaft the stiffness can be calculated by

$$k_s = \frac{\pi r^4 G}{2 l}, \quad (5.1)$$

where  $r$  and  $l$  correspond to the radius and the length of the shaft [Föl08]. The elastic properties are defined by the *shear modulus*  $G$ .

The torsion bar is made of a hardened and tempered spring steel from Böhler<sup>2</sup> and has a total length of 50 cm including the mountings for the sensors and the feather keys below the ball bearings on both ends. The visible part is of reduced thickness and defines mainly the elasticity. It has a total length of 30 cm. Tab. C.4 shows the parameters of the torsion bar. The stiffness of the torsion bar was designed with the help of the software KISSsoft<sup>3</sup> such that fatigue durability<sup>4</sup> is guaranteed for torque steps with the maximum motor torque of 140 N m. This results in a thickness of 16.6 mm.

## 5.2 Electrical topology

Figure 5.3 shows the electrical topology of the test bench. It shows the traction motor, the servo drive or inverter and the rotary encoders.

For the motor control industrial servo drives (type ACOPOS) from Bernecker & Rainer<sup>5</sup> have been chosen. They require a three-phase 400 V AC and a 24 V DC power supply. They are provided with four plug-in module slots. Tab. C.11 shows the basic parameters of the ACOPOS servo drive. The AC power supply requires an all-current sensitive earth-leakage circuit breaker. The test bench is equipped with an emergency-stop button and is protected with 20 A fuses per phase.

Two identical induction machines with squirrel cage rotor from AEG/Lafert<sup>6</sup> are mounted on the test bench. The motor housings are made of aluminium and have a total weight of 54 kg each. Tab. C.9 shows the motor parameters.

High resolution encoders for angular position and velocity measurement are mounted at the motors and at both ends of the torsion bar. The sensors are single turn absolute angle encoders of type ECN/ERN 100 from Heidenhain<sup>7</sup>. Tab. C.10 shows the basic parameters of the rotary encoders.

---

<sup>2</sup>[www.bohler-bleche.com](http://www.bohler-bleche.com)

<sup>3</sup>[www.kisssoft.ch](http://www.kisssoft.ch)

<sup>4</sup>2 000 000 load changes were assumed.

<sup>5</sup>[www.brautomation.com](http://www.brautomation.com)

<sup>6</sup>[www.lafert.com](http://www.lafert.com)

<sup>7</sup>[www.heidenhain.com](http://www.heidenhain.com)

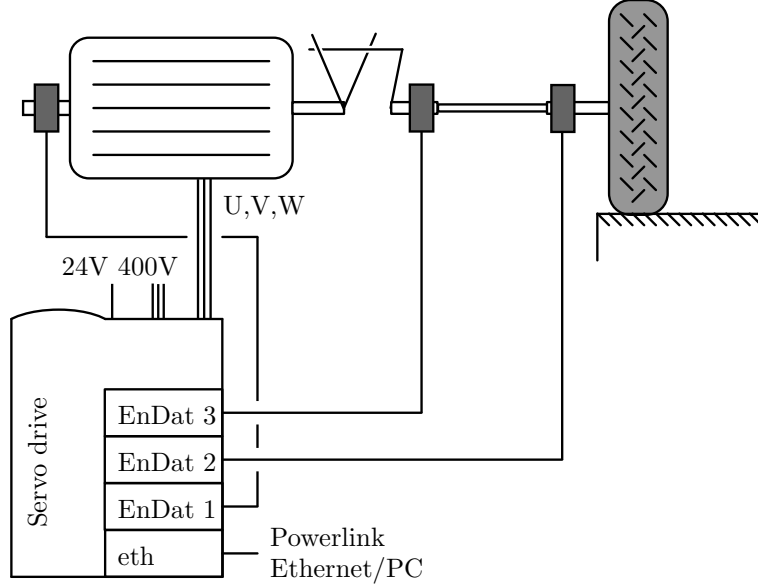


Figure 5.3: Testbench configuration.

## 5.3 Parameter identification

### 5.3.1 Motor torque calculation

In the inverter the concept of field-oriented control (FOC) is implemented. The voltage, flux and current are represented by two-dimensional phasors. In the rotating rotor-flux reference frame, denoted by the  $(d, q)$ , the rotor flux phasor consists only of the d-axis component such that it is a scalar, namely  $\Psi_{rd}$ . The motor torque can be calculated by, see [QD99],

$$T_m = \frac{3}{2}p \frac{L_h}{L_r} \Psi_{rd} i_{sq}, \quad (5.2)$$

where  $p$ ,  $L_h$  and  $L_r$  denote the number of pole pairs, the mutual inductance and the rotor inductance respectively. The stator current of the imaginary q-coordinate in the rotating rotor-flux reference frame is denoted by  $i_{sq}$ . It is assumed that the EM is operated in the base range such that the magnetic flux does not have to be weakened. Then the magnetic flux can be held constant in the motor control such that the motor torque is calculated by

$$T_m = k_T i_{sq}, \quad (5.3)$$

where  $k_T$  defines the motor torque constant in  $\text{N m A}^{-1}$ , i.e.

$$k_T = \frac{3}{2}p \frac{L_h}{L_r} \Psi_{rd}. \quad (5.4)$$

For the practical application of the presented state observers the accurate knowledge of the motor torque is of great importance, since an offset leads to deviations

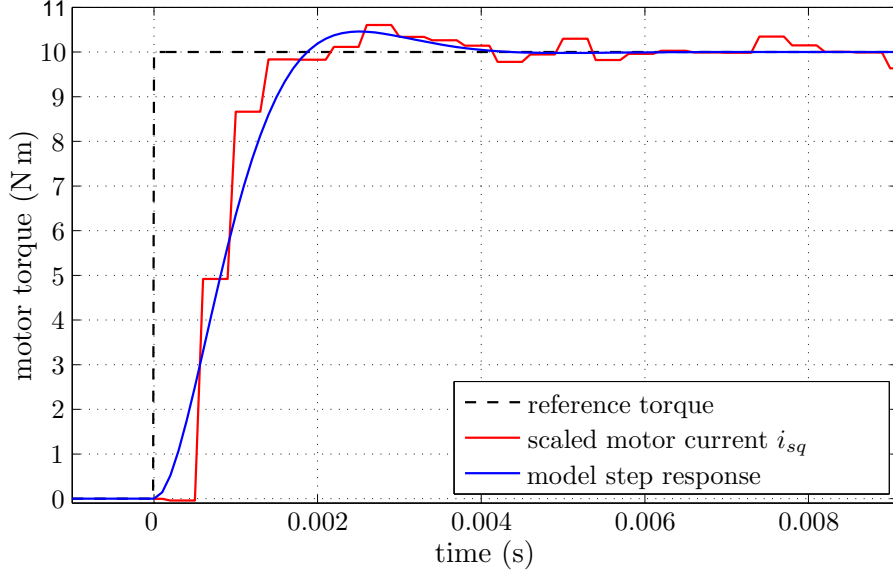


Figure 5.4: Step responses of the scaled motor current  $i_{sq}$  and the linear second order actuator model.

in the state estimation. Therefore also the losses due to the magnetization of the EM have to be considered. The magnetization losses depend on the rotation direction. They have been considered approximately such that the motor torque is calculated by

$$T_m = k_T i_{sq} - k_M \text{sat} \left( \frac{\omega_m}{\omega_{m,0}} \right), \quad (5.5)$$

where  $\omega_{m,0}$  corresponds to the saturation angular velocity. The motor torque constant  $k_T$ , the constant with respect to the magnetization losses  $k_M$  and  $\omega_{m,0}$  were identified experimentally. The constants  $k_M$  and  $\omega_{m,0}$  were approximately identified by a maneuver where the rotation direction changed. The constant  $k_T$  was approximately identified with the help of the torque measurement by the rotary encoders mounted at the torsion bar. The identification process was performed with the help of a maneuver of controlled constant shaft torque. Tab. C.12 shows the identified parameters and Fig. 5.10 shows an identification maneuver.

### 5.3.2 Linear model of the induction machine

The torque dynamics of the induction machine is approximated by the second order transfer function according to (2.13). Fig. 5.4 shows the step responses of the scaled current  $i_{s,q}$  of the EM and of the second order model. The torque-step maneuver was performed with a closed backlash gap from standstill. The parameters of the approximated transfer function are listed in Tab. C.13.

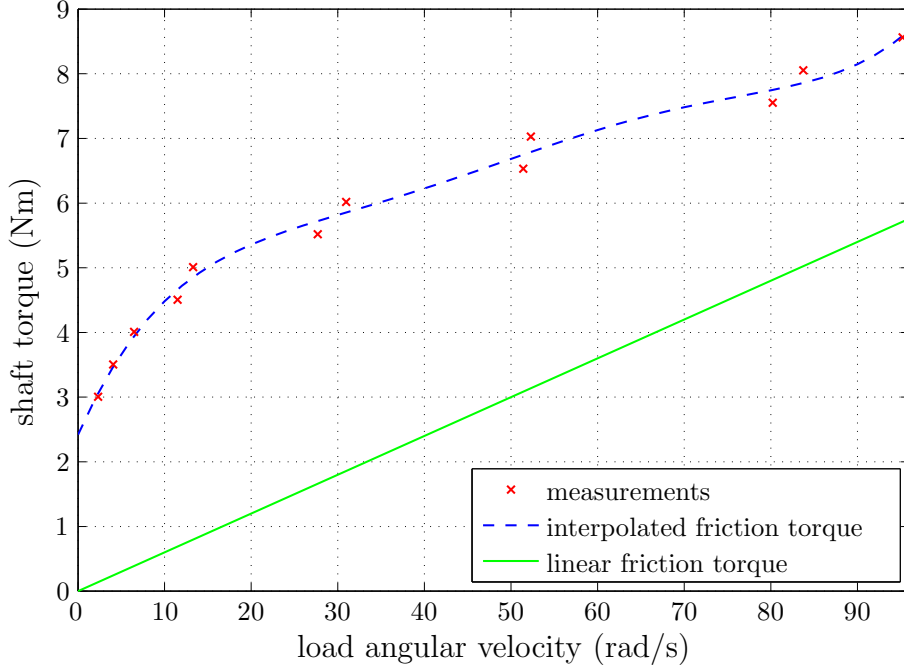


Figure 5.5: Speed dependent friction at steady state angular velocities and linear friction torque.

### 5.3.3 Rolling resistance

The rolling resistance or friction torque depends non-linear in the speed. Fig. 5.5 shows the friction values of different operating points. The friction torques correspond to the shaft torque values at the torsion bar at steady state load angular velocities. The measurements are interpolated by a fifth-order polynomial. Additionally the linear friction torque used in the synthesis model (2.42) is depicted.

### 5.3.4 Tire model

At the test bench a moped tire is used. Its parameters are shown in Tab. C.6. In this section the tire-slip characteristic, the tire radius  $r_{st}$  and the elasticity parameters of the tire are determined. According to (2.48) the longitudinal tire force corresponds to

$$F_x = \frac{\hat{T}_s - J_w \dot{\omega}_w}{r_{st}} - F_r(|\omega_w|) \operatorname{sgn}(\omega_w), \quad (5.6)$$

where  $\omega_w$  denotes the wheel angular velocity. The tire force in dependence of the wheel slip was determined experimentally. The measurements were performed at different reference shaft torques where the backlash gap was closed beforehand. The longitudinal tire slip was determined according to (2.20), where the velocity of the cylinder surface area corresponds to the vehicle's velocity, i.e.  $v_x = \omega_c r_c$ . Then the corresponding tire force was determined according to (5.6). Fig. 5.6

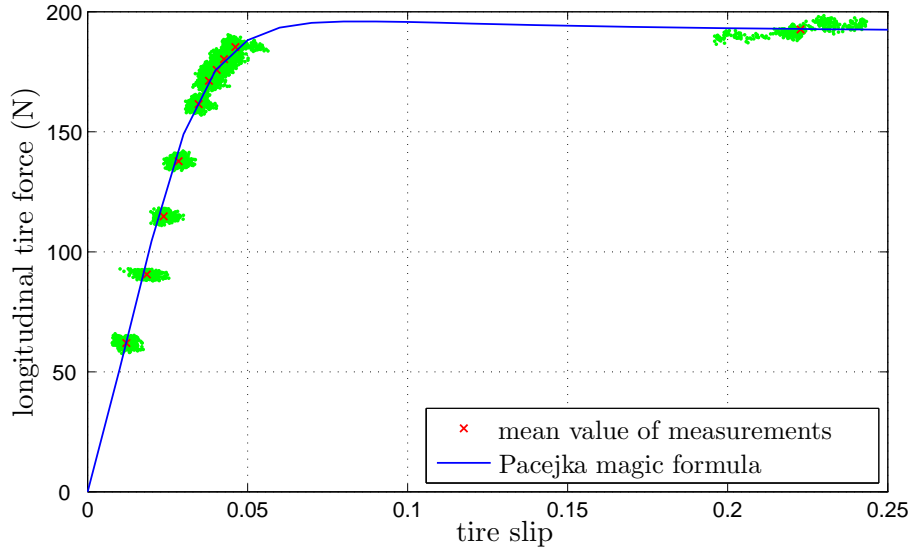


Figure 5.6: Longitudinal tire force versus wheel slip.

shows the longitudinal tire force in dependence the longitudinal wheel slip. The Pacejka tire model (2.22) was fitted to the mean values of the measurements. Tab. C.7 shows the parameters. The tire radius was estimated such that the straight line connecting the mean values of the tire forces in the linear region crosses the origin.

Since the stiffness of the torsion bar is known the tire elasticity and the damping coefficient were estimated by comparing the oscillation frequencies of the measured and simulated shaft torques. Tab. C.8 shows the identified parameters.

## 5.4 Test bench model

### 5.4.1 Model evaluation

The test bench model described in sections 2.6.2 - 2.6.5 has been implemented using Matlab/Simulink<sup>8</sup> as a three-mass system. The inertias of the wheel rim and the tire are shown in Tab. C.2. The inertia of the metal cylinder and its radius are shown in Tab. C.5. The shaft including the part of the clutch is modeled inertia-free due to the physical backlash model. The test bench model includes the rolling resistance and the Pacejka tire model which were identified in sections 5.3.3 and 5.3.4.

Fig. 5.7 compares the results of the simulation model with the test bench measurements at an acceleration maneuver. It shows the shaft torque and the angular velocities of the motor and the load. The load angular velocity corresponds to the angular velocity of the wheel rim  $\omega_r$ . The maneuver and the simulation were performed with a backlash gap at the beginning. For comparison reasons

<sup>8</sup>[www.mathworks.com](http://www.mathworks.com)

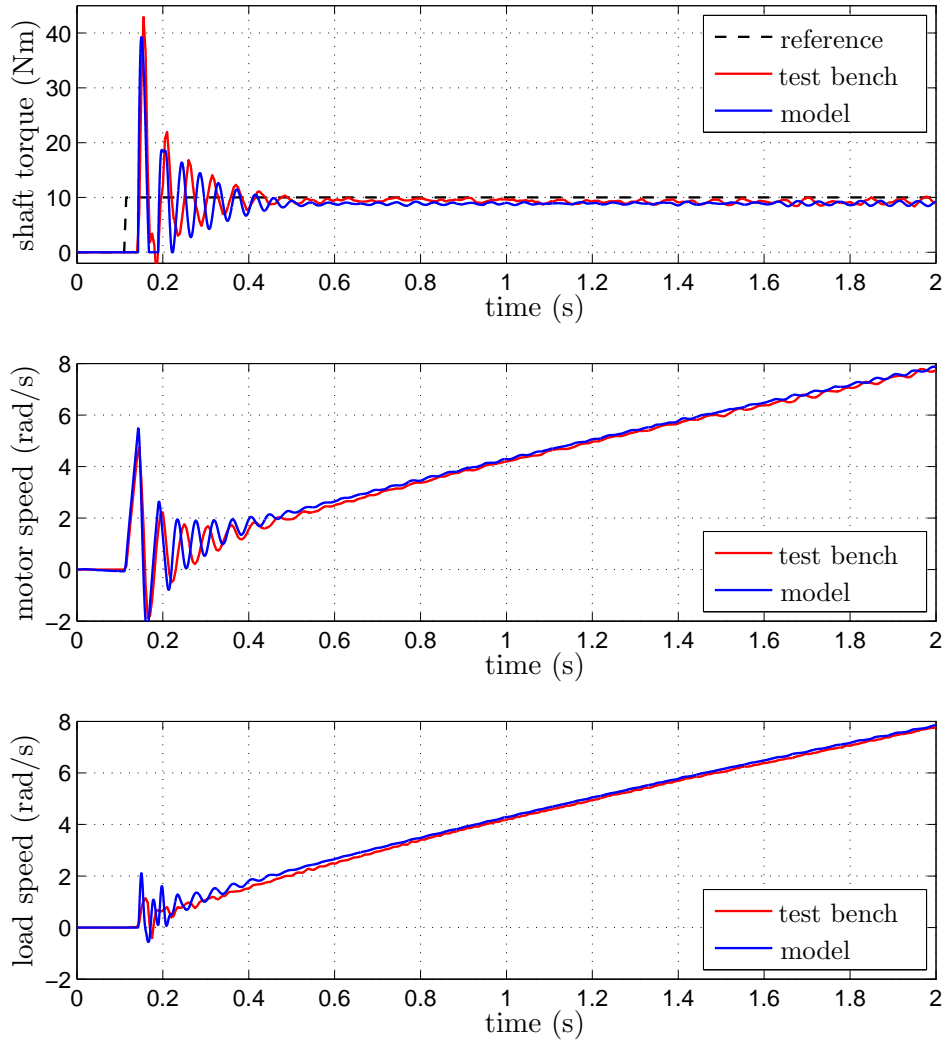


Figure 5.7: Evaluation of the test bench simulation model at an acceleration maneuver.

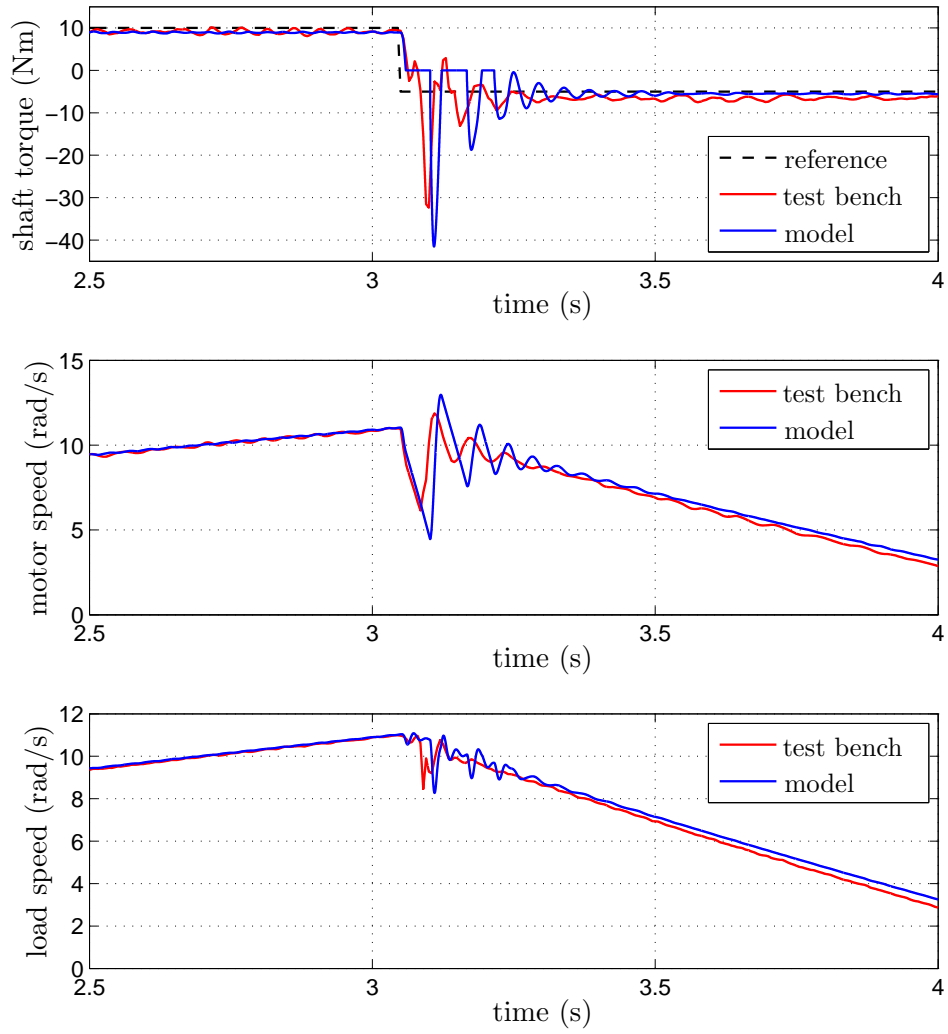


Figure 5.8: Evaluation of the test bench simulation model at a deceleration maneuver.

the measured motor torque estimate was used as input to the simulation. The oscillation frequency of the simulation model is higher than in the measurement because the simulation model assumes the all the test bench parts to be stiff except the torsion bar and the tire. Fig. 5.8 compares the results of the simulation model with the test bench measurements at deceleration. The reference torque changes from 10 N m to  $-5$  N m at about  $t = 3.1$  s. The test bench model is able to represent the dynamics of the test bench in the backlash and the contact phases. Deviations during the backlash transition result from the inertia-free modeling of the backlash dynamics.

### 5.4.2 Synthesis model

The stiffness of the torsion bar was determined by software, see section 5.1.3. The value of the damping coefficient  $d_s$  was determined approximately from the decay time of the torque oscillations of an open loop measurement. The inertia of the clutch was added to the motor inertia. The load inertia consists of the inertias of the wheel rim, the tire and the metal cylinder. Tab. C.3 shows the parameters of the linear synthesis model (2.42).

## 5.5 Concept implementation

The observer and controller concepts have been implemented in C into the FOC software of the ACOPOS servo drive. Only the header files and current controller routine are available as source code. This means that only the current  $i_{sq}$  can be modified by the controller. The sampling time of the current controller routine corresponds to 100  $\mu$ s. It is defined by the predefined switching frequency of the servo drive. Because of the small sampling time and the limited computing power of the ACOPOS processor only a few floating-point multiplication instructions can be added to the existing source code. The angular encoder values are read by the ACOPOS software every 400  $\mu$ s. This requires that the encoder angular velocity signals have to be filtered due to the small sampling time of the current controller routine. This has been accomplished by a first-order low-pass filter with time constant  $\tau_f = 333$   $\mu$ s. The ACOPOS SW is controlled by setting or reading so-called *parameter identifier* variables via an Ethernet network. User defined parameter identifiers have been assigned to the corresponding variables of the concept. Batch scripts have been written for measurement. The measurement memory is very limited. It involves a maximum of ten variables for a measurement length of about 5 s.

For the predefined constants of the controllers and the observers the code of the corresponding C-defines has been generated by a Matlab script such that parameter changes can be performed quickly in the software. The implementation of the concepts itself was done in a two step process. First the Simulink models were implemented into a Matlab function and compared with each other. Then the Matlab code was ported into C.

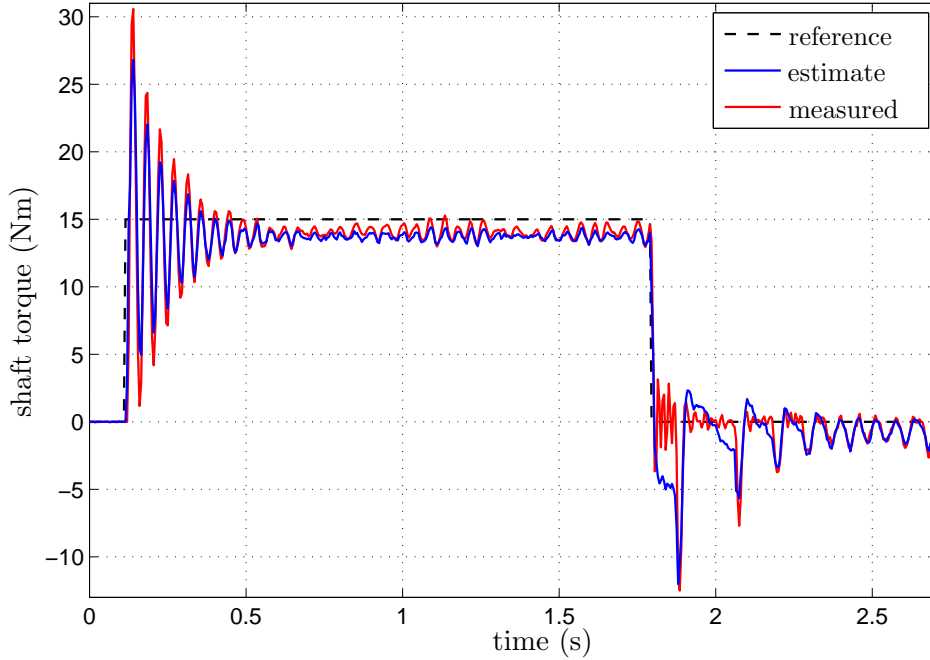


Figure 5.9: Observer of section 3.2.3 using non-delayed measurement signals at a torque step and subsequent step to zero.

For the implementation of the observer of section 3.2.2 the filtered load angular velocity signal has been artificially delayed by 2 ms with the help of a ring buffer. Then the delayed value has been sampled every 5 ms using a counter. This implements the delay and the limited update rate, for example, of a bus system. *Euler* integrators have been implemented for the observer concepts.

The rotor-flux of the electric motor is held constant during the experiments by the FOC, see Tab. C.9 where the value of the predefined magnetization current is given.

## 5.6 Experiments

### 5.6.1 First order SMC concepts

#### Measurement of load angular velocity without delay

At first, it is assumed that the load angular velocity can be measured without any delay. Since the observer forms the basis of the control concept it is parameterized and analyzed first. This involves the parameterization of the gains  $M_i$ ,  $i = 1, 2$  of (3.21) and the widths of the saturation functions  $\varepsilon_{o,i}$ ,  $i = 1, 2$ , see (3.26), by verifying the estimates with respect to the measured states. Initial values were determined with the help of the test-bench simulation model described in section 2.6. Since the encoder values are read every  $400 \mu\text{s}$  the widths of the saturation functions  $\varepsilon_{o,i}$  were chosen such that the measured states are filtered

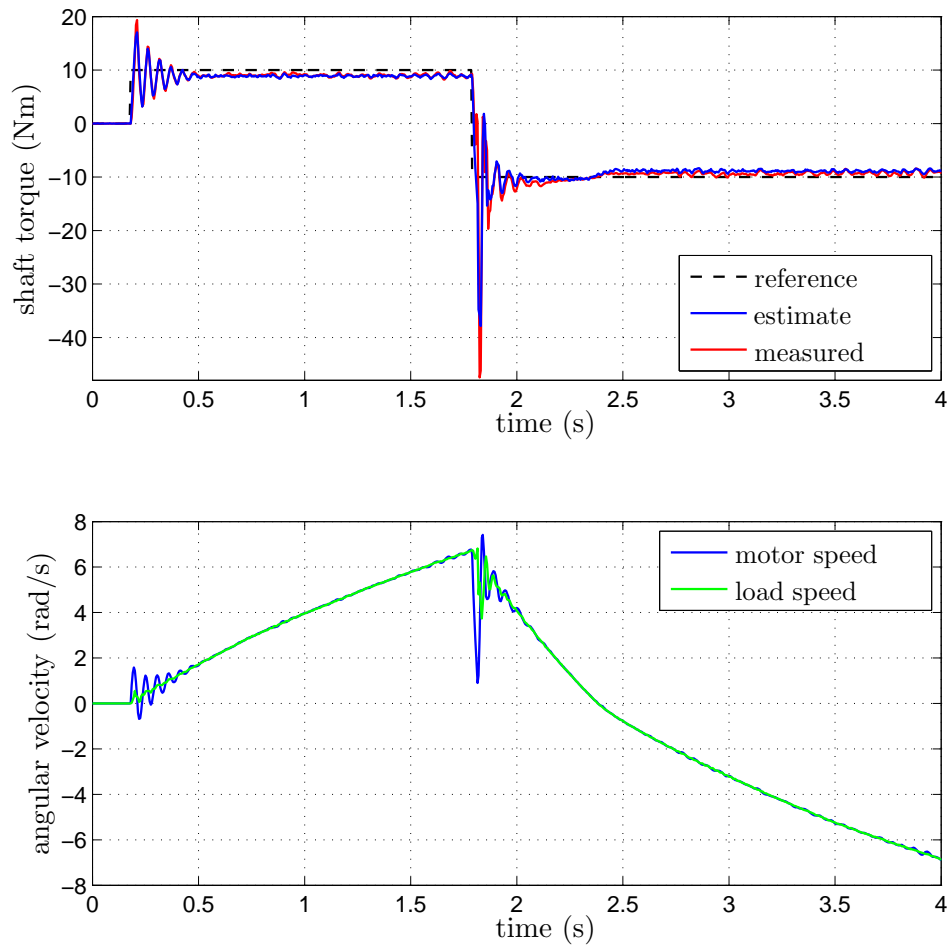


Figure 5.10: Observer of section 3.2.3 at a positive and negative torque step maneuver.

and chattering is reduced. Subsequently the observer gain matrix (3.44) was parameterized. Tab. 5.1 shows the parameters, where  $\sigma(\cdot)$  denotes the spectrum of a matrix.

Fig. 5.9 shows the performance of the observer of section 3.2.3. It depicts the reference torque, the torque estimate at the torsion bar and the torque which results from the measured difference angle at the torsion bar. The initial backlash gap was closed manually. Due to the torque step low-damped oscillations are enforced. The remaining oscillations at the constant torque of 15 Nm result due slight axial misalignments of the test bench construction. After setting the reference torque to zero torque oscillations arise due to the backlash. It can be seen that the estimated torque does not exactly correspond to the real measured torque during the backlash phase. This results from the linear observer synthesis model (2.42). In the backlash phase the torque measurement signal also oscillates. This is due to the inertia of the coupling part connected to the torsion bar. But in the contact phase the shaft torque is estimated sufficiently accurate independently of the backlash width. During the backlash phase the torque estimate remains small.

Fig. 5.10 shows the observer performance at a positive and subsequent negative torque step maneuver. It can be seen that after the backlash transition a large torque overshoot occurs which is also reflected by the observer's estimate. Additionally, when the direction of the angular velocities becomes negative, the absolute torque value reduces whereas the the reference is constant. According to the second equation of (2.48) this is effected by the motor torque. The motor torque is calculated according to (5.5) considering the magnetization losses.

The implementation of the control law, see (4.7) and (4.8), requires the estimated state variables of the observer. Also the measured state variables are provided by the observer. Due to the filtering property high frequency components are attenuated in the measured signals. From the reference torque a reference torsion angle  $\phi_{\text{ref}}$  is calculated according to (4.2). The reference torsion angle has been also filtered by a first-order low-pass filter with time constant  $\tau_r = 2.5$  ms. Due to computational reasons the time derivative terms in the equivalent control (4.8) have been neglected in the implementation.

The determination of the control gain  $K$  is done according to (4.12) and experimentally. It is assumed that the load torque error is sufficiently small such that it is neglected. It is further assumed that the absolute maximum acceleration of the load corresponds to  $|\dot{\omega}_l|_{\text{max}} = 100 \text{ rad s}^{-2}$  and that the term  $\delta J_l / \hat{J}_l \leq 0.25$ . Then according to (4.12) the control gain has to be chosen as  $K > 25$ . For the practical implementation a saturation function has been chosen to reduce chattering. The control gain  $K$  has to be chosen such that the system is also stable within the boundary layer. According to section 4.1.3 the parameter  $\lambda$ , the gain  $K$  and the boundary layer width  $\varepsilon_c$  have to be designed such that the system remains stable., i.e. the denominator of (4.24) has zeros in the open left complex half-plane. With the identified parameters of the test-bench and the IM, see Tab. C.3 and Tab. C.13, and the chosen parameters for  $\lambda$  and  $\varepsilon_c$ , the

Table 5.1: Observer Parameters for load angular velocity without delay.

Parameter	Value
$M_1, M_2$	1200
$\epsilon_{o,1}, \epsilon_{o,2}$	0.9
$\sigma(\mathbf{A}_{11} + \mathbf{L}\mathbf{A}_{21})$	$\{-400, -400\}$

Table 5.2: Controller parameters for load angular velocity without delay.

Parameter	Value
$K$	120
$\epsilon_c$	0.4
$\lambda$	200

upper bound of the gain has to satisfy  $K < 127.5$ . Tab. 5.2 shows the controller parameters which were tuned experimentally.

Fig. 5.11 shows the reference, the estimated and the measured shaft torque. Additionally the motor and load angular velocities and the load torque are depicted. The test-bench was accelerated from standstill by applying a constant reference shaft torque of 30 N m. Immediately after the backlash gap is closed the shaft torque tracks the reference. There are no visible torque overshoots at the backlash-contact transition and when the shaft torque reaches the reference.

After a short acceleration period the reference torque changes to  $-15$  N m which corresponds to an energy regeneration maneuver. Again there is no visible torque overshoot and torque oscillations can be completely avoided. During the deceleration phase there is a very small deviation of the estimated shaft torque from the measured one. Due to the large rolling resistance compared to the reference torque, see Fig. 5.5, the value of the load inertia changes. This yields a load torque estimation error and a small control error according to (4.19). The load torque estimate is noisy due to the chosen eigenvalue, see Tab 5.1. Peaks at the backlash-contact and contact-backlash transitions can be seen. The reason is that the error dynamics is not differentiable at these transitions, see (B.9).

### Delayed and sampled load angular velocity

Due to the delayed and sampled load angular velocity the observer design is a two-step process as described in section 3.2.3. The observer parameters were determined with the help of the simulation model and were tuned experimentally afterwards. First the eigenvalues of the matrix  $\mathbf{A}_0$  were chosen such that they all have the same real part  $-\lambda_0$ . In the second step the eigenvalues of  $\mathbf{A}_0 + \mathbf{A}_1$  were shifted to the left in the complex plane. Again, all the real parts were chosen identical at  $-\tilde{\lambda}_0$ . The choice of  $-\tilde{\lambda}_0$  was performed with the help of Fig. 3.4 which depicts the decay rate of the observer error dynamics (3.36). The goal was to in-

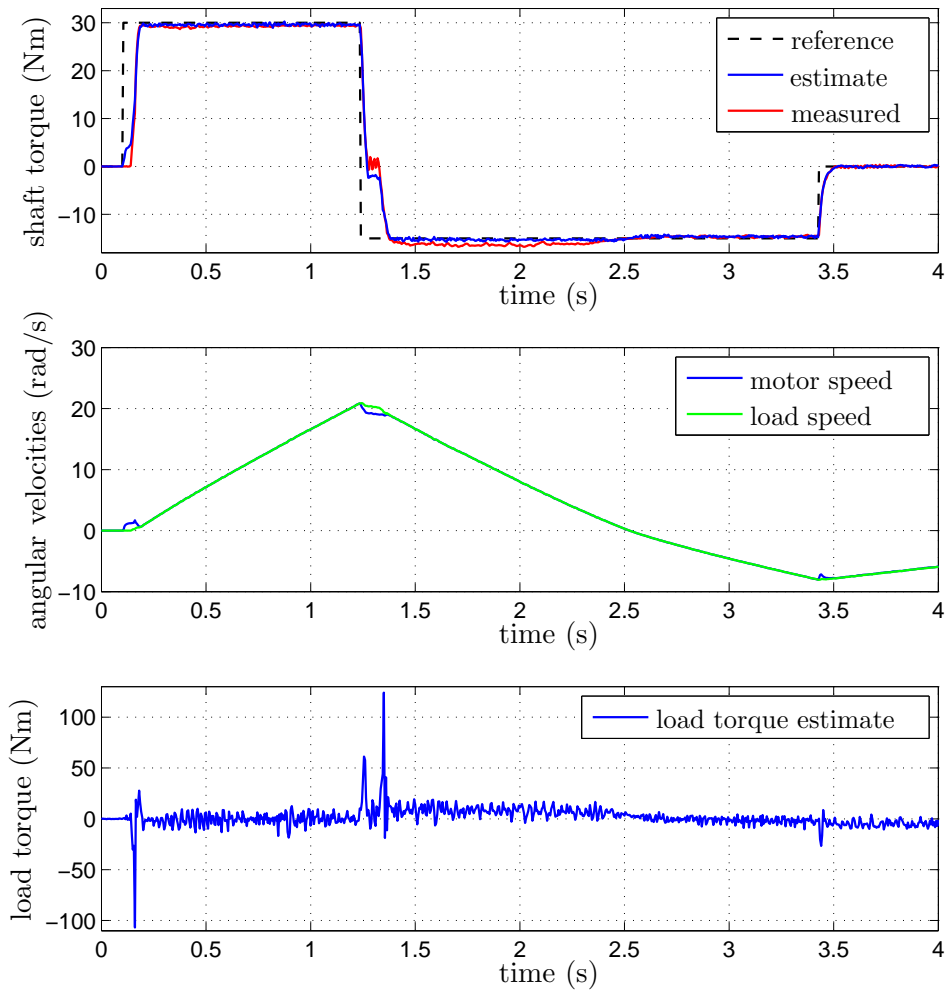


Figure 5.11: Reference and controlled shaft torque based on the observer of section 3.2.1 using non-delayed measurement signals.

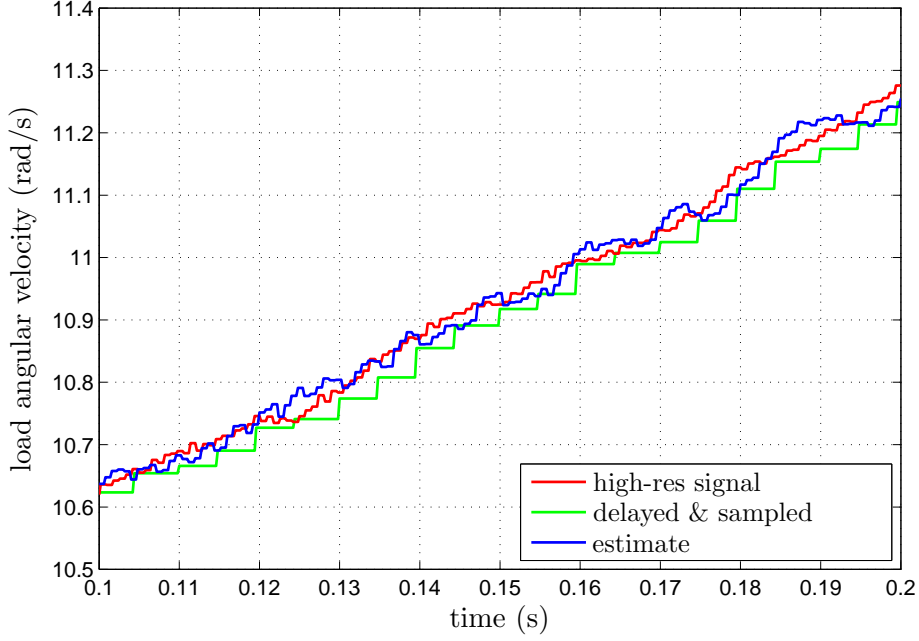


Figure 5.12: Comparison of the high-resolution, the measured and the estimated load angular velocity signal in the contact phase.

crease the decay rate. Fig. 3.5 depicts the value  $\iota$  which is a measure for the estimation error of the load angular velocity signal in the backlash phase. From experiments it was found that it is necessary for a satisfactorily closed-loop control behavior that

$$\iota < 0.7. \quad (5.7)$$

For larger values of  $\iota$  there is a torque overshoot at the backlash-contact transitions. This requires that the real parts of the eigenvalues of  $\mathbf{A}_0 + \mathbf{A}_1$  have to be placed at about  $-190$ , see Fig. 3.4. Tab. 5.3 shows the observer parameters where  $\sigma(\cdot)$  denotes the spectrum of a matrix. The observer gains are

$$\mathbf{l}_1 = \begin{bmatrix} 0.141 \\ 0.024 \\ -4.093 \end{bmatrix}, \quad \mathbf{l}_2 = \begin{bmatrix} 5.046 \\ 0.242 \\ -90.9 \end{bmatrix}. \quad (5.8)$$

From the delayed and sampled measurement of the load angular velocity the high-resolution signal is estimated without any delay. Fig. 5.12 shows the high-resolution, the delayed and sampled and the estimated load angular velocity signal in the contact phase. The delayed and sampled signal is generated from the high-resolution signal. Noise in the high-resolution signal deteriorates the estimate since it corresponds to a constant disturbance of the sampled signal such that there are small deviations in the estimate of the angular velocity signal.

Table 5.3: Parameters for the observer using the delayed and sampled load angular velocity measurement.

Parameter	Value
$M$	1400
$\epsilon_o$	1.0
$\sigma(\mathbf{A}_0)$	$\{-170, -170 + 68j, -170 - 68j\}$
$\sigma(\mathbf{A}_0 + \mathbf{A}_1)$	$\{-190, -190 + 76j, -190 - 76j\}$

Table 5.4: Controller parameters based on the observer using the delayed and sampled load angular velocity measurement.

Parameter	Value
$K$	140
$\epsilon_c$	0.7
$\lambda$	110

Tab. 5.4 shows the parameters of the implemented first order sliding mode control concept. Compared to the concept without delay the parameter  $\lambda$  has to be significantly decreased because of the reduced decay rate of the observer error dynamics.

Fig. 5.13 shows the reference, measured and estimated shaft torque, the motor and the load angular velocity and the load torque estimate. There is no torque overshoot at the backlash-contact transitions. There is a small overshoot when the reference torque is reached. This results from the erroneous load torque estimate in the backlash phase, see (B.24). The backlash is transitioned faster compared to the concept of the previous section. The steady state control error because of the controller parameters  $\lambda$  and  $\epsilon_c$ . Due to the fact that the observer incorporates the delayed and sampled measurement the control performance is nearly as good as the concept with measurements without any delay and sampling.

For comparison reasons Fig. 5.14 shows the control performance torque when the load angular velocity signal is not available for measurement at all. This was implemented by setting the observer gain  $\mathbf{I}_2$  to zero. Since no information of the load side is available, the backlash-contact transition is performed non-smooth although the mean difference angular velocity  $\bar{\omega}$  is small in the backlash phase. A large torque overshoot appears which could harm mechanical parts. In the contact phase the load angular velocity becomes observable and the concept tracks the reference. When the reference torque is set to zero multiple non-smooth backlash-contact transitions arise.

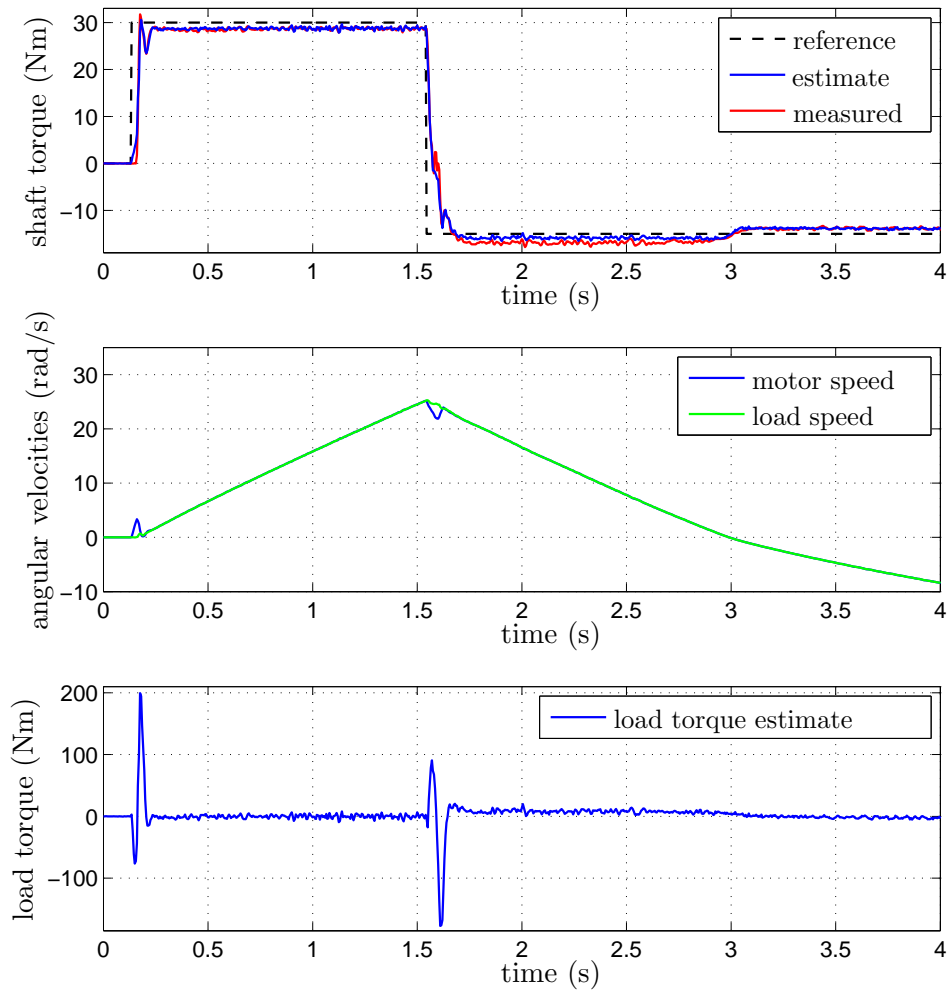


Figure 5.13: Reference and controlled shaft torque based on the observer using the delayed and sampled load angular velocity measurement.

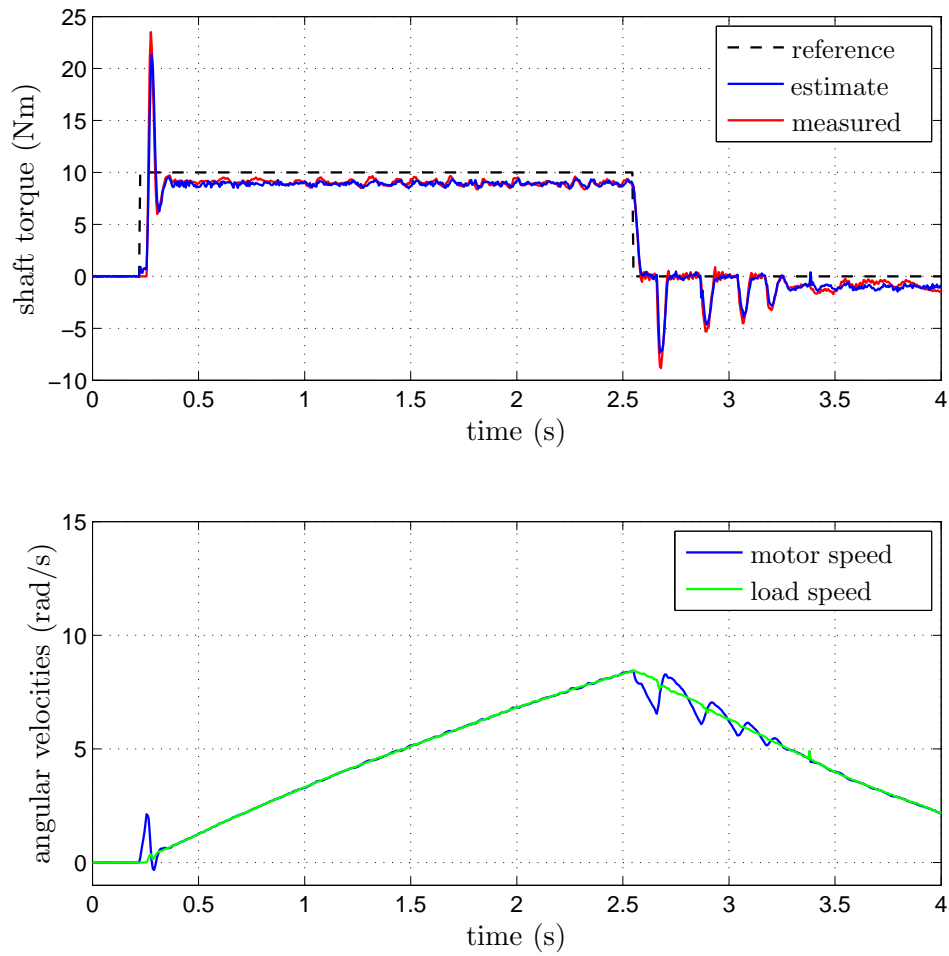


Figure 5.14: Controlled shaft torque using only the motor angular velocity signal as measurement.

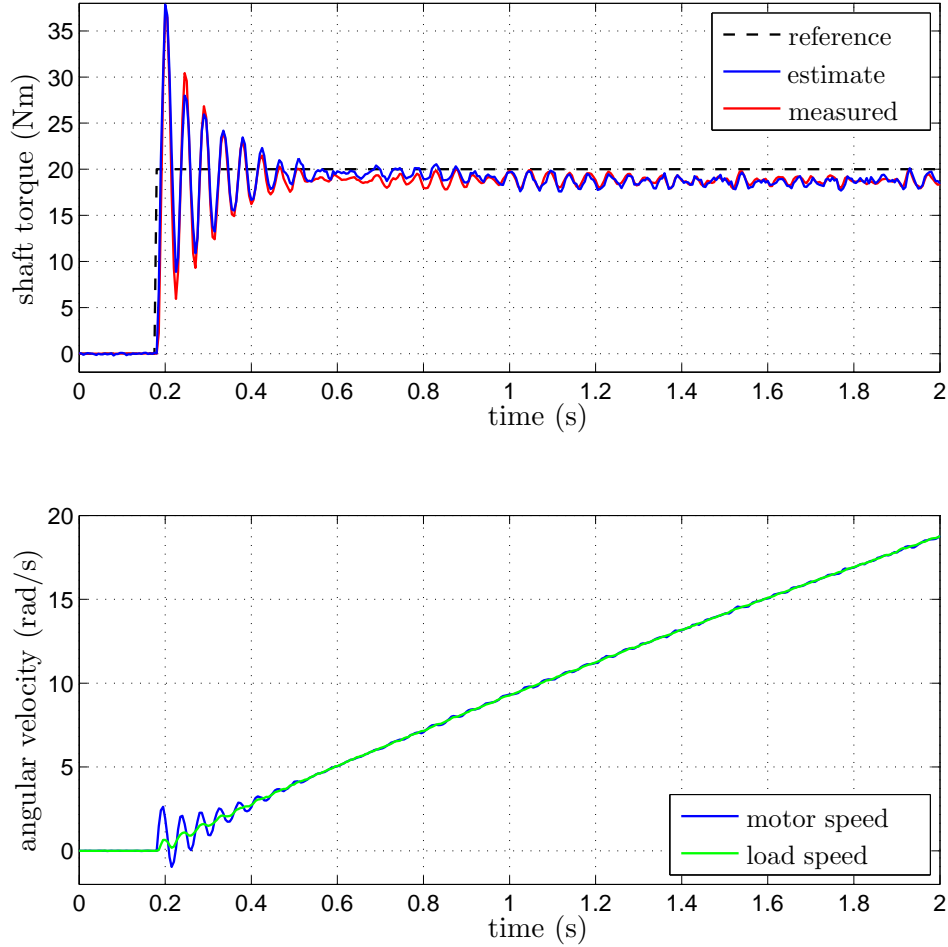


Figure 5.15: Reference and controlled shaft torque based on the second-order step-by-step observer.

### 5.6.2 Higher-order based concepts

The second-order sliding mode observer of section 3.3.2 was implemented in the current controller C-file of the ACOPOS SW. Since the square-root operations of the super-twisting algorithm are time consuming the switching frequency of the servo drive had to be set to 5 kHz.

According to section 3.3.2 the Lipschitz constants were determined with the help of the simulation model. The maximum absolute value of the derivative of the transformed third state variable was set to  $|\dot{z}_3|_{\max} = 8000$ . The maximum absolute value of the load torque derivative is assumed not to exceed the maximum absolute value of the shaft torque derivative. Then the Lipschitz constants correspond to  $L_1 = 8000$ ,  $L_2 = 8000$  and  $L_3 = 100\,000$ . The observer gains are calculated according to (3.63) and adapted slightly experimentally. The parameters are shown in Tab. 5.5. The parameter  $E_3$  was always set to 1 since all the state variables are zero initially.

Table 5.5: Observer gains of the second-order step-by-step observer.

Parameter	Value
$\kappa_{1,1}$	583.27
$\kappa_{2,1}$	8800
$\kappa_{1,2}$	583.27
$\kappa_{2,2}$	8800
$\kappa_{1,3}$	1944.22
$\kappa_{2,3}$	110 000

Table 5.6: Controller parameters of the GSOA.

Parameter	Value
$k_1$	90
$k_2$	30
$p$	0.75
$\lambda$	200

Fig. 5.15 shows the measured and estimated shaft torque and the motor and load angular velocity signals. It can be seen that the estimate nearly perfectly matches the measurement.

The determination of the control parameters  $k_1$  and  $k_2$  according to the sector conditions, see (4.41), allows finite time convergence to the origin  $\sigma = \mathbf{0}$  but leads to large control parameters, especially to that of  $k_2$ . This leads to chattering because of the actuator dynamics which is not considered in the design. Therefore the gains were determined experimentally such that the high-frequency control is sufficiently mitigated. Due to the reduced control gains only practical stability can be achieved, see section 4.4. The exponent in (4.42) was chosen as  $p = 0.75$  such that it can be computed by two successive square root operations. Tab. 5.6 shows the parameters of the GSOA.

Fig. 5.16 shows the controlled test-bench shaft torque, the measured torque and the angular velocities. The state variables were estimated by the second-order step-by-step observer of section 3.3.2. The load torque estimate of the observer according to (3.77) is not used in the equivalent control term because it is very noisy. Since the control algorithm (4.42) is continuous no additional chattering reduction methods are necessary. Again, the controller tracks well the reference torque and the backlash-contact transitions are performed without torque overshoot.

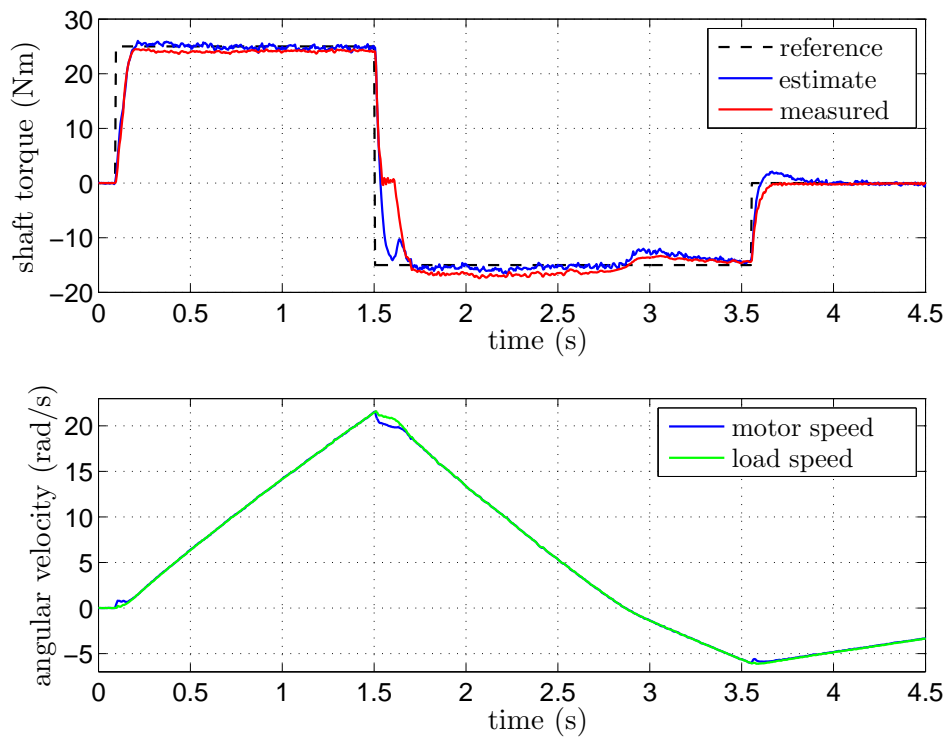


Figure 5.16: Reference and controlled shaft torque based on the observer of Section 3.3.

# Chapter 6

## Summary and Outlook

In this thesis a new sliding mode power-train control concept for electric vehicles was developed for tracking a given reference torque such that power-train oscillations are prevented. The advantage of this concept is that it does not require any torque sensor information and it copes with unknown backlash and the wheel speed information from the vehicle's bus system.

The concept is based on a state observer which estimates the shaft and load torque at the power-train. The observer was designed by means of sliding mode concepts. For the synthesis of the controller and the state observer a linear two-mass system model of the power-train was derived. The observer based on the linear synthesis model is able to estimate the shaft torque despite of unknown backlash width.

The observer requires the motor and the wheel angular velocity signals for measurement. The information of the wheel speed sensors is available on the vehicle's bus system but its update rate is not sufficient for a proper function of the controller. Therefore the sliding mode observer was extended for the use of delayed and sampled signal measurements.

Based on the presented observer a first-order sliding mode controller was designed and an appropriate chattering reduction method was applied. The bounds of the control gain were determined with respect to the disturbance and the second-order actuator dynamics. The behavior of the control concept in the backlash phase was described in dependence of the control parameters. The proposed concept was verified by means of a multi-body system simulation of the electrical rear axle of a prototype vehicle. The simulation model includes a wheel speed sensor model and a simple bus model. It was shown that the power-train oscillations were prevented with the presented control concept.

For comparison reasons a second-order sliding mode step-by-step observer for the power-train was designed. It has a smaller estimation error. Additionally a controller based on the so-called generic second order algorithm was designed.

In order to investigate the performance of the observer and controller concepts a test-bench was designed. A three-mass system model of the test-bench including the tire elasticity, the tire slip, the rolling resistance and a physical backlash model was designed and parameterized. The control concepts were implemented at the

servo drive in addition to the field-oriented control of the electric machine.

The first-order sliding mode concepts are preferred due to the very limited computational power of the servo drive processor. The developed concepts track the reference torque in the contact phase. The backlash-contact transition is performed without any noticeable torque overshoot. The control concept based on the observer with delayed and sampled measurement of the wheel speed information performs nearly as good as the control concept based on measurements without delay.

The presented results form the basis for future research in the field of power-train control and reduction of torque oscillations. The proposed concepts are not limited to power-train control. They can be applied to applications in the field of mechanical engineering where torque oscillations must be prevented.

# Appendix A

## Stability of Linear Sampled Data Systems

Consider the linear, continuous-time system

$$\dot{\mathbf{x}} = \mathbf{A}_0\mathbf{x} + \mathbf{A}_1\mathbf{x}(t - \tau(t)), \quad (\text{A.1})$$

where  $\tau(t)$  is a time-varying delay with the initial condition  $\mathbf{x}(\nu) = \phi(\nu)$ , for  $-\tau_m \leq \nu \leq 0$ . A basic method for the determination of the stability of (A.1) is the *Razumikhin Theorem* [GKC03, Fri14]. Assume  $V = \mathbf{x}^T\mathbf{P}\mathbf{x}$  positive definite.

The system (A.1) is asymptotically stable if

$$\dot{V} < 0, \quad \text{if } V(t + \psi) < pV(t), \quad p > 1, \quad \forall \psi \in [-\tau_m, 0]. \quad (\text{A.2})$$

This leads to the following linear matrix inequality (LMI), i.e.

$$\begin{bmatrix} \mathbf{A}_0^T\mathbf{P} + \mathbf{P}\mathbf{A}_0^T + q\mathbf{P} & \mathbf{P}\mathbf{A}_1 \\ \mathbf{A}_1^T\mathbf{P} & -q\mathbf{P} \end{bmatrix} \prec 0. \quad (\text{A.3})$$

The LMI (A.3) does not depend on the delay or on its derivative such that it can be applied for sampled data systems. The drawback of this method is that it leads to conservative results.

Less conservative stability criteria for the stability of linear sampled data systems are given in [Fri14]. In [LF12, Fri14] a method for sampled data systems with additional constant delay were published. The method is based on a discontinuous Lyapunov-Krasovskii functional which also results in solving an LMI. The functional consists of a nominal and a discontinuous term  $V = V_n + V_w$ , i.e.

$$\begin{aligned} V_n &= \mathbf{x}^T\mathbf{P}\mathbf{x} + \int_{t-\tau_0}^t \mathbf{x}^T(s)\mathbf{R}_1\mathbf{x}(s)ds + \tau_0 \int_{-\tau_0}^0 \int_{t+\nu}^t \dot{\mathbf{x}}^T(s)\mathbf{R}_2\dot{\mathbf{x}}(s)dsd\nu, \\ V_w &= (\tau_m - \tau_0)^2 \int_{t_k - \tau_0}^t \dot{\mathbf{x}}^T(s)\mathbf{W}\dot{\mathbf{x}}(s)ds \\ &\quad - \frac{\pi^2}{4} \int_{t_k - \tau_0}^{t - \tau_0} (\mathbf{x}(s) - \mathbf{x}(t_k - \tau_0))^T \mathbf{W} (\mathbf{x}(s) - \mathbf{x}(t_k - \tau_0)) ds, \end{aligned} \quad (\text{A.4})$$

where  $\mathbf{P}$ ,  $\mathbf{W}$ ,  $\mathbf{R}_1$ ,  $\mathbf{R}_2$  are symmetric, positive definite matrices. For  $t = t_k$   $V_w = 0$  because the integration interval is zero. Additionally, in the last term of (A.4) the expression  $(\mathbf{x}(s) - \mathbf{x}(t_k - \tau_0))$  is zero for  $s = t_k - \tau_0$ . In the derivative of (A.4) the the so-called *Jensen* and *Wirtinger* inequality are used for the derivation of the LMI criterion (3.38). The derivation is outlined in [LF12].

# Appendix B

## Observer and Controller Analysis

### B.1 Observer analysis with respect to unknown backlash width

The error dynamics of the presented observers of sections 3.2.1 and 3.2.2 is analyzed for the contact and backlash phase. In the analysis the backlash width corresponding to the angle  $2\alpha$  is assumed to be unknown.

#### B.1.1 Measurements without delay

In this section the error dynamics of observer (3.21) applied to the model (2.39) is analyzed. In the observer design of section 3.2.3 the synthesis model is augmented by the disturbance model (3.43) in order to estimate the unknown input. To express the observer error dynamics conveniently, the model (2.39) is also augmented by the disturbance model. With the state transformation (3.19) the augmented power-train model is

$$\begin{aligned} \begin{bmatrix} \dot{\mathbf{x}}_1 \\ \dot{\mathbf{y}} \end{bmatrix} &= \begin{bmatrix} \mathbf{A}_{11} & \mathbf{A}_{12} \\ \mathbf{A}_{21} & \mathbf{A}_{22} \end{bmatrix} \begin{bmatrix} \mathbf{x}_1 \\ \mathbf{y} \end{bmatrix} + \begin{bmatrix} \mathbf{b}_1 \\ \mathbf{b}_2 \end{bmatrix} u + \begin{bmatrix} \mathbf{g}_1 \\ \mathbf{g}_2 \end{bmatrix} \xi(\theta), \\ \mathbf{g}_2 &= \begin{bmatrix} -\frac{k_s}{J_l} \\ \frac{k_s}{k_g J_m} \end{bmatrix}, \end{aligned} \tag{B.1}$$

where  $\mathbf{g}_1 = \mathbf{0}$ . The vector of the non-measured states in (B.1) corresponds to

$$\mathbf{x}_1 = \begin{bmatrix} q \\ \theta \end{bmatrix}, \tag{B.2}$$

where  $\theta$  denotes the total angle of deflection including backlash according to (2.23). In the observer design the state variable corresponding to the torsion angle  $\varphi$  is introduced instead of  $\theta$ , since observer (3.21) applies for LTI systems.

It is assumed that the elements of the diagonal matrix  $\mathbf{M}$  of the observer (3.21) are sufficiently large such that sliding mode is enforced. Subtracting the second

equation of (B.1) from the second equation of (3.21) yields the error dynamics of the measured states, i.e.

$$\dot{\mathbf{e}}_y = \mathbf{A}_{21}\mathbf{e}_{x_1} + \mathbf{A}_{22}\mathbf{e}_y - \mathbf{g}_2\xi(\theta) - \mathbf{v}, \quad (\text{B.3})$$

where

$$\mathbf{e}_y = \hat{\mathbf{y}} - \mathbf{y}. \quad (\text{B.4})$$

In sliding mode the error vanishes, i.e.  $\mathbf{e}_y \equiv \mathbf{0}$ . With the help of the equivalent control method  $\dot{\mathbf{e}}_y = \mathbf{0}$ . Then the discontinuous term  $\mathbf{v}$  in (B.3) can be expressed by

$$\mathbf{v}_{eq} = \mathbf{A}_{21}\mathbf{e}_{x_1} - \mathbf{g}_2\xi(\theta). \quad (\text{B.5})$$

Substituting (B.5) into the error dynamics of

$$\mathbf{e}_{x_1} = \hat{\mathbf{x}}_1 - \mathbf{x}_1 \quad (\text{B.6})$$

yields

$$\dot{\mathbf{e}}_{x_1} = \mathbf{L}\mathbf{A}_{21}\mathbf{e}_{x_1} - \mathbf{L}\mathbf{g}_2\xi(\theta). \quad (\text{B.7})$$

With (2.37) the error vector with respect to the non-measured states can be defined as

$$\begin{aligned} \mathbf{e} &= \frac{1}{k_s} \begin{bmatrix} \hat{T}_l - T_l \\ \hat{T}_s - T_s \end{bmatrix} = \begin{bmatrix} \hat{q} - q \\ \hat{\varphi} - (\theta - \xi(\theta)) \end{bmatrix} = \\ &= \mathbf{e}_{x_1} + \mathbf{h}_2\xi(\theta), \end{aligned} \quad (\text{B.8})$$

where  $\mathbf{h}_i \in \mathbb{R}^2$  denotes the  $i$ -th unit vector. With

$$\dot{\mathbf{e}} = \dot{\mathbf{e}}_{x_1} + \mathbf{h}_2\frac{d\xi}{d\theta}\dot{\theta} \quad (\text{B.9})$$

the error dynamics of (B.7) in terms of the error vector  $\mathbf{e}$  is

$$\dot{\mathbf{e}} = \mathbf{L}\mathbf{A}_{21}(\mathbf{e} - \mathbf{h}_2\xi(\theta)) - \mathbf{L}\mathbf{g}_2\xi(\theta) + \mathbf{h}_2\frac{d\xi}{d\theta}\dot{\theta}. \quad (\text{B.10})$$

According to (2.39) the vector  $\mathbf{g}_2$  corresponds to the negative second column of  $\mathbf{A}_{21}$ , i.e.  $\mathbf{g}_2 = -\mathbf{A}_{21}\mathbf{h}_2$ , such that the terms corresponding to  $\xi(\theta)$  cancel out. In the contact phase  $d\xi/d\theta$  vanishes such that

$$\dot{\mathbf{e}} = \mathbf{L}\mathbf{A}_{21}\mathbf{e} = \text{diag}\{-\lambda_1, -\lambda_2\}\mathbf{e}. \quad (\text{B.11})$$

This means that the observer error exponentially decays to zero if unknown backlash is present in the power train. In the backlash phase  $d\xi/d\theta = 1$  such that

$$\begin{aligned} \dot{\mathbf{e}} &= \mathbf{L}\mathbf{A}_{21}\mathbf{e} + \mathbf{h}_2\dot{\theta} \\ &= \text{diag}\{-\lambda_1, -\lambda_2\}\mathbf{e} + \mathbf{h}_2\left(\frac{\omega_m}{k_g} - \omega_l\right). \end{aligned} \quad (\text{B.12})$$

This means that  $\hat{\varphi}$  corresponds to the output of a first order low-pass filter with time constant  $1/\lambda_2$ , i.e.

$$\hat{\varphi} = \frac{1}{\lambda_2} \left( \frac{\omega_m}{k_g} - \omega_l \right)_f. \quad (\text{B.13})$$

The load torque error vanishes also in backlash phase, since  $\dot{e}_q = -\lambda_1 e_q$ .

## B.1.2 Delayed and sampled load speed measurement

Applying the state transformation (3.19) to the power train model (2.39) yields

$$\begin{aligned} \begin{bmatrix} \dot{\mathbf{z}} \\ \dot{y}_1 \end{bmatrix} &= \begin{bmatrix} \mathbf{A}_{11} & \mathbf{a}_{12} \\ \mathbf{a}_{21}^T & a_{22} \end{bmatrix} \begin{bmatrix} \mathbf{z} \\ y_1 \end{bmatrix} + \begin{bmatrix} \mathbf{b}_1 \\ b_2 \end{bmatrix} u + \begin{bmatrix} \mathbf{g}_1 \\ g_2 \end{bmatrix} \xi(\theta) \\ \mathbf{g}_1 &= \begin{bmatrix} 0 \\ 0 \\ -k_s/J_l \end{bmatrix}, \quad g_2 = \frac{k_s}{k_g J_m}. \end{aligned} \quad (\text{B.14})$$

The vector of the non-measured states and the delayed measured state corresponds to

$$\mathbf{z} = \begin{bmatrix} q \\ \theta \\ \omega_l \end{bmatrix}, \quad (\text{B.15})$$

whereas the state vector of the observer corresponds to (3.46). The error of the measured state  $e_{y_1} = \hat{y}_1 - y_1$  is

$$\dot{e}_{y_1} = \mathbf{a}_{21}^T \hat{\mathbf{e}}_z + a_{22} e_{y_1} - v - g_2 \xi(\theta). \quad (\text{B.16})$$

For sufficiently large  $M$  sliding mode exists and the equivalent control method yields

$$v_{\text{eq}} = \mathbf{a}_{21}^T \mathbf{e}_z - g_2 \xi(\theta). \quad (\text{B.17})$$

The observer error dynamics with respect to the non-measured states is

$$\begin{aligned} \dot{\mathbf{e}}_z &= (\mathbf{A}_{11} + \mathbf{l}_1 \mathbf{a}_{21}^T) \mathbf{e}_z + \mathbf{l}_2 e_{y_2}(t - \tau(t)) \\ &\quad - \mathbf{l}_1 g_2 \xi(\theta) - \mathbf{g}_1 \xi(\theta). \end{aligned} \quad (\text{B.18})$$

With (2.37) the error vector can be defined as

$$\mathbf{e} = \frac{1}{k_s} \begin{bmatrix} \hat{T}_l - T_l \\ \hat{T}_s - T_s \\ k_s(\hat{\omega}_l - \omega_l) \end{bmatrix} = \mathbf{e}_z + \mathbf{h}_2 \xi(\theta), \quad (\text{B.19})$$

where  $\mathbf{h}_2 = [0 \ 1 \ 0]^T$ . With the time-derivative of (B.19)

$$\dot{\mathbf{e}} = \dot{\mathbf{e}}_z + \mathbf{h}_2 \frac{d\xi}{d\theta} \dot{\theta} \quad (\text{B.20})$$

the error dynamics with respect to  $\mathbf{e}$  can be expressed, i.e.

$$\begin{aligned} \dot{\mathbf{e}} &= (\mathbf{A}_{11} + \mathbf{l}_1 \mathbf{a}_{21}^T)(\mathbf{e} - \mathbf{h}_2 \xi(\theta)) + \mathbf{l}_2 e_{y_2}(t - \tau(t)) \\ &\quad - \mathbf{l}_1 g_2 \xi(\theta) - \mathbf{g}_1 \xi(\theta) + \mathbf{h}_2 \frac{d\xi}{d\theta} \dot{\theta}. \end{aligned} \quad (\text{B.21})$$

Since  $\mathbf{A}_{11} \mathbf{h}_2 = -\mathbf{g}_1$ , and  $\mathbf{a}_{21}^T \mathbf{h}_2 = -g_2$  the terms corresponding to  $\xi(\theta)$  cancel out. In the contact phase  $d\xi/d\theta$  vanishes such that

$$\dot{\mathbf{e}} = \mathbf{A}_0 \mathbf{e} + \mathbf{A}_1 \mathbf{e}(t - \tau) \quad (\text{B.22})$$

is independently of the unknown backlash width. In the backlash phase  $d\xi/d\theta = 1$  such that

$$\dot{\mathbf{e}} = \mathbf{A}_0 \mathbf{e} + \mathbf{A}_1 \mathbf{e}(t - \tau(t)) + \mathbf{h}_2 \left( \frac{\omega_m}{k_g} - \omega_l \right). \quad (\text{B.23})$$

The matrix  $(\mathbf{A}_0 + \mathbf{A}_1)$  is invertible such that the steady-state error is

$$\mathbf{e}_\infty = -(\mathbf{A}_0 + \mathbf{A}_1)^{-1} \mathbf{h}_2 \left( \frac{\omega_m}{k_g} - \omega_l \right), \quad (\text{B.24})$$

where

$$(\mathbf{A}_0 + \mathbf{A}_1)^{-1} \mathbf{h}_2 = \begin{bmatrix} \frac{J_l l_{11} l_{23} + (J_m k_g - J_l l_{13}) l_{21} - d_l l_{11}}{k_s l_{11} l_{22} - k_s l_{12} l_{21} - k_s l_{11}} \\ \frac{J_m k_g l_{21}}{k_s l_{11} l_{22} - k_s l_{12} l_{21} - k_s l_{11}} \\ \frac{l_{11}}{l_{11} l_{22} - l_{12} l_{21} - l_{11}} \end{bmatrix},$$

and  $\mathbf{l}_1 = [l_{11} \ l_{12} \ l_{13}]^T$ ,  $\mathbf{l}_2 = [l_{21} \ l_{22} \ l_{23}]^T$ .

## B.2 Observer analysis with respect to a unknown load inertia

Basically, the model parameters are known from CAD modeling. The vehicle mass is considered in the load inertia  $J_l$  and therefore not exactly known. By the extension of the observer with the disturbance model the unknown load torque  $\hat{T}_l$  will be estimated. The parameter  $J_l$  appears only in the equation affected by the unknown input  $T_l$ . The analysis is performed for the backlash-free case. Assume that the estimated, constant load inertia corresponds to

$$\hat{J}_l = J_l + \delta J_l, \quad (\text{B.25})$$

where  $J_l$  correspond to the real load inertia. Then the inverse of (B.25) is

$$\frac{1}{\hat{J}_l} = \frac{1}{J_l} - \frac{\delta J_l}{J_l \hat{J}_l}. \quad (\text{B.26})$$

### B.2.1 Measurements without delay

With (B.26) the matrices  $\hat{\mathbf{A}}_{21}$  and  $\hat{\mathbf{A}}_{22}$  of observer of section 3.2.3 can be expressed as

$$\begin{aligned} \hat{\mathbf{A}}_{21} &= \mathbf{A}_{21} + \delta \mathbf{A}_{21} = \begin{bmatrix} -\frac{k_s}{J_l} & \frac{k_s}{J_l} \\ 0 & -\frac{k_s}{k_g J_m} \end{bmatrix} + \begin{bmatrix} \frac{k_s \delta J_l}{J_l \hat{J}_l} & -\frac{k_s \delta J_l}{J_l \hat{J}_l} \\ 0 & 0 \end{bmatrix}, \\ \hat{\mathbf{A}}_{22} &= \mathbf{A}_{22} + \delta \mathbf{A}_{22} = \begin{bmatrix} -\frac{d_l}{J_l} & 0 \\ 0 & -\frac{d_m}{J_m} \end{bmatrix} + \begin{bmatrix} \frac{d_l \delta J_l}{J_l \hat{J}_l} & 0 \\ 0 & 0 \end{bmatrix}. \end{aligned} \quad (\text{B.27})$$

Then the error dynamics resulting from the measurement vector is

$$\dot{\hat{\mathbf{e}}}_y = (\mathbf{A}_{21} + \delta \mathbf{A}_{21}) \hat{\mathbf{x}}_1 + (\mathbf{A}_{22} + \delta \mathbf{A}_{22}) \hat{\mathbf{y}} - \mathbf{v} - \mathbf{A}_{21} \mathbf{x}_1 - \mathbf{A}_{22} \mathbf{y}. \quad (\text{B.28})$$

Assuming that sliding mode exists the value for  $\mathbf{v}$  can be calculated with the help of the equivalent method, i.e.

$$\mathbf{v}_{\text{eq}} = \mathbf{A}_{21}\mathbf{e}_{\mathbf{x}_1} + \delta\mathbf{A}_{21}\hat{\mathbf{x}}_1 + \delta\mathbf{A}_{22}\hat{\mathbf{y}}. \quad (\text{B.29})$$

Substituting (B.29) into the error dynamics of  $\mathbf{e}_{\mathbf{x}_1} = \hat{\mathbf{x}}_1 - \mathbf{x}_1$  yields

$$\dot{\mathbf{e}}_{\mathbf{x}_1} = (\mathbf{L}\mathbf{A}_{21})\mathbf{e}_{\mathbf{x}_1} + \mathbf{L}(\delta\mathbf{A}_{21}\hat{\mathbf{x}}_1 + \delta\mathbf{A}_{22}\hat{\mathbf{y}}). \quad (\text{B.30})$$

The steady-state error is

$$\mathbf{e}_{\mathbf{x}_1,\infty} = -(\mathbf{L}\mathbf{A}_{21})^{-1}(\mathbf{L}\delta\mathbf{A}_{21}\hat{\mathbf{x}}_1 + \delta\mathbf{A}_{22}\hat{\mathbf{y}}). \quad (\text{B.31})$$

Assuming that  $\mathbf{L}$  is invertible (B.31) can be expressed as

$$\mathbf{e}_{\mathbf{x}_1,\infty} = -\mathbf{A}_{21}^{-1}(\delta\mathbf{A}_{21}\hat{\mathbf{x}}_1 + \delta\mathbf{A}_{22}\hat{\mathbf{y}}), \quad (\text{B.32})$$

where

$$-\mathbf{A}_{21}^{-1}\delta\mathbf{A}_{21} = \begin{bmatrix} \frac{\delta J_l}{\hat{J}_l} & -\frac{\delta J_l}{\hat{J}_l} \\ 0 & 0 \end{bmatrix}, \quad -\mathbf{A}_{21}^{-1}\delta\mathbf{A}_{22} = \begin{bmatrix} \frac{d_l\delta J_l}{k_s\hat{J}_l} & 0 \\ 0 & 0 \end{bmatrix}.$$

## B.2.2 Delayed and sampled measurements

With (B.26) the matrix  $\hat{\mathbf{A}}_{11}$  can be expressed as

$$\hat{\mathbf{A}}_{11} = \mathbf{A}_{11} + \delta\mathbf{A}_{11} = \begin{bmatrix} 0 & 0 & 0 \\ 0 & 0 & -1 \\ -\frac{k_s}{J_l} & \frac{k_s}{J_l} & -\frac{d_l}{J_l} \end{bmatrix} + \begin{bmatrix} 0 & 0 & 0 \\ 0 & 0 & 0 \\ \frac{k_s\delta J_l}{J_l\hat{J}_l} & -\frac{k_s\delta J_l}{J_l\hat{J}_l} & \frac{d_l\delta J_l}{J_l\hat{J}_l} \end{bmatrix}. \quad (\text{B.33})$$

Since the error differential equation with respect to the measured state  $\omega_m$  is independent of  $J_l$  and  $\hat{J}_l$  the equivalent method yields

$$\mathbf{v}_{\text{eq}} = \mathbf{a}_{21}^T \mathbf{e}_{\mathbf{x}_1}. \quad (\text{B.34})$$

The error dynamics of the non-measured states and the delayed measured state  $\mathbf{e}_z = \hat{\mathbf{z}} - \mathbf{z}$  is

$$\dot{\mathbf{e}}_z = \mathbf{A}_0\mathbf{e}_z + \mathbf{A}_1\mathbf{e}_{\mathbf{x}_1}(t_k) + \delta\mathbf{A}_{11}\hat{\mathbf{x}}_1. \quad (\text{B.35})$$

The steady-state error is

$$\mathbf{e}_{z,\infty} = -\mathbf{A}_0^{-1}\delta\mathbf{A}_{11} = -(\mathbf{A}_0 + \mathbf{A}_1)^{-1}\delta\mathbf{A}_{11} = \begin{bmatrix} \frac{\delta J_l}{J_l} & -\frac{\delta J_l}{J_l} & \frac{d_l\delta J_l}{k_s\hat{J}_l} \\ 0 & 0 & 0 \\ 0 & 0 & 0 \end{bmatrix}. \quad (\text{B.36})$$

## B.3 Observer analysis with known backlash width

In this section the backlash width, which corresponds to the angle of  $2\alpha$ , is assumed to be known exactly. The power-train model (2.40) corresponds to the synthesis model for the sliding mode observer design.

### B.3.1 Sliding mode observer for nonlinear systems

In [SHM86] a sliding mode observer for non-linear autonomous systems is presented. It is assumed that the system

$$\begin{aligned}\dot{\mathbf{x}} &= \mathbf{f}(\mathbf{x}, t), \\ \mathbf{y} &= \mathbf{C}\mathbf{x},\end{aligned}\tag{B.37}$$

with  $\mathbf{x} \in \mathbb{R}^n$ ,  $\mathbf{y} \in \mathbb{R}^r$  is locally observable. A non-linear system is locally observable if the rank of the non-linear observability matrix has full rank, see for example [Ada09]. The observer is

$$\begin{aligned}\dot{\hat{\mathbf{x}}} &= \hat{\mathbf{f}}(\hat{\mathbf{x}}, t) - \mathbf{K}\text{sgn}(\mathbf{s}), \\ \boldsymbol{\sigma} &= \hat{\mathbf{y}} - \mathbf{y},\end{aligned}\tag{B.38}$$

where  $\mathbf{K} \in \mathbb{R}^{n \times r}$ ,  $\text{sgn}(\cdot)$  denotes the vector-valued sign-function and  $\hat{\mathbf{f}}$  is the model of  $\mathbf{f}$ . Sliding mode occurs for

$$\dot{\sigma}_i \sigma_i < -\eta |\sigma_i|, \quad \eta > 0, \quad i = 1, \dots, r.\tag{B.39}$$

The observer gain matrix  $\mathbf{K}$  is designed in the same way as in the sliding mode observer design for LTI systems of section 3.2.1, i.e.

$$\mathbf{K} = \begin{bmatrix} \mathbf{L}\mathbf{M} \\ -\mathbf{M} \end{bmatrix}.\tag{B.40}$$

### B.3.2 Power-train observer design

The observer (B.38) is applied to the non-linear power-train model (2.39). For simplicity the unknown input is assumed to be zero. With the state transformation (3.19) the power-train model (2.39) corresponds to

$$\begin{bmatrix} \dot{\theta} \\ \dot{\mathbf{y}} \end{bmatrix} = \begin{bmatrix} a_{11} & \mathbf{a}_{12}^T \\ \mathbf{a}_{21} & \mathbf{A}_{22} \end{bmatrix} \begin{bmatrix} \theta \\ \mathbf{y} \end{bmatrix} + \begin{bmatrix} b_1 \\ \mathbf{b}_2 \end{bmatrix} u + \begin{bmatrix} g_1 \\ \mathbf{g}_2 \end{bmatrix} \xi(\theta),\tag{B.41}$$

where  $a_{11} = 0$ ,  $b_1 = 0$ ,  $g_1 = 0$  and

$$\begin{aligned}\mathbf{g}_2 &= \begin{bmatrix} -\frac{k_s}{J_l} \\ \frac{k_s}{k_g J_m} \end{bmatrix}, & \mathbf{a}_{12}^T &= \begin{bmatrix} -1 & \frac{1}{k_g} \end{bmatrix} \\ \mathbf{a}_{21} &= \begin{bmatrix} \frac{k_s}{J_l} \\ -\frac{k_s}{k_g J_m} \end{bmatrix}, & \mathbf{A}_{22} &= \begin{bmatrix} -\frac{d_l}{J_l} & 0 \\ 0 & -\frac{d_m}{J_m} \end{bmatrix}.\end{aligned}$$

The sliding mode observer incorporates the dead zone model of the backlash, i.e.

$$\begin{aligned}\dot{\hat{\theta}} &= \mathbf{a}_{12}^T \hat{\mathbf{y}} + \mathbf{l}^T \mathbf{v}, \\ \dot{\hat{\mathbf{y}}} &= \mathbf{a}_{21} \hat{\theta} + \mathbf{A}_{22} \hat{\mathbf{y}} + \mathbf{b}_2 u + \mathbf{g}_2 \xi(\hat{\theta}) - \mathbf{v}, \\ \mathbf{v} &= \mathbf{M} \operatorname{sgn}(\hat{\mathbf{y}} - \mathbf{y}).\end{aligned}\tag{B.42}$$

### B.3.3 Observer stability analysis

The observer error dynamics with respect to the measured states is

$$\dot{\mathbf{e}}_y = \mathbf{a}_{21} e_\theta + \mathbf{A}_{22} \mathbf{e}_y - \mathbf{v} + \mathbf{g}_2 \left( \xi(\hat{\theta}) - \xi(\theta) \right),\tag{B.43}$$

where  $\mathbf{e}_y = \hat{\mathbf{y}} - \mathbf{y}$  and  $e_\theta = \hat{\theta} - \theta$ . It is assumed that the diagonal elements of the matrix  $\mathbf{M}$  are sufficiently large such that a sliding mode is enforced in (B.43). In sliding mode  $\mathbf{e}_y = \mathbf{0}$ . With the equivalent control method  $\dot{\mathbf{e}}_y = \mathbf{0}$  such that

$$\mathbf{v}_{eq} = \mathbf{a}_{21} e_\theta + \mathbf{g}_2 \left( \xi(\hat{\theta}) - \xi(\theta) \right).\tag{B.44}$$

The term (B.44) is substituted into the observer error dynamics with respect to the non-measurable state  $\theta$ . This yields

$$\dot{e}_\theta = +\mathbf{l}^T \mathbf{a}_{21} e_\theta + \mathbf{l}^T \mathbf{g}_2 \left( \xi(\hat{\theta}) - \xi(\theta) \right).\tag{B.45}$$

The vector  $\mathbf{a}_{21} = -\mathbf{g}_2$ . The observer gain vector  $\mathbf{l}$  has to be designed such that  $\mathbf{l}^T \mathbf{a}_{21} = -\lambda$ ,  $\lambda > 0$ . Then the error dynamics corresponds to

$$\dot{e}_\theta = -\lambda e_\theta + \lambda \left( \xi(\hat{\theta}) - \xi(\theta) \right).\tag{B.46}$$

The stability of the observer error dynamics with respect to the non-measurable state  $\theta$  is shown with the help of a quadratic Lyapunov function, i.e.

$$V(e_\theta) = \frac{1}{2} \theta^2.\tag{B.47}$$

Its time-derivative corresponds to

$$\dot{V}(e_\theta) = -\lambda e_\theta^2 + \lambda e_\theta \left( \xi(\hat{\theta}) - \xi(\theta) \right).\tag{B.48}$$

Due to the shape of  $\xi(\theta)$ , see Fig. 2.9, the term

$$e_\theta \left( \xi(\hat{\theta}) - \xi(\theta) \right) \geq 0.\tag{B.49}$$

In the contact phase  $e_\theta^2 > e_\theta (\xi(\hat{\theta}) - \xi(\theta))$  such that (B.48) is negative definite. In the backlash phase

$$\left( \xi(\hat{\theta}) - \xi(\theta) \right) = e_\theta,\tag{B.50}$$

such that (B.48) is zero. The terms  $\mathbf{g}_2 e_\theta$  and  $\mathbf{a}_{21} e_\theta$  cancel out in (B.41) such that the observability is lost.

## B.4 Sliding surface with unknown load inertia

In this section the sliding surface (4.3) with not exactly known load inertia is derived. For the analysis the power-train is assumed to be in contact phase. It is further assumed that the damping coefficient  $d_s = 0$  for simplicity. The rolling resistance is assumed to be part of the load torque. According to (2.42) the synthesis model corresponds to

$$\begin{aligned}\dot{\varphi} &= \frac{\omega_m}{k_g} - \omega_l, \\ J_l \dot{\omega}_l &= k_s \varphi - d_l \omega_l - T_l, \\ J_m \dot{\omega}_m &= -\frac{k_s \varphi}{k_g} - d_m \omega_m + T_m.\end{aligned}\tag{B.51}$$

In this analysis the corresponding differential equations of (B.51) and the control law (4.7) with estimated load inertia  $\hat{J}_l$  and load torque  $\hat{T}_l$  are inserted into the time-derivative of the sliding surface (4.4) such that

$$\dot{\sigma} = \underbrace{\frac{k_s \hat{\varphi}}{\hat{J}_l} - \frac{k_s \varphi}{J_l}}_1 + \underbrace{\frac{T_l}{J_l} - \frac{\hat{T}_l}{\hat{J}_l}}_2 - \underbrace{\frac{d_l}{\hat{J}_l} \omega_l + \frac{d_l}{J_l} \omega_l}_3 - K \operatorname{sgn}(\sigma).\tag{B.52}$$

The estimated, constant load inertia corresponds to

$$\hat{J}_l = J_l + \delta J_l.\tag{B.53}$$

It is further assumed that the estimation error of the torsion angle is sufficiently small such that  $\hat{\varphi} = \varphi$ . With (B.53) the first part of (B.52) can be simplified such that

$$\frac{k_s \varphi}{\hat{J}_l} - \frac{k_s \varphi}{J_l} = -\frac{k_s \delta J_l}{J_l \hat{J}_l} \varphi.\tag{B.54}$$

For the simplification of the second part of (B.52) the second differential equation of (B.51) can be solved for  $T_l$ . Solving the load torque error  $e_{T_l} = \hat{T}_l - T_l$  for  $\hat{T}_l$  yields

$$\frac{T_l}{J_l} - \frac{\hat{T}_l}{\hat{J}_l} = -\frac{e_{T_l}}{\hat{J}_l} + \frac{\delta J_l}{J_l \hat{J}_l} (k_s \varphi - d_l \omega_l - J_l \dot{\omega}_l).\tag{B.55}$$

The third part of (B.52) corresponds to

$$\frac{d_l}{J_l} \omega_l - \frac{d_l}{\hat{J}_l} \omega_l = \frac{d_l \delta J_l}{J_l \hat{J}_l} \omega_l.\tag{B.56}$$

Substituting the right-hand sides of (B.54) to (B.56) into (B.52) yields

$$\dot{\sigma} = -\frac{e_{T_l}}{\hat{J}_l} - \frac{\delta J_l}{\hat{J}_l} \dot{\omega}_l - K \operatorname{sgn}(\sigma).\tag{B.57}$$

# Appendix C

## Parameters

### C.1 Test bench parameters

Table C.1: General test bench parameters.

Parameter	Value
Length	2000 mm
Width	780 mm
Height without screw feet	1200 mm
Dimension of outer hollow iron profiles	80×80×4 mm
Dimension of inner hollow iron profiles	80×80×3 mm
Weight	700 kg
Max. backlash width $2\alpha$	10°

Table C.2: Moments of inertia of test bench parts.

Part	Value
sensor	0.0003 kg m <sup>2</sup>
coupling	0.0154 kg m <sup>2</sup>
torsion bar	0.0006 kg m <sup>2</sup>
ball bearings at torsion bar	0.0003 kg m <sup>2</sup>
wheel bearing	0.0041 kg m <sup>2</sup>
tire	0.0506 kg m <sup>2</sup>
wheel rim	0.0437 kg m <sup>2</sup>
steel cylinder	1.38 kg m <sup>2</sup>
steel shaft	0.0052 kg m <sup>2</sup>
coupling at steel shaft with flange	0.0047 kg m <sup>2</sup>
ball bearing at steel shaft	0.0015 kg m <sup>2</sup>

Table C.3: Test-bench parameters of the linear synthesis model.

<b>Parameter</b>	<b>Value</b>
shaft stiffness $k_s$	1747.58 N m rad <sup>-1</sup>
shaft damping coefficient $d_s$	1 N m rad <sup>-1</sup> s <sup>-1</sup>
rotor inertia $J_m$	0.05 kg m <sup>2</sup>
load inertia $J_l$	1.4743 kg m <sup>2</sup>
viscous friction coefficient motor	0.005 N m s rad <sup>-1</sup>
viscous friction coefficient load	0.06 N m s rad <sup>-1</sup>
gear ratio $k_g$	1

Table C.4: Torsion bar.

<b>Parameter</b>	<b>Value</b>
steel type	Böhler VEW F550, spring steel, hardened and tempered.
steel material	50CrV4
length	30 cm
length with feather keys	50 cm
diameter	16.6 mm
torsion at 140 N m	4.59°
shear modulus	79.231 kN mm <sup>-2</sup>
load changes	2 000 000

Table C.5: Parameters of the steel cylinder.

<b>Parameter</b>	<b>Value</b>
Inertia	1.38 kg m <sup>2</sup>
radius $r_c$	0.2 m

Table C.6: Tire parameters.

<b>Parameter</b>	<b>Value</b>
Type	Michelin S83, 3-10
Width	3"
Diameter	10 mm
load speed index	42J, i.e. up to 150 kg at 100 km h <sup>-1</sup>
Weight	1.8 kg

Table C.7: Parameters of the Pacejka tire model.

Parameter	Value
peak value $D$	196 N
stiffness factor $B$	22
shape factor $C$	1.16
curvature factor $E$	-3.45

Table C.8: Identified tire parameters.

Parameter	Value
tire stiffness $k_t$	50 N/°
tire damping coefficient $d_t$	5 N m s rad <sup>-1</sup>
statical tire radius $r_{st}$	0.194 m

Table C.9: Parameters of the induction machine.

Parameter	Value
type	AEG AM 132M ZA
housing material	aluminium
weight	54 kg
rotor and motor shaft inertia	0.04 kg m <sup>2</sup>
overall motor efficiency	82.4 %
rated motor speed $n_n$	940 min <sup>-1</sup>
max. motor speed $n_{max}$	6000 min <sup>-1</sup>
pole pairs $p$	3
active power factor $\cos(\varphi)$	0.75
rated voltage $U_n$	400 V
rated current $I_n$	12.3 A
max. current $I_{max}$	44.7 A
rated torque $T_n$	55 N m
max. torque $T_{max}$	148 N m
stator leakage inductance $L_{s\sigma}$	8.2 mH
stator resistance $R_s$	879.9 mΩ
rotor leakage inductance $L_{r\sigma}$	8.2 mH
rotor resistance $R_r$	879.9 mΩ
mutual inductance $L_h$	110 mH
magnetizing current $I_\mu$	7.5 A

Table C.10: Rotary encoder parameters.

Parameter	Value
type	ECN/ERN 100 single turn, absolute angle
interface type	EnDat 2.2/01
outer diameter	87 mm
shaft diameter	38 mm
resolution	25 bits
line counts	2048
system accuracy	$\pm 0.0056^\circ$
supply voltage	5 V
calculation time	$\leq 25 \mu\text{s}$

Table C.11: Servo Drive.

Parameter	Value
type	ACOPOS 1180.00-2 with line filter braking resistor and DC bus power supply
voltage	three phase 400 V <sub>eff</sub>
intermediate DC voltage	400 V
continuous rated current	19 A <sub>eff</sub>
rated power	9 kW
switching frequency	5, 10 (nominal) and 20 kHz
DC bus power supply	24 V
Plug-in module slots	4
Used Plug-in modules	EnDat encoder interfaces Ethernet Powerlink interface
weight	10.1 kg

Table C.12: Identified parameters for motor torque calculation

Parameter	Value
torque constant $k_T$	3.33 N m A <sup>-1</sup>
constant $k_M$ w.r.t. magnetization losses	0.9 N m
saturation angular velocity $\omega_{m,0}$	0.5 rad s <sup>-1</sup>

Table C.13: Parameters of the second-order model of the induction machine

Parameter	Value
undamped frequency $\omega_n$	1753.85 (rad s <sup>-1</sup> )
damping ratio $d_n$	0.7

## C.2 Parameters of the MBS simulation model

Table C.14: Parameters of the MBS power-train model.

Parameter	Value
stiffness left shaft	80 Nm/°
stiffness right shaft	80 Nm/°
vehicle mass	860 kg
transmission ratio	11.94
backlash width motor	10°
backlash width tripod joint	1°
torsional tire stiffness	330 Nm/°
stiffness of mountings	200 N m mm <sup>-1</sup>

Table C.15: Inertia of the MBS power-train parts.

Parameter	Value
inertia of rotor	0.047 kg m <sup>2</sup>
inertia of roll	33.3 kg m <sup>2</sup>
inertia of wheel	0.86 kg m <sup>2</sup>
inertia of hub and rim	0.26 kg m <sup>2</sup>
inertia of tire	0.59 kg m <sup>2</sup>
inertia of left shaft	1967 kg mm <sup>2</sup>
inertia of right shaft	1991 kg mm <sup>2</sup>
inertia of differential gear	0.012 kg m <sup>2</sup>
inertia of input shaft (diff)	90 kg mm <sup>2</sup>
inertia of shaft between motor and diff	940 kg mm <sup>2</sup>
inertia of right output shaft (diff)	610 kg mm <sup>2</sup>
inertia of left output shaft (diff)	507 kg mm <sup>2</sup>

# Nomenclature

## Symbols

Symbol	Unit	Description
$\mathbf{A}$		system matrix
$\mathbf{A}_{ij}, \mathbf{a}_{ij}$		sub-matrix of system matrix
$\tilde{\mathbf{A}}_i$		sub-matrix (block observable form)
$B$		stiffness factor, Pacejka tire model
$\mathbf{b}$		input vector
$\tilde{\mathbf{b}}$		input vector (block observable form)
$C$		shape factor, Pacejka tire model
$\mathbf{C}$		output matrix
$D$		peak factor, Pacejka tire model
$\tilde{\mathbf{d}}$		unknown input vector (block observable form)
$d$		conditional usage delayed corr. term
$d_c$	$\text{N m s rad}^{-1}$	viscous friction coefficient cylinder
$d_m$	$\text{N m s rad}^{-1}$	viscous friction coefficient motor
$d_l$	$\text{N m s rad}^{-1}$	viscous friction coefficient load
$d_s$	$\text{N m s rad}^{-1}$	viscous damping coefficient shaft
$d_t$	$\text{N m s rad}^{-1}$	viscous damping coefficient tire
$E$		curvature factor, Pacejka tire model
$\mathbf{e}$		error vector
$e_{\text{rel}}$		relative quantization error (sensor)
$e_i$		error variable (block observable form)
$e_w$	m	distance of wheel center to pressure maximum of tire
$f_0$	$\text{s}^{-1}$	reference frequency (sensor)
$F_r, F_r(\omega_t)$	N	rolling resistance
$f_r$		rolling resistance coefficient
$F_a$	N	longitudinal axle force
$F_{\text{acc}}$	N	acceleration resistance
$F_{\text{ad}}$	N	air drag resistance

Symbol	Unit	Description
$F_x$	N	longitudinal tire force
$F_z$	N	vertical tire force
$g$	$\text{m s}^{-2}$	gravitational acceleration
$G$	$\text{N m}^{-2}$	shear modulus
$G_a(s)$		transfer function of actuator dynamics
$G_{\text{sm}}$		transfer function motor to shaft torque
$G_{\text{sm},0}$		transfer function motor to shaft torque (undamped)
$G_{\text{sm},a}(s)$		transfer function motor to shaft torque (approx.)
$\mathbf{h}_i$		i-th unit vector
$\tilde{\mathbf{H}}_i$		sub-matrix (block observable form)
$i_{sq}$	A	motor current q-axis
$J_c$	$\text{kg m}^2$	steel cylinder inertia
$J_l$	$\text{kg m}^2$	inertia load
$J_m$	$\text{kg m}^2$	inertia motor
$J_r$	$\text{kg m}^2$	inertia of wheel rim
$J_{\text{roll}}$	$\text{kg m}^2$	MBS roll inertia
$J_s$	$\text{kg m}^2$	shaft inertia
$J_t$	$\text{kg m}^2$	tire inertia
$K$		SMC gain value
$k_1, k_2$		gain GSOA
$k_g$		gear ratio
$k_M$	N m	constant w.r.t. magnetization losses
$k_s$	$\text{N m rad}^{-1}$	shaft stiffness
$k_{s,1}, k_{s,2}$	$\text{N m rad}^{-1}$	stiffness of left and right half shaft
$k_t$	$\text{N m rad}^{-1}$	torsional tire stiffness
$k_T$	$\text{N m A}^{-1}$	motor torque constant
$l$	m	length
$\mathbf{L}$		observer gain matrix
$\mathbf{L}_1, \mathbf{l}_1$		observer gain w.r.t. output without delay
$\mathbf{L}_2, \mathbf{l}_2$		observer gain w.r.t. output with delay
$L_h$	H	mutual inductivity
$L_i$		Lipschitz constant (block observable form)
$L_r$	H	rotor inductivity
$\mathbf{M}$		observer gain matrix w.r.t. discontinuous part
$\mathbf{m}$		input vector of unknown input
$m_v$	kg	vehicle mass
$m_w$	kg	wheel mass
$n$		system order
$n_0(s)$		denominator polynomial
$N$		number of sensor increments for measurement
$N_0$		total number of magnetic sensor units

Symbol	Unit	Description
$\mathbf{p}$		eigen-vector
$p$		exponent GSOA, pole pairs
$\mathbf{P}$		solution of Lyapunov equation
$r_c$	m	steel cylinder radius
$r_{st}$	m	static tire radius
$r_{dyn}$	m	dynamical tire radius
$s$	$s^{-1}$	Laplace variable
$s_x$		longitudinal tire slip
$s_{x,c}$		critical tire slip at maximum adhesion
$\mathbf{T}$		regular state transformation matrix
$\mathbf{t}^t$		row vector of state transformation matrix
$t_k, t_{k+1}$	s	sampled time instants
$T_l$	N m	load torque
$T_m$	N m	motor torque
$T_{m,ref}$	N m	reference motor torque
$T_{ref}$	N m	reference shaft torque
$T_s$	N m	shaft torque
$T_t$	N m	tire torque
$T_{th}$	N m	threshold torque
$T(s)$		command step response
$t_{gr}$	s	group delay
$u$		actuating signal, system input
$V$		Lyapunov function, Lyapunov-Krasovskii functional
$V_0$		transfer function gain
$\mathbf{V}$		matrix of eigen-vectors
$v_x$	$m s^{-1}$	longitudinal vehicle velocity
$w$		unknown input
$\mathbf{W}_o$		observability Gramian
$\mathbf{x}$		state vector
$\hat{\mathbf{x}}$		state vector estimate
$\mathbf{x}_1$		sub-vector of state vector
$\mathbf{y}$		output vector
$\mathbf{y}_1$		sub-vector of output vector
$\mathbf{z}$		sub-vector of state vector
$\mathbf{z}, \mathbf{z}_i$		transformed state (sub-)vector (block observable form)
$z_0(s)$		numerator polynomial

Symbol	Unit	Description
$\alpha$	rad	half backlash width
$\beta$	rad	backlash angle
$\gamma$		decay rate
$\Delta\phi$	rad	angle of N sensor units
$\Delta t$	s	time interval (wheel speed sensor)
$\delta_{i,w}$		relative degree of output $i$ w.r.t unknown input $w$
$\delta_1, \delta_2$		bounds on disturbance GSOA
$\theta$	rad	total angle of deflection at shaft including backlash
$\lambda$		parameter of sliding surface
$\lambda_0, \tilde{\lambda}_0$		real part of eigenvalues
$\kappa_{1,i,j}, \kappa_{2,i,j}$		gains of super-twisting algorithm
$\mu$		adhesion
$\mu_h$		maximum adhesion
$\mu_g$		adhesion at pure slip
$\nu(\cdot)$		abbreviation for super-twisting algorithm
$\varepsilon_c$		boundary layer width controller
$\varepsilon_o$		boundary layer width observer
$\varphi$	rad	shaft torsion angle
$\varphi_t$	rad	tire torsion angle
$\varphi_{\text{ref}}$	rad	reference torsion angle
$\rho_i$		dimension of sub-block $i$ (block observable form)
$\rho_1, \rho_2$		disturbances GSOA
$\sigma$		sliding surface
$\sigma(\cdot)$		spectrum of a matrix
$\tau_f$	s	filter time constant
$\tau_b$	s	delay due to bus transmission
$\tau_0$	s	minimum delay
$\tau_m$	s	maximum delay
$\tau_s$	s	maximum delay due to sampling
$\xi(\theta)$		correction due to backlash
$\chi$	rad	road gradient angle
$\bar{\omega}$	rad s <sup>-1</sup>	difference angular frequency
$\omega_0$	rad s <sup>-1</sup>	undamped natural frequency
$\omega_m$	rad s <sup>-1</sup>	motor angular frequency
$\omega_{m,0}$	rad s <sup>-1</sup>	sat. angular frequency
$\omega_l$	rad s <sup>-1</sup>	load angular frequency
$\omega_{\text{res}}$	rad s <sup>-1</sup>	resonance frequency
$\omega_r$	rad s <sup>-1</sup>	angular frequency of wheel rim
$\omega_s$	rad s <sup>-1</sup>	sensor angular speed

Symbol	Unit	Description
$\omega_{s,m}$	$\text{rad s}^{-1}$	measured sensor angular speed
$\omega_{s,m,f}$	$\text{rad s}^{-1}$	measured and filtered sensor angular speed
$\omega_t$	$\text{rad s}^{-1}$	tire angular frequency
$\omega_{th}$	$\text{rad s}^{-1}$	threshold tire angular frequency
$\psi$	s	delay time
$\Psi_{rd}$	Wb	rotor flux, d-axis
$\zeta$		damping ratio

## Acronyms

Acronym	Name
ABS	Anti-lock Braking System
CAN	Controller Area Network
COG	Center of Gravity
ECU	Electronic Control Unit
EM	Electric Machine
ESC	Electronic Stability Control
EV	Electric Vehicle
FOC	Field-Oriented Control
GSOA	Generic Second Order Algorithm
HEV	Hybrid Electric Vehicle
HV	High-Voltage
IC	Integrated Circuit
IM	Induction Machine
LMI	Linear Matrix Inequality
LQR	Linear Quadratic Regulator
LTI	Linear Time-Invariant
MBS	Multi-Body System
PI	Proportional Integral
SMC	Sliding Mode Control
SMO	Sliding Mode Observer
TDMA	Time Division Multiple Access

# List of Figures

2.1	Two-mass system with additional viscous friction at the motor and the load. . . . .	7
2.2	Roots of the normed second order polynomial. . . . .	9
2.3	Bode diagrams of the transfer function (2.8) of a two-mass system and its approximation (2.16). . . . .	10
2.4	Forces acting on the wheel and vehicle according to [MW04]. . . .	11
2.5	Friction coefficient $\mu$ versus tire slip. . . . .	12
2.6	Dead zone model for the shaft torque $T_s(\theta)$ in the presence of backlash of width $2\alpha$ . . . . .	14
2.7	Phase plane plots of backlash models. Within the open set of the shaded area there is no contact of the gear teeth. . . . .	14
2.8	Power train of an electrically driven vehicle. . . . .	15
2.9	Nonlinear function $\xi(\theta)$ for correcting a linear function in $\theta$ in order to model the effect of backlash. . . . .	18
2.10	Automotive wheel speed sensor with magnetic multi pole ring. . .	20
2.11	Real wheel angular velocity, output of the sensor model and subsequently filtered signal. . . . .	20
2.12	Test bench for investigating power train control concepts. . . . .	22
2.13	Tire modeled as an elastic element with stiffness and damping coefficient $k_t$ and $d_t$ . . . . .	23
3.1	Representation of a boundary layer with a saturation function for chattering reduction. . . . .	32
3.2	Delayed and sampled signal due to network or bus transmission. . .	33
3.3	Variable time delay $\tau(t)$ due to sampling. Additional constant delay $\tau_0$ due to measurement processing and bus transmission. The overall delay is assumed to be bounded by $\tau_m$ . . . . .	33
3.4	Exponential decay rate $\gamma$ of the observer error dynamics in dependence of the real part $-\tilde{\lambda}_0$ of the eigenvalues of $\mathbf{A}_0 + \mathbf{A}_1$ . . . . .	38
3.5	Value $\iota$ which is a measure for the estimation error of the load angular velocity signal in the backlash phase in dependence of the real part $-\tilde{\lambda}_0$ of the eigenvalues of $\mathbf{A}_0 + \mathbf{A}_1$ . . . . .	38
3.6	Step-by-step sliding mode observer for the power-train. . . . .	45
4.1	Boundary layer solution for chattering reduction. . . . .	50

4.2	Closed loop transfer function for stability analysis of the control law within the boundary layer. . . . .	51
4.3	Overview of the controller software. . . . .	54
4.4	Limitation of the reference torque and its gradient within the backlash phase for the case that no load angular signal is available. . .	55
4.5	Multi Body System model of an electrically driven rear axle of a hybrid prototype vehicle. . . . .	56
4.6	Longitudinal tire force $F_x$ versus tire slip $s_x$ . . . . .	57
4.7	Observer-based Sliding Mode Control evaluated with a MBS model of an electrically driven rear axle power-train. . . . .	58
4.8	Multi Body System simulation of the control concept at an acceleration maneuver. . . . .	59
4.9	Multi Body System simulation of the control concept at a deceleration maneuver. . . . .	60
4.10	Comparing the control concept with the uncontrolled simulation. . .	61
5.1	Test bench for investigating the power-train control concepts. . . .	65
5.2	Test bench without metal frame. . . . .	66
5.3	Testbench configuration. . . . .	68
5.4	Step responses of the scaled motor current $i_{sq}$ and the linear second order actuator model. . . . .	69
5.5	Speed dependent friction at steady state angular velocities and linear friction torque. . . . .	70
5.6	Longitudinal tire force versus wheel slip. . . . .	71
5.7	Evaluation of the test bench simulation model at an acceleration maneuver. . . . .	72
5.8	Evaluation of the test bench simulation model at a deceleration maneuver. . . . .	73
5.9	Observer of section 3.2.3 using non-delayed measurement signals at a torque step and subsequent step to zero. . . . .	75
5.10	Observer of section 3.2.3 at a positive and negative torque step maneuver. . . . .	76
5.11	Reference and controlled shaft torque based on the observer of section 3.2.1 using non-delayed measurement signals. . . . .	79
5.12	Comparison of the high-resolution, the measured and the estimated load angular velocity signal in the contact phase. . . . .	80
5.13	Reference and controlled shaft torque based on the observer using the delayed and sampled load angular velocity measurement. . . .	82
5.14	Controlled shaft torque using only the motor angular velocity signal as measurement. . . . .	83
5.15	Reference and controlled shaft torque based on the second-order step-by-step observer. . . . .	84
5.16	Reference and controlled shaft torque based on the observer of Section 3.3. . . . .	86

# List of Tables

3.1	Observability measure according to Litz. . . . .	28
3.2	Observability measure according to Benninger and Rivoir with damp- ing coefficient $d_s = 1$ . . . . .	29
3.3	Observability measure according to Benninger and Rivoir with damp- ing coefficient $d_s = 0$ . . . . .	29
4.1	Controller and observer parameters of the control concept for the MBS simulation. . . . .	58
5.1	Observer Parameters for load angular velocity without delay. . . .	78
5.2	Controller parameters for load angular velocity without delay. . .	78
5.3	Parameters for the observer using the delayed and sampled load angular velocity measurement. . . . .	81
5.4	Controller parameters based on the observer using the delayed and sampled load angular velocity measurement. . . . .	81
5.5	Observer gains of the second-order step-by-step observer. . . . .	85
5.6	Controller parameters of the GSOA. . . . .	85
C.1	General test bench parameters. . . . .	99
C.2	Moments of inertia of test bench parts. . . . .	99
C.3	Test-bench parameters of the linear synthesis model. . . . .	100
C.4	Torsion bar. . . . .	100
C.5	Parameters of the steel cylinder. . . . .	100
C.6	Tire parameters. . . . .	100
C.7	Parameters of the Pacejka tire model. . . . .	101
C.8	Identified tire parameters. . . . .	101
C.9	Parameters of the induction machine. . . . .	101
C.10	Rotary encoder parameters. . . . .	102
C.11	Servo Drive. . . . .	102
C.12	Identified parameters for motor torque calculation . . . . .	102
C.13	Parameters of the second-order model of the induction machine .	102
C.14	Parameters of the MBS power-train model. . . . .	103
C.15	Inertia of the MBS power-train parts. . . . .	103

# Bibliography

- [ABP04] N. Amann, J. Böcker, and F. Prenner. Active damping of drive train oscillations for an electrically driven vehicle. *Mechatronics, IEEE/ASME Transactions on*, 9(4):697–700, Dec. 2004.
- [Ada09] Jürgen Adamy. *Nichtlineare Regelungen*. Springer Berlin Heidelberg 2009, 2009.
- [AH10] Ulrich Angeringer and Martin Horn. Damping of driveline oscillations in hybrid and electric vehicles. In *10th International Symposium on Advanced Vehicle Control, AVEC'10*, Loughborough, United Kingdom, Aug. 2010.
- [AH11] Ulrich Angeringer and Martin Horn. Sliding mode drive line control for an electrically driven vehicle. In *Control Applications (CCA), 2011 IEEE International Conference on*, pages 521–526, Sept. 2011.
- [ARH12] Ulrich Angeringer, Markus Reichhartinger, and Martin Horn. Drive line control for electrically driven vehicles using generalized second order sliding modes. In *2012 IFAC Workshop on Engine and Powertrain Control, Simulation and Modeling (ECOSM12)*, pages 79–84, IFP Energies nouvelles, Rueil-Malmaison, France, 2012.
- [BR86] N. F. Benninger and J. Rivoir. Ein neues konsistentes maß zur beurteilung der steuerbarkeit in linearen, zeitinvarianten systemen. a new consistent controllability measure for linear timeinvariant systems. *at - Automatisierungstechnik*, 34(12):473–479, 1986.
- [BS88] S.R. Beale and B. Shafai. Robust control system design with proportional integral observer. In *Decision and Control, 1988., Proceedings of the 27th IEEE Conference on*, pages 554 –557 vol.1, dec 1988.
- [CSV<sup>+</sup>06] A. Chamroo, A. Seuret, C. Vasseur, J. P Richard, and H.P. Wang. Observing and controlling plants using their delayed and sampled outputs. In *Computational Engineering in Systems Applications, IMACS Multiconference on*, volume 1, pages 851–857, 2006.
- [ES98] Christopher Edwards and Sarah K. Spurgeon. *Sliding Mode Control: Theory and Applications*. Taylor & Francis, 1998.

- [FB06] Thierry Floquet and Jean-Pierre Barbot. A canonical form for the design of unknown input sliding mode observers. In Christopher Edwards, Enric Fossas Colet, and Leonid Fridman, editors, *Advances in Variable Structure and Sliding Mode Control*, volume 334 of *Lecture Notes in Control and Information Science*, pages 271–292. Springer Berlin Heidelberg, 2006.
- [FLD06a] L. Fridman, A. Levant, and J. Davila. High-order sliding-mode observation and identification for linear systems with unknown inputs. In *Decision and Control, 2006 45th IEEE Conference on*, pages 5567–5572, dec. 2006.
- [FLD06b] L. Fridman, A. Levant, and J. Davila. High-order sliding-mode observer for linear systems with unknown inputs. In *Variable Structure Systems, 2006. VSS'06. International Workshop on*, pages 202–207, june 2006.
- [Föl08] Otto Föllinger. *Regelungstechnik: Einführung in die Methoden und ihre Anwendung*. Hüthig Verlag Heidelberg, 10. auflage edition, 2008.
- [FPL12] Uwe Kiencke Fernando Puente León. *Messtechnik. Systemtheorie für Ingenieure und Informatiker*. Springer-Verlag Berlin Heidelberg, ninth edition, 2012.
- [Fri14] E. Fridman. *Introduction to Time-Delay Systems: Analysis and Control*. Systems & Control: Foundations & Applications. Birkhäuser, Springer, 2014.
- [GK13] Gunther Götting and Markus Kretschmer. Development and series application of a vehicle drivetrain observer used in hybrid and electric vehicles. In *Electric Vehicle Symposium and Exhibition (EVS27), 2013 World*, pages 1–9, Nov 2013.
- [GKC03] Keqin Gu, Vladimir L. Kharitonov, and Jie Chen. *Stability of Time-delay Systems*. Birkhäuser Boston, 2003.
- [Hau83] M.L.J. Hautus. Strong detectability and observers. *Linear Algebra and its Applications*, 50:353 – 368, 1983.
- [HD04] Martin Horn and Nicolaos Dourdoumas. *Regelungstechnik*. Pearson Studium, 2004.
- [HK07] Markus S. Haschka and Volker Krebs. Beobachtung der verdrillung in einem kfz-antriebsstrang mit lose (observing the torque of a powertrain with backlash). *at - Automatisierungstechnik*, 55(3):127–135, March 2007.
- [Kha02] H. K. Khalil. *Nonlinear systems*. Pearson Education. Prentice Hall, third edition, 2002.

- [KN05] U. Kiencke and L. Nielsen. *Automotive Control Systems*. Springer Verlag, second edition, 2005.
- [Kre93] Erwin Kreyszig. *Advanced Engineering Mathematics*. John Wiley & Sons, 1993.
- [LE07] A. Lagerberg and B. Egardt. Backlash estimation with application to automotive powertrains. *Control Systems Technology, IEEE Transactions on*, 15(3):483–493, may. 2007.
- [Lev93] Arie Levant. Sliding order and sliding accuracy in sliding mode control. *International Journal of Control*, 58(6):1247–1263, 1993.
- [Lev98] Arie Levant. Robust exact differentiation via sliding mode technique. *Automatica*, 34(3):379–384, 1998.
- [LF12] Kun Liu and Emilia Fridman. Wirtinger’s inequality and lyapunov-based sampled-data stabilization. *Automatica*, 48(1):102 – 108, 2012.
- [Lun13] Jan Lunze. *Regelungstechnik 2*. Number Band 2 in Springer-Lehrbuch. Springer Verlag, 7 edition, 2013.
- [MDCF06] R. Merzouki, J.A. Davila, J.C. Cadiou, and L. Fridman. Backlash phenomenon observation and identification. In *American Control Conference, 2006*, June 2006.
- [Men01] Marcus Menne. *Drehschwingungen im Antriebsstrang von Elektrostraßenfahrzeugen - Analyse und aktive Dämpfung*. Aachener Beiträge des ISEA, Band 24. Wissenschaftsverlag Mainz, 2001.
- [Mor11] Jaime Moreno. Lyapunov approach for analysis and design of second order sliding mode algorithms. In Leonid Fridman, Jaime Moreno, and Rafael Iriarte, editors, *Sliding Modes after the First Decade of the 21st Century*, volume 412 of *Lecture Notes in Control and Information Sciences*, pages 113–149. Springer Berlin / Heidelberg, 2011.
- [Mos11] Sonja Moschik. *Steuerbarkeitsmaße für lineare zeitinvariante Systeme*. PhD thesis, Graz University of Technology, 2011.
- [MW04] Manfred Mitschke and Henning Wallentowitz. *Dynamik der Kraftfahrzeuge*. VDI-Buch. Springer Berlin Heidelberg, 4. auflage edition, 2004.
- [NG02] Mattias Nordin and Per-Olof Gutman. Controlling mechanical systems with backlash – a survey. *Automatica*, 38(10):1633–1649, 2002.
- [NGG97] Mattias Nordin, Johann Galic’, and Per-Olof Gutman. New models for backlash and gear play. *International Journal of Adaptive Control and Signal Processing*, 11(1):49–63, 1997.

- [Pac02] Hans B. Pacejka. *Tyre and Vehicle Dynamics*. Automotive engineering. Butterworth-Heinemann, Oxford, 2002.
- [PB02] Wilfrid Perruquetti and Jean Pierre Barbot, editors. *Sliding Mode Control in Engineering*. Marcel Dekker Inc., 2002.
- [QD99] Nguyen Phung Quang and Jörg-Andreas Dittrich. *Praxis der feldorientierten Drehstromantriebsregelungen*. Expert-Verlag, zweite edition, 1999.
- [Rei12a] Konrad Reif. *Automobilelektronik. Eine Einführung für Ingenieure*. STUDIUM, ATZ/MTZ-Fachbuch. Vieweg + Teubner Verlag, Springer Fachmedien Wiesbaden, Springer Fachmedien Wiesbaden GmbH, fourth edition, 2012.
- [Rei12b] Konrad Reif, editor. *Sensoren im Kraftfahrzeug*. Bosch Fachinformation Automobil. Vieweg + Teubner Verlag, Springer Fachmedien Wiesbaden, second edition, 2012.
- [Sch09] Dierk Schröder. *Elektrische Antriebe - Regelung von Antriebssystemen*. Springer Berlin Heidelberg, 3 edition, 2009.
- [SEFL13] Y. Shtessel, C. Edwards, L. Fridman, and A. Levant. *Sliding Mode Control and Observation*. Control Engineering. Birkhäuser, 2013.
- [SHM86] J.-J. E. Slotine, J. K. Hedrick, and E. A. Misawa. Nonlinear state estimation using sliding observers. volume 25, pages 332–339, dec. 1986.
- [SL91] Jean-Jacques E. Slotine and Weiping Li. *Applied Nonlinear Control*. Prentice Hall, Englewood Cliffs, New Jersey, 1991.
- [Spu08] Sarah K. Spurgeon. Sliding mode observers: a survey. *International Journal of Systems Science*, 39(8):751–764, 2008.
- [SSK10] Rainer Schruth, Germano Sandoni, and Wolfgang Kriegler. Challenges of an electronically distributed all wheel drive on basis of a “retrofit” full hybrid 4wd solution. In *The 25th World Battery, Hybrid and Fuel Cell Electric Vehicle Symposium & Exhibition*, Shenzhen, China, Nov. 2010.
- [TE09] P. Templin and B. Egardt. An LQR torque compensator for driveline oscillation damping. In *Control Applications, (CCA) Intelligent Control, (ISIC), 2009 IEEE*, pages 352–356, jul. 2009.
- [UGS09] V. Utkin, J. Guldner, and Jingxin Shi. *Sliding Mode Control in Electromechanical Systems*. CRC Press, second edition, 2009.

- [Utk92] Vadim I. Utkin. *Sliding Modes in Control and Optimization*. Springer Berlin, Heidelberg, 1992.
- [Web08] Lena Webersinke. *Adaptive Antriebsstrangregelung für die Optimierung des Fahrverhaltens von Nutzfahrzeugen*. PhD thesis, Universitätsverlag Karlsruhe, Karlsruhe, 2008.
- [XHH<sup>+</sup>11] Lu Xiaohui, Chen Hong, Zhang Huayu, Wang Ping, and Gao Bingzhao. Design of model predictive controller for anti-jerk during tip-in/out process of vehicles. In *Control Conference (CCC), 2011 30th Chinese*, pages 3395–3400, july 2011.
- [ZDG96] Kemin Zhou, John C. Doyle, and Keith Glover. *Robust and Optimal Control*. Prentice-Hall, Upper Saddle River, NJ, USA, 1996.